

Development and Validation of Multibody Road Vehicle Simulation Models for Handling Studies

Pontus Fyhr, Kristoffer Lundahl

March 18, 2009

Master's Thesis in Mechanical Engineering
Supervisor at Division of Mechanics at the Department of Mechanical
Engineering at Lund University: Per Lidström
Examiner: Solveig Melin

LUND UNIVERSITY
DEPARTMENT OF MECHANICAL ENGINEERING
SE 223 00 LUND
SWEDEN

Abstract

Vehicle models are often bound by non-disclosure agreements with manufacturers. This thesis presents a vehicle model based on vehicle data gathered for the National Advanced Driving Simulator in Ohio and therefore it is not bound by such limitations and can be used in future research projects.

The development and validation of the vehicle model requires understanding of the subsystems studied, component based modelling is therefore used in order to evaluate and validate each subsystem individually.

The nonlinear behaviour of vehicle subsystems determines vehicle behaviour at limit handling manoeuvres, physical suspension and steering models are used in order to accurately capture geometric nonlinearities. A lumped hub compliance model including normal load compliance is developed and included in the suspension model.

Validation of the entire vehicle is performed in quasi-static tests as well as driving experiments.

Discussion focus is placed on the lumped hub compliance modelling. A differential compliance formulation is presented in order to circumvent the use of a non-invertible stiffness matrix. Investigations of the effects of lumping elasticities in the wheel hub are performed, as this method is not without its limitations. The lumped elasticity component sees different loads depending on the degree of anti-roll bar engagement, this causes problems with parametrisation of the lumped elasticity as the force-deflection relation differs between bump and roll motions as spring and anti-roll bar loads are not applied at the same location and direction on the suspension. Elastic hub effects on roll centres and jacking forces are also investigated and discussed.

Further studies following this work are suggested regarding compliance modelling. The utility of this unrestricted model may be for studies of handling effects on controlled brake or drive systems.

Contents

1	Introduction	1
1.1	Content	2
2	Problem Statement	5
2.1	Goal	5
2.2	Purposes	5
2.3	Validation Methodology	6
2.4	Related Work	6
3	Simulation Environment	7
3.1	Modelica	8
3.2	Dymola	8
3.2.1	Acausal and Causal Models	8
3.3	Dymola	9
3.4	Vehicle Dynamics Library	9
4	Tyres	11
4.1	Tyre Models	11
4.2	The STI Tyre Model	12
4.2.1	Model Implementation	13
4.3	Tyre Model Results	15
4.4	Tyre Model Validation	17
5	Chassis	19
5.1	Vehicle Topology	19
5.2	Multibody modelling	19
5.2.1	Kinematics	22
5.2.2	Springs and Dampers	22
5.2.3	Modelling the Vehicle	23
5.3	Chassis Model Validation	25
5.3.1	Chassis Analysis	26
5.3.2	Roll Centre	26

5.4	Kinematics Validation	27
6	Compliances	29
6.1	Compliance Modeling	29
6.1.1	Modelling the Hub Elasticity	31
6.1.2	Hub Elasticity Parameter Determination	35
6.1.3	Steering Compliance Modelling	37
6.2	Compliance Validation	37
7	Accomplishment	39
7.1	Preliminaries	39
7.2	Model Development Chronology	39
7.2.1	Vehicle Parameter Identification and Modelling Sequence	40
7.2.2	Iterative Approach	40
8	Results	43
8.1	Vehicle Simulation	43
8.1.1	Frame Resolves	43
8.1.2	Increasing Steer	44
8.1.3	Step Steer	46
8.1.4	Yaw	47
8.1.5	Pitch and Jacking	48
8.1.6	Roll	50
9	Conclusions	55
9.1	Restrictions and Limitations	55
9.2	Final Discussion	56
9.2.1	Elasticity Modelling	56
9.2.2	Kinematics	56
9.2.3	Final Conclusion	57
9.3	Future Work	57
10	Acknowledgements	59
	References	61
A	Basic Vehicle Dynamics Terminology	63
A.1	Coordinate Systems	63
A.2	Motions and Angles	63
A.2.1	Body	64
A.2.2	Wheel	65
A.3	Springs and Dampers	67
A.4	Instant Centre	67

A.5	Roll Centre	68
A.6	Jacking	68
A.7	Anti Geometries	68
A.8	Understeer - Neutral Steer - Oversteer	69
A.9	Aerodynamic Effects	69
A.10	Tyres	70
A.10.1	Slip	70
B	Vehicle Measurements	73
B.1	Vehicle Inertia Measurement	73
B.2	Kinematics and Compliance	73
B.3	Driving Manoeuvres	73
B.3.1	Vehicle Motion Measurement	74
C	Data plots	75
C.1	Tyre Data	76
C.1.1	Front Tyres	76
C.1.2	Rear Tyres	77
C.2	Spring and Damper Characteristics	78
C.3	Suspension Characteristics	80
C.3.1	Geometric	80
C.3.2	Compliance	84
C.3.3	Combined Compliant and Geometric Suspension Behaviour	85
C.4	Vehicle Behaviour	88
C.4.1	Increasing Steer	88
C.4.2	Step Steer	95
C.4.3	Modified Front Suspension Geometry - Step Steer	102
D	Tabular Data	105
E	Source Code	107
E.1	Hub Elasticity	107

List of Figures

1.1	The vehicle model	3
3.1	Simplified suspension linkage	7
4.1	Radial tyre structure, image from howstuffworks.com	11
4.2	Structure of Tyre Model	14
4.3	Structure of wheel model.	15
4.4	Tyre model test rig used in Dymola.	16
4.5	Tyre test rig at Calspan Tire Research Facility	16
4.6	Lateral force depending on slip angle.	16
4.7	Aligning moment depending slip angle.	16
4.8	Longitudinal force depending slip ratio.	16
4.9	Lateral force depending camber angle.	16
5.1	Front suspension drawing	20
5.2	Rear suspension drawing	20
5.3	Virtual rotation points of the rear five-link system.	21
5.4	Virtual rotation point of the front McPherson four-bar linkage.	21
5.5	Chassis model structure in Dymola.	21
5.6	Front suspension model structure.	22
5.7	Rear suspension model structure.	22
5.8	Spring and damper components	23
5.9	Rear anti-roll bar	23
5.10	Front camber angle, simulated geometric and measured	24
5.11	Front toe angle, geometric and measured	24
5.12	Front spring force depending on wheel travel.	25
5.13	Front damper force depending on damper velocity.	25
5.14	Seven-post rig	26
5.15	Front roll stiffness	27
5.16	Rear roll stiffness	27
5.17	Front suspension roll center movement.	27

5.18	Rear suspension roll center movement.	27
6.1	Rear subframe drawing	30
6.2	Filter step response	32
6.3	Hub elasticity loadcases	33
6.4	Front camber vs. normal load	34
6.5	Front toe vs. normal load	34
6.6	Rear camber vs wheel travel, geometric	36
6.7	Rear camber vs normal load, geometric	36
6.8	Rear camber vs wheel travel, compliant	36
6.9	Rear camber vs normal load, compliant	36
6.10	Front Steer Angles vs Lateral Force on the Right Wheel	38
6.11	Front Aligning Moment Toe Compliance	38
6.12	Rear Aligning Moment Toe Compliance	38
8.1	Slowly increasing steer, 250 deg hand wheel	44
8.2	Hand wheel steer angle vs. lateral acceleration	45
8.3	Wheel steer angles	45
8.4	Step steer experiment	46
8.5	Yaw rate comparison	47
8.6	Yaw rate comparison	47
8.7	Calculated pitch angle	48
8.8	Jacking, step steer experiment	49
8.9	Front roll centre for 2 degree roll.	51
8.10	Rear roll centre for 2 degree roll.	51
8.11	Constant turning-radius experiment, lateral acc. and roll	52
8.12	Constant turning-radius experiment, jacking	52
8.13	Roll centre movement for modified front suspension geometry.	53
8.14	Step steer experiment for modified front suspension geometry.	53
8.15	Jacking for modified suspension geometry.	54
A.1	Simplified vehicle body in side view	64
A.2	Camber angle	65
A.3	Rear and side view of a wheel, showing KPI and caster angle	66
A.4	Instant centre definition, wheel seen in front-view.	67
A.5	Roll centre definition, wheel pair seen in front-view.	68
A.6	Jacking definition, wheel seen in front-view.	68
A.7	Slip angle definition, tyre seen from above	70
A.8	Longitudinal slip definition, tyre seen in side view	71
C.1	Front tyre lateral force vs slip angle	76
C.2	Front tyre aligning moment vs slip angle	76

C.3 Front tyre longitudinal force vs slip ratio	76
C.4 Front tyre lateral force vs camber angle	76
C.5 Rear tyre lateral force vs slip angle	77
C.6 Rear tyre aligning moment vs slip angle	77
C.7 Rear tyre longitudinal force vs slip ratio	77
C.8 Rear tyre lateral force vs camber angle	77
C.9 Front spring force	78
C.10 Rear spring force	78
C.11 Front roll stiffness, less tyres	78
C.12 Rear roll stiffness, less tyres	78
C.13 Front roll stiffness, with tyres	79
C.14 Rear roll stiffness, with tyres	79
C.15 Front left camber vs. wheel travel, geometric	80
C.16 Front right camber vs. wheel travel, geometric	80
C.17 Front left camber vs. normal load, geometric	80
C.18 Front right camber vs. normal load, geometric	80
C.19 Front left toe vs. wheel travel, geometric	81
C.20 Front right toe vs. wheel travel, geometric	81
C.21 Front left toe vs. normal load, geometric	81
C.22 Front right toe vs. normal load, geometric	81
C.23 Rear left camber vs. wheel travel, geometric	82
C.24 Rear right camber vs. wheel travel, geometric	82
C.25 Rear left camber vs. normal load, geometric	82
C.26 Rear right camber vs. normal load, geometric	82
C.27 Rear left toe vs. wheel travel, geometric	83
C.28 Rear right toe vs. wheel travel, geometric	83
C.29 Rear left toe vs. normal load, geometric	83
C.30 Rear right toe vs. normal load, geometric	83
C.31 Front lateral force steer compliance	84
C.32 Rear lateral force toe compliance	84
C.33 Front aligning moment toe compliance	84
C.34 Rear aligning moment toe compliance	84
C.35 Front left camber vs. wheel travel, compliant	85
C.36 Front right camber vs. wheel travel, compliant	85
C.37 Front left camber vs. normal load, compliant	85
C.38 Front right camber vs. normal load, compliant	85
C.39 Front left toe vs. wheel travel, compliant	86
C.40 Front right toe vs. wheel travel, compliant	86
C.41 Front left toe vs. normal load, compliant	86
C.42 Front right toe vs. normal load, compliant	86
C.43 Rear left camber vs. wheel travel, compliant	87

C.44 Rear right camber vs. wheel travel, compliant	87
C.45 Rear left camber vs. normal load, compliant	87
C.46 Rear right camber vs. normal load, compliant	87
C.47 Increasing steer experiment, left turn, 11 m/s.	89
C.48 Hand wheel vs. lateral acc.; increasing steer, left turn, 11 m/s.	89
C.49 Increasing steer experiment, right turn, 11 m/s.	90
C.50 Hand wheel vs. lateral acc.; increasing steer, right turn, 11 m/s.	90
C.51 Increasing steer experiment, left turn, 22 m/s.	91
C.52 Hand wheel vs. lateral acc.; increasing steer, left turn, 22 m/s.	91
C.53 Increasing steer experiment, right turn, 22 m/s.	92
C.54 Hand wheel vs. lateral acc.; increasing steer, right turn, 22 m/s.	92
C.55 Increasing steer experiment, left turn, 29 m/s.	93
C.56 Hand wheel vs. lateral acc.; increasing steer, left turn, 29 m/s.	93
C.57 Increasing steer experiment, right turn, 29 m/s.	94
C.58 Hand wheel vs. lateral acc.; increasing steer, left turn, 29 m/s.	94
C.59 Step steer experiment, right turn, 50° hand wheel input, 11 m/s.	96
C.60 Yaw rate; step steer, right turn, 50° hand wheel input, 11 m/s.	96
C.61 Jacking; step steer, right turn, 50° hand wheel input, 11 m/s.	96
C.62 Step steer experiment, left turn, 90° hand wheel input, 11 m/s.	97
C.63 Yaw rate; step steer, left turn, 90° hand wheel input, 11 m/s.	97
C.64 Jacking; step steer, left turn, 90° hand wheel input, 11 m/s.	97
C.65 Step steer experiment, right turn, 130° hand wheel input, 11 m/s.	98
C.66 Yaw rate; step steer, right turn, 130° hand wheel input, 11 m/s.	98
C.67 Jacking; step steer, right turn, 130° hand wheel input, 11 m/s.	98
C.68 Step steer experiment, left turn, 20° hand wheel input, 22 m/s.	99
C.69 Yaw rate; step steer, left turn, 20° hand wheel input, 22 m/s.	99
C.70 Jacking; step steer, left turn, 20° hand wheel input, 22 m/s.	99
C.71 Step steer experiment, right turn, 30° hand wheel input, 22 m/s.	100
C.72 Yaw rate; step steer, right turn, 30° hand wheel input, 22 m/s.	100
C.73 Jacking; step steer, right turn, 30° hand wheel input, 22 m/s.	100
C.74 Step steer experiment, left turn, 50° hand wheel input, 22 m/s.	101
C.75 Yaw rate; step steer, left turn, 50° hand wheel input, 22 m/s.	101
C.76 Jacking; step steer, left turn, 50° hand wheel input, 22 m/s.	101
C.77 Step steer experiment, linkage joints moved upwards.	103
C.78 Jacking in step steer experiment, linkage joints moved upwards.	103
C.79 Step steer experiment, linkage joints moved downwards.	104
C.80 Jacking in step steer experiment, linkage joints moved downwards.	104

List of Tables

5.1	Mass and CG Position	24
5.2	Inertia about the CG	24
8.1	Calculated Jacking	50
8.2	Roll data	50
8.3	Calculated Jacking for Modified Suspension	52

Chapter 1

Introduction

*...for Distinction Sake, a Deceiving by Words, is commonly called a Lye,
and a Deceiving by Actions, Gestures, or Behavior, is called Simulation...*

Robert South (1643 - 1716)

The use of simulation models for prediction of vehicle behaviour has become an ever increasing part of product development and research. As the use of simulation models increases to cover a larger part of the vehicle behaviour analysis, the need for more accurate models over a broader range of handling situations is rising.

In simulation it is imperative to understand the limitations of the model and the results produced. In the analysis of simulation results one must always consider to what extent the model is valid.

All simulation models are limited by reducing the complexity of the problem to a formulation solvable by a computer in an acceptable time frame. This inevitably leads to inconsistencies between the simulation model and experimental data. These inconsistencies may be due to model formulation, simulation programming, parameter identification, numerical accuracy or low quality experimental results. [11]

In order to validate a simulation model, experimental data capturing behaviour for a range of inputs is required. Comparison between this data and simulated data is a sound method for validation. However, with larger models used in analysis of complex systems such as vehicle dynamics studies, the model may contain errors that are not observable in the comparisons. For validation of such complex systems each subsystem should be modelled and validated separately, in order to minimise sources of error. Doing this requires a deep understanding of each subsystem in order to assess the importance of accuracy for each subsystem model and what effects any deviations may have on the final simulation result. This also allows prediction of the range for which the model results may be accurate outside of that which is validated with experimental data.

1.1 Content

Problem Statement

The problem statement describes the outline of the thesis, its goals, purposes and the methodology used, as well as work related to this project.

Simulation Environment

The Simulation Environment chapter reviews the engine behind solving the equations describing the dynamic system modelled in this thesis, including a brief introduction to Modelica and the Dymola graphical modelling interface.

Tyres

The Tyre chapter describes the STI-tyre model [5] and how the implementation of it was performed for this thesis.

Chassis Modelling

The Chassis Modelling chapter presents the development of the multibody suspension and steering models, as well as spring and damper model calculations and implementations. The vehicle mass and powertrain is also included in this chapter.

Compliance

This chapter investigates possible ways of modeling the elasticities to include their effects in the simulation model. In this work a so called lumped hub elasticity formulation is formulated and investigated, along with some of the issues with implementing such a solution.

Basic Vehicle Dynamics Terminology

Readers unfamiliar with vehicle dynamics are advised to read Appendix A in order to understand the definitions and terminology used throughout this report.

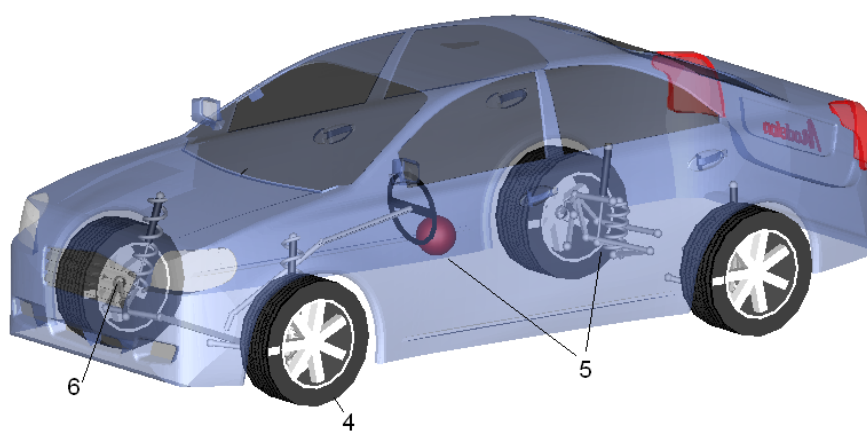


Figure 1.1: *The vehicle model, with numbered chapters, 4: Tyres, 5: Chassis, 6: Compliance.*

Chapter 2

Problem Statement

The stated problem is to develop and validate a multibody road vehicle simulation model for Handling Studies, based on publicly available parameter data not classified by Original Equipment Manufacturers (OEM), for use in further research.

The challenge of creating a full vehicle model based on parameters presented in various articles published by the Society of Automotive Engineers (SAE) and validating the entire model and its subsystems with measurement data of the actual vehicle is interesting, not only for the further research possibilities based on the resulting model but also for showing how parameter determination and experimental measurements can be re-used in projects different from that for which they were originally performed.

2.1 Goal

The goal of this thesis is to create a valid multibody vehicle dynamics model for handling studies based on public data not bound by non-disclosure agreements with any automotive manufacturer, focusing on modeling methodology and validation of subsystem behaviour individually on each level, as well as comparing vehicle measurement data from repeated driving manoeuvres with the results from full vehicle simulations of the same manoeuvres.

2.2 Purposes

Developing a multibody road vehicle model based on public data, for simulation of handling behaviour, allows the model to be free from non-disclosure agreements and therefore available for use in studies of additional systems or further handling studies. The result of a simulation is useful to the extent the simulation model has been validated, for use in severe manoeuvre simulations the model must be validated for limit handling.

Developing a model based on data gathered for other purposes also shows that it is possible to recreate results from the original studies within a different environment, with the model presented based solely on previously published parameters also showing the viability of reusing measurement data that is costly and time consuming to obtain.

2.3 Validation Methodology

In order to accept the model as valid for handling studies, each subsystem is investigated and compared to measurement data. The suspension linkages are tested on rig systems allowing input of position for analysis of geometric behaviour, spring force characteristics, pure roll behaviour as well as force and torque inputs to examine compliances. A tyre test rig is used to examine longitudinal, lateral and camber angle behaviour of the tyres, for pure and combined slip cases.

Full vehicle simulations have been carried out for several different input conditions in order to validate steady state characteristics as well as transient and frequency responses. An experiment allowing input of the kinematics and compliance test inputs in order to validate the full car rig behaviour.

Especially non-linear range behaviour is important to investigate on a subsystem level, as subsystem errors in the non-linear region are difficult to identify in full vehicle simulations. Without knowledge of the applicable range of the subsystems it is also impossible to know the limits of utility for full vehicle model studies.

2.4 Related Work

The work around the development of a real-time driving simulator model of the BMW 330i for the National Advanced Driving Simulator (NADS), presented in [12, 20, 22], as well as earlier work in development of models for use in this simulator, especially the development of tyre models [5, 14] is closely related to this work.

Chapter 3

Simulation Environment

The more constraints one imposes, the more one frees one's self. And the arbitrariness of the constraint serves only to obtain precision of execution.

Igor Stravinsky (1882 - 1971)

Describing the mechanical system of a road vehicle with traditional mechanics using rigid bodies connected to constrain motions to a predefined path is a complicated and time consuming task.

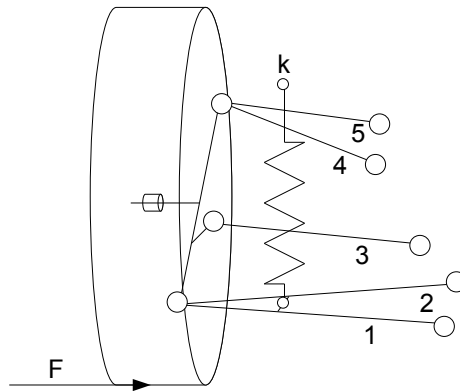


Figure 3.1: *Simplified individual suspension linkage with spherical joints*

Calculating the forces in links 1–5 and the spring k in Figure 3.1 is time consuming for a constant force F . With a varying force F and four linkages similar to the one in Figure 3.1 connected by a rigid body with mass and inertia, the equation system is growing and difficult to handle with hand calculations. If dampers are added and transient effects are to be calculated, as F varies with normal load, computer aided calculations are a necessity.

Enter the component based multibody simulation software, as the formulations describing the system can be solved by a computer, and a spherical joint constraint only

needs to be formulated generally once and then reused in every joint with the same constraints.

Modelling components separately and combining them to form a more complex system also allows the formulation to be solved at each level if each level is formulated with the same amount of equations and unknowns [6]. This also allows simplified formulations to be replaced by more complex ones as long as the constraints described are the same giving the possibility to create and solve a simplified formulation and then refine the model for more accurate results.

3.1 Modelica

Modelica is an object oriented multiphysics modeling language, for creating acausal physically oriented models. Modelica uses hierarchical models, sub models connected into larger systems to describe complex systems. This allows combinations of electrical, hydraulic and mechanical sub models in a combined system. [6]

Modelica also allows parameter and variable definition as physical properties in order to check for physical relation inconsistencies in the equations making the model description more closely related to the physical problem than a set of purely mathematical differential equations. Modelica is text based with graphical annotations allowing for fast drag-drop modelling of systems based on standard components within a Modelica editor. [15]

Modelica is designed to be able to handle very large models with more than hundred thousand equations by use of specialised algorithms, where the general Modelica model contains a set of differential algebraic equations (DAE). The model is then translated into a form that can be integrated with standard methods. [15].

3.2 Dymola

The work carried out in this thesis is performed in Dymola (Dynamic Modeling Laboratory), a multiphysics simulation environment, based on the open Modelica® modeling language. The vehicle dynamics simulations performed in this thesis also use the Vehicle Dynamics Library, a component library based largely on the Multibody Mechanics package for Dymola, this allowed for an increased modeling pace as several components could be used with only some modification.

Dymola provides a model design and editing front end with both text and graphical views, as well as a modelica translator, differential algebraic equation (DAE) solver and simulation output analysis tools. There are libraries for several engineering domains such as mechanical, electrical, control, pneumatic and hydraulic.

3.2.1 Acausal and Causal Models

An acausal model is composed of variables and the relation between these variables, the relations act as constraints between the values variables take at each instant. The simulation results consist of extracting information at certain time instants.

A causal model is a more traditional block model, with a specific set of inputs and outputs. In between the inputs and outputs are a set of equations defining the values of the outputs.

The key difference is that in causal models the data flow is explicitly from input to output. [8]

3.3 Dymola

The work carried out in this thesis is performed in Dymola (Dynamic Modeling Laboratory), a multiphysics simulation environment, based on the open Modelica modelling language. The vehicle dynamics simulations performed in this thesis also use the Vehicle Dynamics Library, a component library based largely on the Multibody Mechanics package for Dymola, this allowed for an increased modelling pace as several components could be used with only slight modification.

Dymola provides a model design and editing front end with both text and graphical views, as well as a Modelica translator, differential algebraic equation (DAE) solver and simulation output analysis tools. Libraries for several engineering domains such as mechanical, electrical, control, pneumatic, hydraulic also exist.

3.4 Vehicle Dynamics Library

The libraries used in this thesis are the Vehicle Dynamics Library (VDL), Multibody Mechanics and the base Modelica library. VDL provides base classes for vehicle subsystems types such as suspensions, tyres, drivetrains and drivers as well as vehicle frames for different vehicle types. This allows faster vehicle modelling as general model types can be modified to suit the current problem with less time spent developing new models from base components. [4]

Chapter 4

Tyres



Figure 4.1: *Radial tyre structure, image from howstuffworks.com*

The radial pneumatic tyre is a very complex mechanical device. From the inside and out it consists of a rubber lining, a series of steel rings on the edge where the tyre seals against the rim, these are called beads. The sidewalls connect beads to the outer parts of the tyre, these consist of a rubber polyester composite, see figure 4.1. The ply is a belt of steel wire held together with rubber. This composite is often denoted the tyre carcass. The outermost layer, the tread, is made from a different type of rubber than the carcass. Since the tread is in contact with the ground its rubber composition and properties are adjusted for the tyre application, e.g. the working temperature range differs greatly from a snow and ice tyre to a racing tyre.[26, 23]

4.1 Tyre Models

Over time a number of models to simulate the behaviour of tyres have been developed, the first being steady state models based on physical interpretations of tyre properties for the vehicle and aircraft industry in the 1940's. These early models only described the

relation between slip and developed force. The first empirical models were developed in the 1960's, based on the friction circle criterion, with equations describing lateral force depending on longitudinal force and slip. Since then development of existing models and new physical and empirical interpretations have been presented in various articles, one of the most important being the "Magic Formula" presented in 1987 based on a joint operation of Volvo and Technical University Delft by E. Bakker and H.B. Pacejka. [18]

$$\begin{aligned} F_y &= D \sin(C \arctan(B\alpha - E(B\alpha - \arctan(B\alpha)))) \\ B &= \frac{C_\alpha}{CD} \\ D &= \mu F_z = F_{y,peak} \\ C_\alpha &= c_1 \sin\left(2 \arctan\left(\frac{F_z}{c_2}\right)\right) \end{aligned}$$

Development of several other models has led to many ways of achieving accurate results, depending on the requirements of the simulation and available computational power model selection should be done to allow for sufficient results requiring as little parameter determination and computer calculation time as possible.

4.2 The STI Tyre Model

The tyre model used is based on the STI tyre model, developed by Systems Technology Inc. for use in the National Advanced Driving Simulator (NADS). It is a semi empirical tyre model based on a physical composite slip formulation, where calculation of the contact forces is done by determining the composite slip (σ) which is a function of longitudinal and lateral slip. This parameter (σ) is used in a polynomial force saturation function determined by four shaping parameters.

The National Advanced Driving Simulator is a real time driving simulator for studies of driver-vehicle interactions, therefore all simulation models used in it must be able to run in real time. Because of this the tyre model has to be accurate but still simplified enough to be solved in real time.

Longitudinal slip in the STI tyre model is defined as the ratio S , which is the differential tyre patch to ground longitudinal velocity divided by the longitudinal velocity of the wheel hub to the ground. [5]

$$S = \frac{v_x - R\omega}{v_x}, v_x \neq 0 \quad (4.1)$$

Slip angle, α , is defined as the angular difference between the direction of which the tyre is pointing and the actual direction of travel.

$$\alpha = \arctan\left(\frac{v_y}{v_x}\right) \quad (4.2)$$

A composite slip parameter (σ) is then determined from the lateral and longitudinal slip components and the tyre contact patch length.

$$\sigma = \frac{\pi a_p^2}{8F_z} \sqrt{\frac{K_s^2 \tan^2 \alpha}{\mu_{py}^2} + \frac{K_c^2}{\mu_{px}^2} \left(\frac{S}{1-S}\right)^2} \quad (4.3)$$

Initial contact patch length (a_{p0}) is determined by tyre width (T_W), tyre pressure (T_p), rated design load (F_{ZT}) and normal load (F_z). This is used to calculate the actual contact patch length (a_p), which also varies with the ratio between longitudinal force (F_x) and normal load (F_z).

$$a_{p0} = \frac{\sqrt{F_z F_{ZT}}}{T_W T_p} \quad (4.4)$$

$$a_p = a_{p0} \left(1 - K_a \frac{F_x}{F_z} \right) \quad (4.5)$$

Given the composite slip parameter (σ) a force saturation function called normalised composite force, a polynomial shape function based on empirically set parameters C_1 to C_4 .

$$f(\sigma) = \frac{F_c}{\mu F_z} = \frac{C_1 \sigma^3 + C_2 \sigma^2 + C_3 \sigma}{C_1 \sigma^3 + C_3 \sigma^2 + C_4 \sigma + 1} \quad (4.6)$$

Equations 4.1 to 4.6 are explained in [5].

The longitudinal force (F_x) is dependent on the longitudinal coefficient of friction (μ_x) and normal load, the force saturation function $f(\sigma)$, the transitional stiffness (K'_c) and the longitudinal slip (S). The lateral tyre stiffness (K_s) and transitional tyre stiffness (K'_c) coupled with respective slips accounts for the reduction of available force due to combined slips.

$$F_x = - \frac{\mu_x F_z f(\sigma) K'_c S}{\sqrt{K_s^2 \tan^2 \alpha + K'^2_c S^2}} \quad (4.7)$$

The lateral force (F_y) is dependent on the lateral coefficient of friction (μ_y), the force saturation function $f(\sigma)$, lateral tyre stiffness (K_s) and slip angle (α). The lateral tyre stiffness (K_s) and transitional tyre stiffness (K'_c) coupled with respective slips accounts for the reduction of available force due to combined slips. The added factor is the primed camber stiffness (Y'_γ) multiplied with the camber angle (γ) which gives the lateral force component due to camber angle.

$$F_y = - \frac{\mu_y F_z f(\sigma) K_s \tan \alpha}{\sqrt{K_s^2 \tan^2 \alpha + K'^2_c S^2}} + Y'_\gamma \gamma \quad (4.8)$$

4.2.1 Model Implementation

The STI tyre model force calculations as described above were first implemented in MATLAB® as a script with parameter inputs for slip angle (α), longitudinal slip (S), camber angle (γ), and Normal load (F_z).

As MATLAB solves input equations from top to bottom and the contact patch length (a_p) function requires longitudinal force, the MATLAB model first calculates the longitudinal force based on initial contact patch length (a_{p0}) and then recalculates the contact patch length and the longitudinal force.

This model outputs accurate results for the input parameters provided, however, as input is limited to discrete values this model was only used to verify that the calculations based on parameter data for the tyres used are valid.

The force calculations were then inserted as a Modelica calculation block with input parameters longitudinal velocity (v_x), lateral velocity (v_y), rotational velocity (ω),

effective rolling radius (R_e), inclination angle (γ) and normal load (F_z). This block calculates the contact forces and moments and supplies them as outputs.

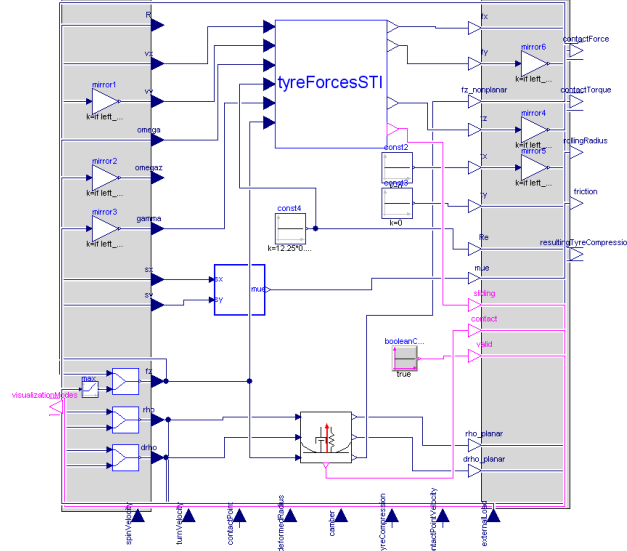


Figure 4.2: *Structure of Tyre Model*

The force calculation block is inserted into a tyre model template which interprets input parameters, handles input conversions for wheels mounted on the right side of the vehicle, as well as handling inputs depending on if the tyre model is used in a planar model simulation or a full dynamic simulation, see figure 4.2.

In this template a block is added to provide road friction coefficient for the contact patch coordinates. Another calculation block is added to calculate normal load depending on tyre vertical dynamics, tyre vertical compression (ρ), compression rate ($d\rho$) and vertical load. The block also provides a boolean value showing if the tyre is in contact with the ground or not.

Calculation of effective rolling radius can also be performed, the measured effective rolling radius is different than the compressed wheel radius, Blundell and Harty approximate the free rolling radius R_e to the loaded radius R_l plus $2/3 \rho$. [7]

However as the parameter set provided in [22, 13] suggests a constant value, this value is used in this implementation of the model.

The tyre force model is inserted in a wheel model, see figure 4.3. This model provides the input forces, velocities and positions from the hub. It also provides the ground friction at the given position. A wheel model is also extended from this wheel model to provide appropriate input parameters for the given wheel and tyre, including size parameters, tyre data friction properties and stiffness.

Tyre Dynamics

modelling the tyre force dynamics accurately is important especially for high frequency manoeuvres, for example the step steer experiments described in Section 8.1.3.

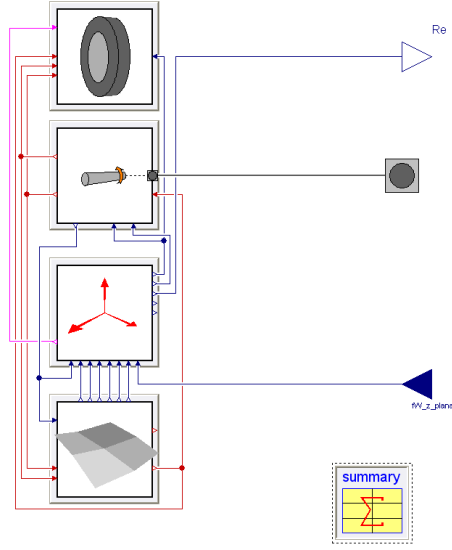


Figure 4.3: Structure of wheel model. Model blocks; visualization, hub, tyre forces and tyre-ground contact.

The tyre dynamic behaviour presented in [22], replaces the static slip definition with a first order differential formulation fit to measurement data of the longitudinal and lateral slip buildup.

$$\dot{S} + \frac{|v_x|}{\lambda} S = \frac{|v_x| - r \omega \operatorname{sign}(v_x)}{\lambda} \quad (4.9)$$

$$\frac{d \tan(\alpha)}{dt} + \frac{|v_x|}{\beta} \tan \alpha = \frac{v_y}{\beta} \quad (4.10)$$

In equation 4.9, 4.10 parameters λ and β are the longitudinal and lateral relaxation lengths, the distance the tyre travels before developing the steady state force. [20]

4.3 Tyre Model Results

For evaluation of the tyre model a tyre rig experiment was used, where sweeps over longitudinal and lateral slips as well as over camber angles can be performed for several load cases. The rig is made to resemble rigs used for testing real tyres, giving the opportunity to compare the same behaviour the tyres will experience. In Figure 4.4 the rig for testing the tyre model is shown and Figure 4.5 show a test rig at Calspan Tire Research Facility.

Front wheel tyre data is presented in Figure 4.6 - 4.9, data for the rear tyre can be found in Appendix C.1. Lateral force and aligning moment for the slip angle sweep is displayed in Figure 4.6 and Figure 4.7, longitudinal forces for the slip ratio sweep in Figure 4.8 and lateral force for the camber angle sweep in Figure 4.9.

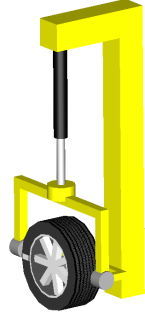


Figure 4.4: Tyre model test rig used in Dymola.



Figure 4.5: Tyre test rig at Calspan Tire Research Facility, image from calspan.com.

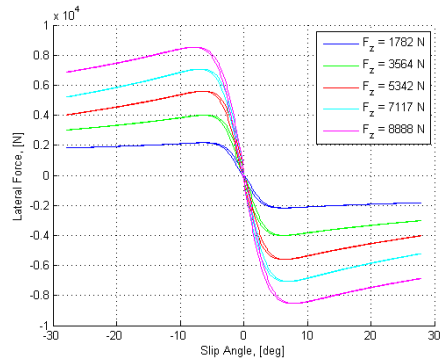


Figure 4.6: Lateral force depending on slip angle.

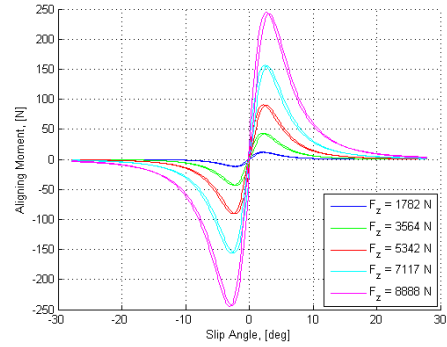


Figure 4.7: Aligning moment depending slip angle.

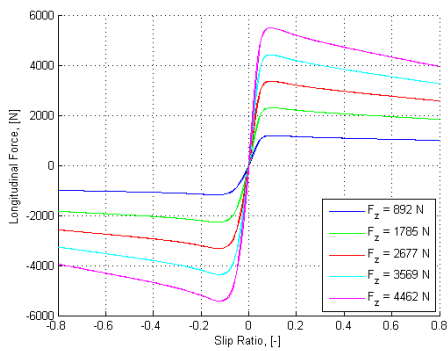


Figure 4.8: Longitudinal force depending slip ratio.

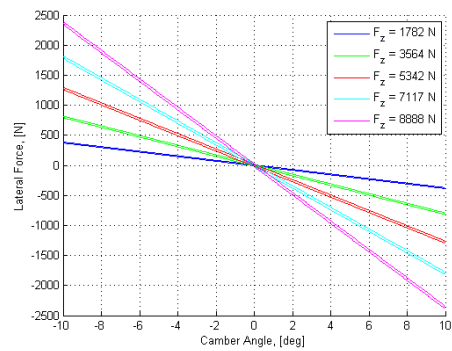


Figure 4.9: Lateral force depending camber angle.

4.4 Tyre Model Validation

The STI-tyre model itself is validated in [5, 14] and the data parameters set for the Bridgestone tyre force calculation is presented and validated in [22]. Other than what is presented in these articles, no measurement data have been available and therefore only visual comparisons for the implemented model has been possible. These comparisons were performed by visually examining the extreme values, such as peak forces, and several data points in between. As far as it is possible to observe, the implemented model corresponds very well to the simulation data in [22].

Chapter 5

Chassis

To achieve a credible result from vehicle dynamics simulations for near limit handling manoeuvres, it is vital to accurately model the load transfers. If the tyre model is not provided with the correct loads and the suspension kinematics are not captured in detail, the model will be unable to return accurate forces to accelerate the vehicle, no matter how exact the tyre model is.

5.1 Vehicle Topology

The vehicle studied in this thesis uses a McPherson strut type front suspension with a lower arm consisting of two separate links (1 and 2 in figure 5.1). The chassis joints of the lower arm are mounted with bushings while the outer are spherical joints. A third link, the steering rod (3 in figure 5.1), is attached to the steering rack and the upright by spherical joints. In a McPherson strut the lower part of the damper is rigidly mounted to the upright while the top is mounted to the chassis, the spring is fitted around the damper (4 is the upright, 5 the damper in figure 5.1). On the vehicle the damper top mount consists of a rubber bushing. The spring is mounted to the chassis frame. The McPherson strut constrains the original six degrees of freedom of the upright by one displacement constraint for each of the two lower separate links, the strut itself adds two additional constraints by a displacement constraint on the top mount and rigid lower mount. Effectively constraining four of the original six degrees of freedom, the remaining two are controlled by the steering rod and the spring.

The rear suspension is a five link type, meaning the upright is mounted with five individual links with rubber bushings at both ends (1-5 in figure 5.2). These links are geometrically located in the same manner as double wishbones with a toe link, though the separate mounting points allow mounting on the upright closer to the chassis while maintaining the virtual rotation point near the centre of the wheel, see figure 5.3. The five individual links each constrain one degree of freedom each and the spring controls the motion in the remaining path.

5.2 Multibody modelling

The chassis model consists of several submodels, each described by its own class. The vehicle chassis model itself only contains a frame with attachments for subcomponents,

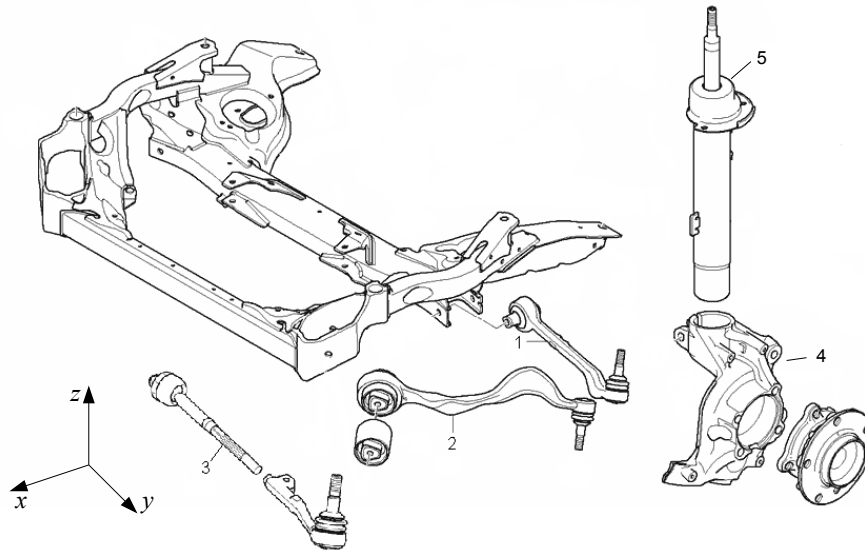


Figure 5.1: Front suspension drawing, image from bmwfans.info

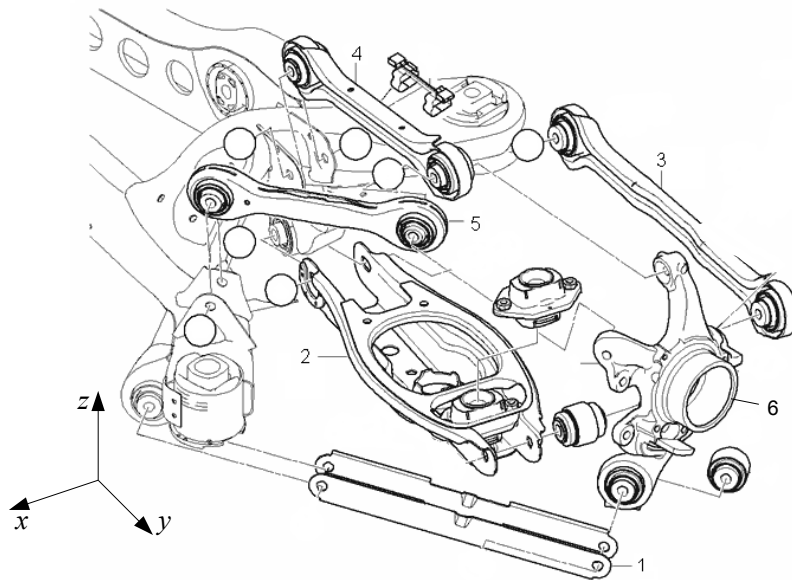


Figure 5.2: Rear suspension drawing, image from bmwfans.info

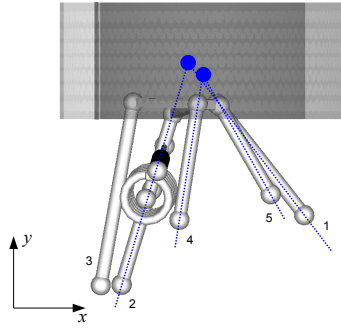


Figure 5.3: Virtual rotation points of the rear five-link system.

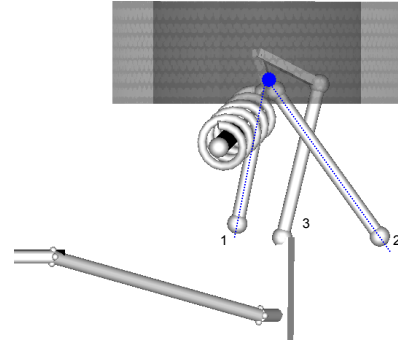


Figure 5.4: Virtual rotation point of the front McPherson four-bar linkage.

this model defines that the vehicle has four wheels, attached to two suspension models. It also defines that a body model containing mass and inertia must be included. Figure 5.5 shows the structure of the chassis model.

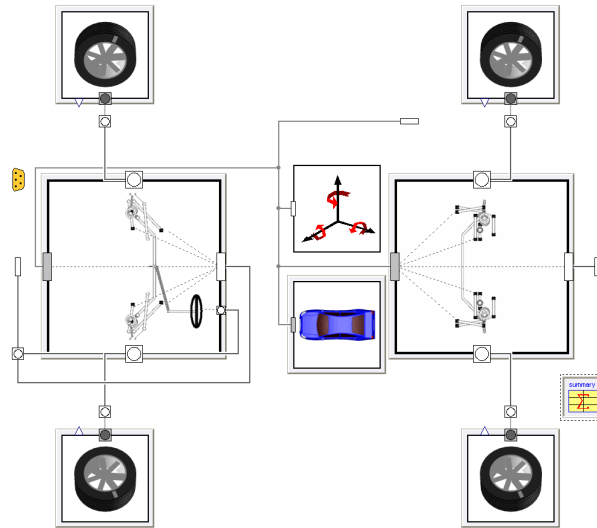


Figure 5.5: Chassis model structure in Dymola.

As the vehicle studied in this thesis has individual front and rear suspensions, the suspension models are very similar. The key difference is that the front suspension is steerable and therefore includes a steering rack. The suspension model is made up of two linkages, one for each wheel, mounted to a subframe which is rigidly attached to the chassis frame, the steerable suspension model also connects the steering rack to each of the linkages. The suspension model also allows the connection of a torsional spring between the two linkages representing the anti-roll bar. Spring and damper data is also placed in the suspension model for each linkage. Figures 5.6 and 5.7 show the front and rear linkage model structures.

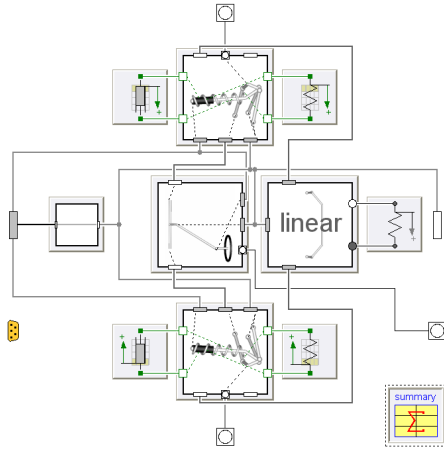


Figure 5.6: *Front suspension model structure.*

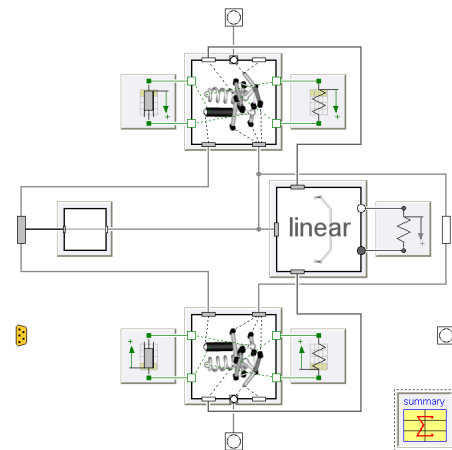


Figure 5.7: *Rear suspension model structure.*

5.2.1 Kinematics

The linkages in an independent suspension are modelled with a hub flange providing connection to the wheel. A bearing connects the hub flange to the upright, a rigid body on to which the suspension links are attached. The links are also connected to the suspension subframe, which is rigidly mounted to the vehicle body. A link consists of a rigid rod with a mass and two joints. A spring and a damper component is also inserted into the linkage, these are connected to the subframe at one end and a moving component at the other.

Several types of joints may be used to connect bodies. The most common joint in vehicle modeling is a spherical, which constrains a given point on a body to another in translation but allows rotation around all axis.

The revolute joint is a more restraining type of joint, it also constrains translation, but only allows rotation around one axis. A revolute joint may be designed by placing two sphericals side by side, the axis through the centres of both sphericals forms the axis of rotation for the revolute joint.

A universal joint is the option in between revolute and spherical, it allows rotation around two axes, meaning it behaves much like a spherical but locks rotation around one axis. A universal joint can be created by placing two revolute joints so that their respective axis coincide orthogonally.

The bushing joint connect two bodies by a series of springs and dampers. This joint is described in-depth in the compliance chapter below.

A prismatic joint allows the connected body to translate along a predefined axis, by constraining all three rotational and two of the translational degrees of freedom.

5.2.2 Springs and Dampers

Coil spring and translational damper components mainly consist of two mounting points, that are able to move relative to each other on an axis. Depending on the relative position between the mounting points a, force is applied along the respective axis for the spring

component. For the damper a force is applied in a similar manner, only depending on relative velocity instead of position.

The force characteristics of the spring and damper components are generally set in the suspension model. The characteristic can be described as linear with an optional non linearity in the form of a bump stop at a specified distance, or be entered in tabular form as discrete measured data points in order to include the full nonlinear behaviour including bump stops. As the spring length is defined in the model by the input parameter distance between the mounting points, a pre-tension can be added in order to maintain the correct static ride height. Figure 5.8 shows a coil spring model in the rear suspension.

The anti-roll bar may be modelled as a torsional spring attached to a linkage connecting to the suspension, the force developed in the anti-roll bar is described by a force-rotation relation. The non-linear behaviour can often be captured by accurately modelling the linkage to the anti-roll bar, however the design of some commercial road vehicle anti-roll bars are not pure torsional springs and may require additional attention. It is also possible to use a simplified model, only depending on the vertical position of each wheel hub relative to each other, giving a linear relation of relative wheel travel and anti-roll bar twist. Figure 5.9 shows a torsional spring model for the rear anti-roll bar.

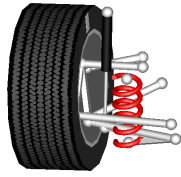


Figure 5.8: Spring and damper components in an independent suspension.

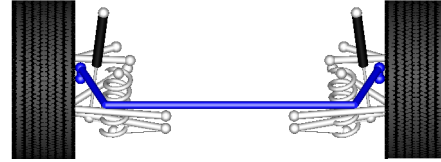


Figure 5.9: Rear anti-roll bar, connecting left and right suspension.

5.2.3 Modelling the Vehicle

Chassis

The vehicle studied in this thesis, a BMW 330i model year 2006, is modelled as a full four wheel dynamic model. Suspension subframes are modelled rigidly attached to the vehicle frame, vehicle mass and inertia is entered as a point mass at the centre of gravity with measured inertia about all three axes. For all driving tests the vehicle mass includes driver and data acquisition system masses [22].

The full vehicle measurements describe the entire vehicle mass and inertias. As some of the mass is located in the wheel and suspension linkages, these are not carried by the springs, the wheel, hub and upright masses are therefore inserted in respective components and subtracted from the overall vehicle mass. The vehicle body inertias are re-calculated based on the static ride height coordinates to the unsprung masses. As the inertia contribution of the unsprung masses are handled by the multibody environment,

Table 5.1: Mass and CG Position

	Sprung mass [kg]	CG Height over ground [m]	Front Axle to CG [m]	CG Off Center [m]
With driver and instrumentation	1539	0.5328	-1.3949	-0.0011

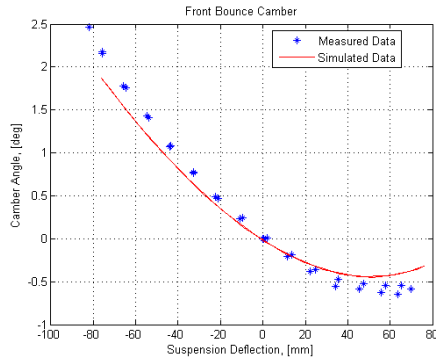
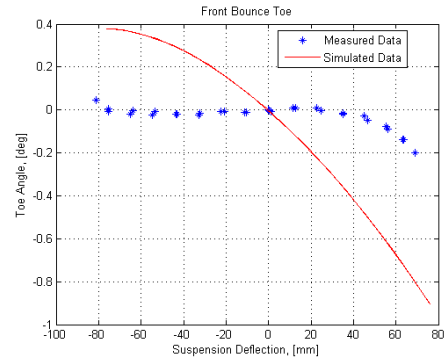
Table 5.2: Inertia about the CG

Load Condition	I_{xx} [kgm ²]	I_{yy} [kgm ²]	I_{zz} [kgm ²]	I_{xz} [kgm ²]
With driver and instrumentation	462	2186.1	2325.5	42

arbitrary small masses are used in suspension links for numerical purposes. The new body mass and inertia properties can be seen in table 5.1, 5.2.

Suspension

The suspension components are modelled as individual linkages mirrored to form a symmetric suspension model. All joints used are spherical except the rear roll over strut, which uses a universal on the inside joint to avoid rotation of this link as the spring and damper are mounted on it. Figures 5.10 and 5.11 show the behaviour of the geometric suspension models.

**Figure 5.10:** Front camber angle, simulated geometric and measured**Figure 5.11:** Front toe angle, geometric and measured

Springs and Dampers

The spring force is modelled using a tabular force characteristic calculated from wheel force measurements via a non-linear motion ratio captured from the geometric simulation

model.

The damper data is modelled using a tabular force characteristic based on a curve fitted cubic spline function of measured data from a shock absorber testing rig [22]. Both spring and damper components are connected at the same location in the model as on the actual vehicle for accurate motion characteristics at large deflections.

Vehicle

In order to accurately run some experiments, the chassis model requires a drivetrain to allow velocity control. This is done by creating a vehicle model in which the chassis is coupled with a drivetrain and brakes creating additional controllable inputs for acceleration, braking and turning.

5.3 Chassis Model Validation

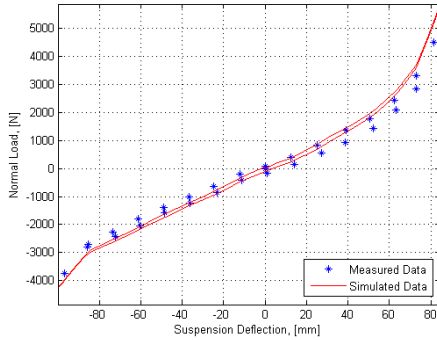


Figure 5.12: *Front spring force depending on wheel travel.*

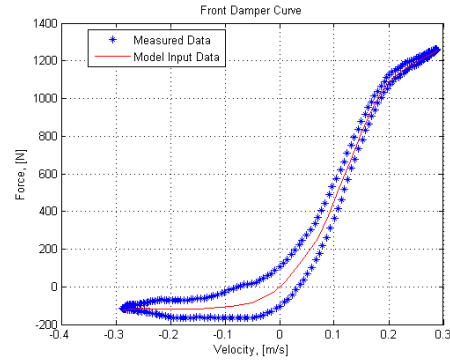


Figure 5.13: *Front damper force depending on damper velocity.*

The spring characteristics are tested in a one axle suspension rig with inputs similar to the suspension motion from the measurement data. The hub position is controlled by an actuator, driving the suspension through the wheeltravel range both in bump and roll. This allows validation of spring and anti-roll bar characteristics, see figure 5.12 and appendix C.2, as well as identification of the kinematic suspension properties. As no measurement data other than mounting point coordinates is available for the geometric suspension behaviour, the mounting point coordinates and the resulting geometric model must simply be accepted as valid and the suspension properties investigated further with compliance effects included.

Bounce and roll stiffness tests were also performed for the full vehicle model in a seven-post rig, figure 5.14, similar to the one used in the kinematics and compliance measurements presented in [19]. This was done in order to validate tyre model vertical stiffness as well as the stiffness of the coupled tyre-spring system.

The damper model is validated by comparing the idealised tabular damping curve with measurement data from damper tests at 1 Hz, presented in figure 5.13. The undamped natural frequency is around 1.5 Hz

$$(2\pi f)^2 = \frac{k}{m}$$

The velocity and steering controllers used, are taken straight from the Vehicle Dynamics Library without adjustments as no severe inputs are used, only low throttle applications to maintain a constant velocity and controlled curve radius.

5.3.1 Chassis Analysis

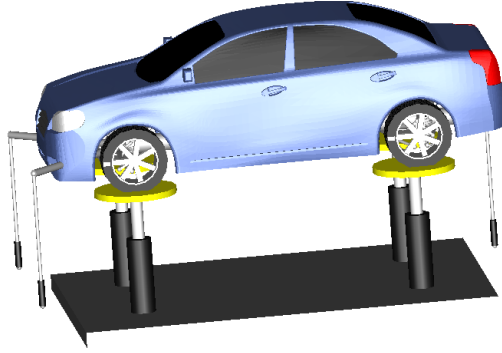


Figure 5.14: *Seven-post rig used for full chassis analyses.*

A rig for full vehicle chassis investigation was created to mimic the one used in the SEA K&C test report, in order to both validate the simulation results as well as investigating if there were any measurement errors. As the measurement results overdefine the system, the validated subsystems can be used for investigating possible measurement errors in [19], for example that the roll data from the K&C test is not pure roll. The full vehicle chassis rig also allows verifying tyre vertical dynamics in series with suspension dynamics.

5.3.2 Roll Centre

Roll centre investigations were performed by measuring the instant rotation of the hub flange with a sensor in the simulation environment and projecting this point on the YZ-plane, calculating the vector from the instant centre to the contact patch of the respective tyre and finding the intersection of these vectors, a method similar to that presented in [2]. In doing this the compliant effects on the roll centre were also accounted for. As the bushings in the real suspension would also affect the roll centre, this should yield a more accurate result than looking at the purely geometrical roll centre. However,

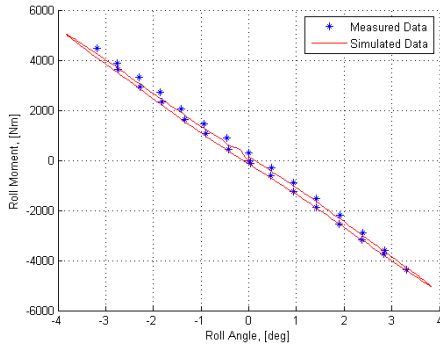


Figure 5.15: *Front vehicle roll moment depending on roll angle.*

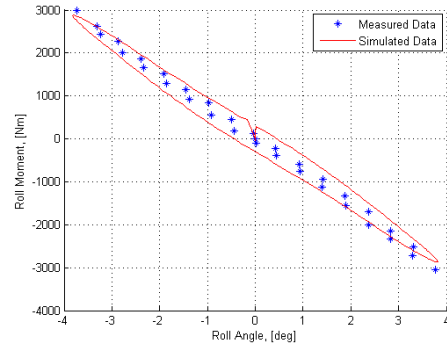


Figure 5.16: *Rear vehicle roll moment depending on roll angle.*

as the driving simulation results show, for lumped hub elasticities this is not the case, see section 8.1.6.

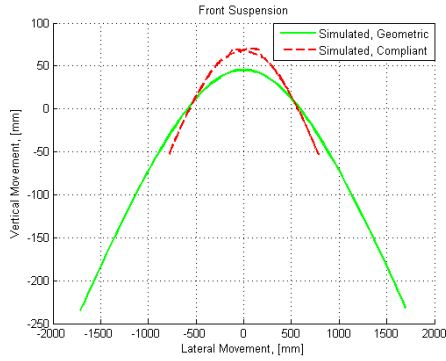


Figure 5.17: *Front suspension roll center movement.*

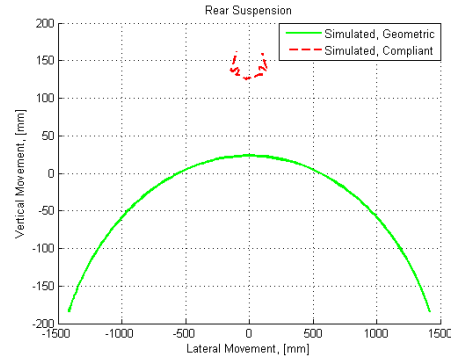


Figure 5.18: *Rear suspension roll center movement.*

5.4 Kinematics Validation

Kinematics can not be validated without including the elasticity effects. The pure geometrical behaviour of the suspension can not be measured, as elasticities affect the measurement results severely. The suspension pickup points are therefore accepted as accurate and only validated with measurement data including the elasticities. See section 6.2.

The kinematic suspension rig simulation results are presented in Appendix C.3.1.

Chapter 6

Compliances

Elastic components referred to as bushings are used in many joints throughout road vehicles. Their purpose is to reduce friction in joints, transfer loads to a larger area and to introduce some flexibility in order to minimise vibration, wear and noise. Play in bearings and deflection in stiff links and mounts under severe load conditions also show as compliant behaviour.

Bushings are often used to mount suspension components and subframes in order to provide some flexibility in the joints to reduce transmission of road harshness to the passenger compartment, as well as reducing peak loads on mounting points. Vehicle handling behaviour can be tuned using varying stiffness in suspension joints allowing a certain amount of deflection in strategic places in order to achieve the desired behaviour. Elasticities are also used in the steering system in order to provide appropriate level of feedback from the tyre to the steering wheel in combination with geometric steering effects.

Changing vehicle handling and ride behaviour via tuning of elasticities is cheaper than to redesign geometry which requires new castings, stamped or welded structures. Because of this the understanding of compliance effects are vital in road vehicle engineering.

6.1 Compliance Modeling

When modeling suspensions rigid bodies are often used since most components in the suspension system generally can be considered rigid. However, joints are often designed with elastic bushings resulting in a system with a characteristic differing from the purely geometrical. This is due to the load dependent behaviour of the joints.

In modeling for handling studies, capturing this load dependent behaviour often plays a vital role in achieving accurate results. To accomplish this elasticities must be introduced into the rigid body model. This can be done by using bushing elements in the joints where bushings are mounted on the actual vehicle or by introducing a simplified model of the elastic behaviour at the wheel.

A bushing joint typically has six DOF, three translational and three rotational, for joints with small deformations linear stiffness and damping can be used. For larger deformations non linear relations should be used. [25]

Modeling a bushing joint requires the anisotropic characteristics, both linear stiffness

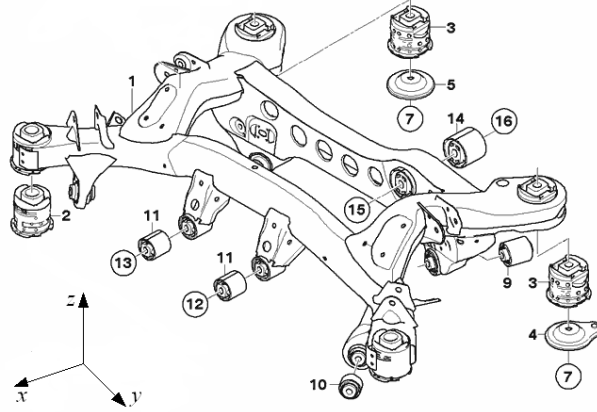


Figure 6.1: *Rear subframe drawing with bushings.*

and damping must be described in all translational and rotational degrees of freedom. For calculation this is entered in the diagonal of six by six stiffness and damping matrices respectively. A non linearity is commonly introduced in the form of an increased stiffness at a certain deflection in order to keep deformations reasonable as the bushings often are mounted in steel housings. Care must also be used when defining the axis of the bushing element in the model so that the anisotropic behaviour is accurately defined.

With the addition of elasticity in a joint described by stiffness and damping matrices, the number of degrees of freedom is vastly increased, as the motion of the interconnecting components is described by the stiffness and damping, instead of rotating about a fixed position. This leads to more equations to solve, thus more CPU time.

Correct measurements of individual bushing elements requires two things, a consistent ambient temperature during measurements and the correct pre-loading conditions. In order to achieve the correct pre-load conditions the bushings must be pressed into the suspension members and their corresponding housings, therefore special measurement rigs must be designed for every specific component. [25]

A simplified method of describing the elastic properties in a suspension linkage is to insert a single bushing element between a rigid wheel carrier and the wheel, significantly reducing the degrees of freedom for the system. Calculating the stiffness matrix for this element is relatively straightforward with measurement data on wheel displacement and rotations under load, complications may arise as if not all diagonal stiffness elements can be determined, for example S_{33} in eq. 6.3 the F_z/δ_z stiffness can not be determined due to the large deformation in the spring, leading the information in that row and column off diagonal will be lost, they can not be included as the stiffness matrix must be inverted in the calculation of $\vec{\Delta}$.

$$\vec{F} = \mathbf{S}\vec{\Delta} \quad (6.1)$$

$$\mathbf{S}^{-1}\vec{F} = \vec{\Delta} \quad (6.2)$$

$$\mathbf{S} = \begin{pmatrix} S_{11} & S_{12} & \dots & S_{16} \\ S_{21} & S_{22} & \dots & S_{26} \\ \vdots & \vdots & \ddots & \vdots \\ S_{61} & S_{62} & & S_{66} \end{pmatrix} \quad (6.3)$$

One of the key issues with lumping elasticities into a single bushing element is that parameters dependent on normal load, f_z , are more difficult to determine than those depending on other loads as the deformation in the spring is very large in comparison with the other deformations.

Trying to work around this problem by simply mounting a rigid body instead of the spring for measurements will not give adequate results due to the changing loads in the suspension links over wheel travel.

Assessing the importance of individual bushing measurements compared to wheel only deformations is difficult without the possibility to analyse both. However, as the development in elastic components is progressing, especially for increased ride comfort the problem is a very interesting one. In order to illustrate the longitudinal translation stiffness effects, important in comfort over road joints or kerbs, with an elastic hub component this deflection will not include spring compression due to the actual movement of the upright. A simplified calculation was performed in order to evaluate effects of longitudinal stiffness.

6.1.1 Modelling the Hub Elasticity

As compliance measurements were only measured at the wheel and not on individual links, the lumped hub elasticity method is used, accurately estimating six by six stiffness matrices for ten elastic elements based on load applied at the wheel is nearly impossible.

The compliance measurements were gathered by applying a lateral force at the contact patch and measuring wheel displacement and rotation. An aligning moment load applied at the wheel provided a dataset for torque loads. Based on this data the compliance effects at the wheel were initially modelled as one bushing between the wheel bearing and the upright, the stiffness matrix of this bushing is created as a linear approximation of angular deflection around the X-axis and the Z-axis depending on lateral force and aligning moment. A damping matrix is also included corresponding to the stiffness matrix with arbitrary values to avoid resonance effects.

This solution proved incapable of describing the compliant behaviour from several loads, especially normal load, as the stiffness matrix is inverted to solve the equations the parts of the stiffness matrix that can not be provided for the stiffness diagonal from measurement data leads to the loss of information in that entire dimension.

In order to work around this a new compliant component was modelled based on a differential motion description.

$$\alpha \ddot{\vec{\Delta}} + \beta \dot{\vec{\Delta}} + \vec{\Delta} - \mathbf{K} \vec{F} = 0 \quad (6.4)$$

Where $\vec{\Delta}$ is the deformation vector, containing translational and rotational deformations. The compliance matrix \mathbf{K} contains the compliance in translation and rotation for all loads. The load vector \vec{F} contains loads in x, y, z and torques around x, y, z . See equations 6.11, 6.9, 6.10.

The differential motion description limits the rate of motion so that the deflection is not instantaneous, if the response is too fast the problem will be difficult to solve,

for example if a steering angle is applied to a wheel resulting in a lateral force and toe angle is dependent on lateral force the toe angle would change instantly resulting in a different lateral force which in turn results in a new toe angle, leading to a very stiff problem where the solution would prove very unstable if solvable.

For this the parameters α and β are determined for a low pass filter where ω determines response time, see figure 6.2.

$$\alpha = \frac{1}{(1.27\omega)^2} \quad (6.5)$$

$$\beta = \frac{2D}{1.27\omega} \quad (6.6)$$

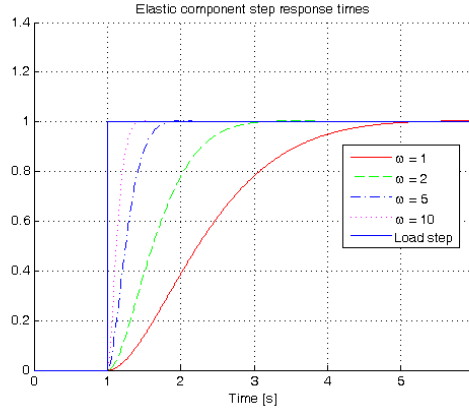


Figure 6.2: Filter step response, normalised step force plotted with normalised deflection response.

The alpha parameter is affected by mass located between the component and a force acting on it, this can be seen by substituting the force component in equation 6.4 with ma from Newton's 2nd law.

$$\begin{aligned} \vec{F} &= m\ddot{\vec{\Delta}} \\ (\mathbf{I}\alpha - \mathbf{K}m)\ddot{\vec{\Delta}} + \beta\dot{\vec{\Delta}} + \vec{\Delta} &= 0 \end{aligned} \quad (6.7)$$

The differential formulation in eq. 6.4 can be solved for \vec{F} by substituting $\ddot{\vec{\Delta}}$ with \vec{F}/m if $m \neq 0$.

$$\begin{aligned} \mathbf{I}\frac{\alpha}{m}\vec{F} + \beta\dot{\vec{\Delta}} + \vec{\Delta} - \mathbf{K} &= 0 \\ (\mathbf{I}\frac{\alpha}{m} - \mathbf{K})\vec{F} + \beta\dot{\vec{\Delta}} + \vec{\Delta} &= 0 \\ \vec{F} &= (-\beta\dot{\vec{\Delta}} - \vec{\Delta})(\mathbf{I}\frac{\alpha}{m} - \mathbf{K})^{-1} \end{aligned} \quad (6.8)$$

The behaviour of this formulation was first investigated in a 1 degree of freedom translational model, this was expanded to x-y-z translational freedom and finally including the rotational components for a full 6 DOF component. The formulation allows

definition of the compliance matrix \mathbf{K} to provide compliance in any direction depending on any load.

$$\mathbf{K} = \begin{pmatrix} K_{11} & K_{12} & \dots & K_{16} \\ K_{21} & K_{22} & \dots & K_{26} \\ \vdots & \vdots & \ddots & \vdots \\ K_{61} & K_{62} & & K_{66} \end{pmatrix} \quad (6.9)$$

Where K_{11} is compliance for translation in x by F_x , with the vector \vec{F} containing all loads and the vector $\vec{\Delta}$ containing all deformations.

$$\vec{F}^T = (f_x \quad f_y \quad f_z \quad m_x \quad m_y \quad m_z) \quad (6.10)$$

$$\vec{\Delta}^T = (\delta_x \quad \delta_y \quad \delta_z \quad \phi_x \quad \phi_y \quad \phi_z) \quad (6.11)$$

A model designer applying a formulation like the one described above must use care when parameterising the elasticities. As it out of necessity is possible to create dependencies that are physically impossible, one may be tempted to enter high order polynomial relations for the elements in \mathbf{K} in order to very accurately mimic measured data, however, this will lead to large errors outside of the measurement range. Doing this would also void the multibody formulation of the model as the elasticity behaviour will be very dominant for large deflections where it in reality will reach a bump-stop and the elastically deformed geometric non-linear behaviour will be dominant.

Approximations must also be made for loads giving a combination of elastic and geometric characteristics depending on vehicle state. A given wheeltravel may result in different load cases and deformations as the wheeltravel may be due to vehicle bounce, roll, surface disturbance or any given combined state. The formulation above is only load dependant. This limits its versatility as discussed below.

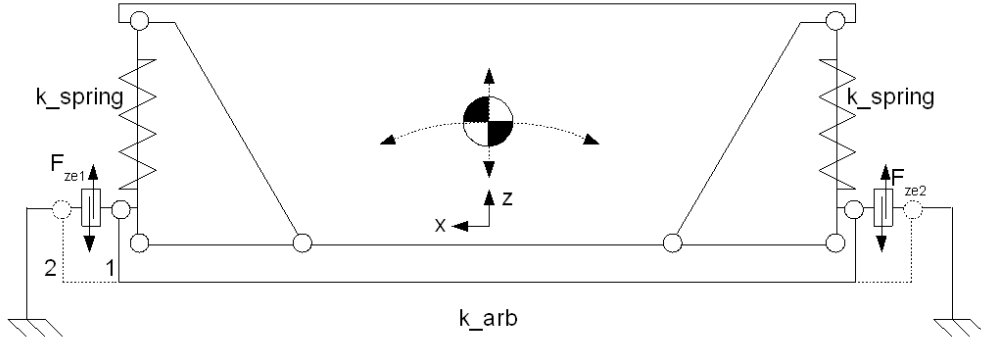


Figure 6.3: Two-dimensional illustration of the lumped hub elasticity loadcase possibilities.

The load seen by the hub elasticity (rectangle 1, figure 6.3) is dependent on where the elasticity is placed in regard to the anti-roll bar mounts. It can either be placed so that the anti-roll bar load path is outside of the elasticity (dashed line 2, figure 6.3), or so that the anti-roll bar loads the elasticity (solid line 1, figure 6.3). In a pure roll

state case 3 with elasticity parameters based on roll data is an accurate model, however in order to keep the model accurate in bounce, either case 1 or case 2 could be with elasticity parameters based on bounce data, both case 1 and 2 would provide erroneous deformations in roll with elasticity parameters based on bounce data.

The elastic deformation differs between roll and bounce, on the vehicle studied in this thesis, roll deformations are generally larger for the same load, see figure 6.4, 6.5. This means that if the elasticity parameters are determined based on roll data, a combined bounce roll motion will result in a deformation larger than that of the separated roll and bounce deformations together, as only the larger roll based parameter is used for the combined load.

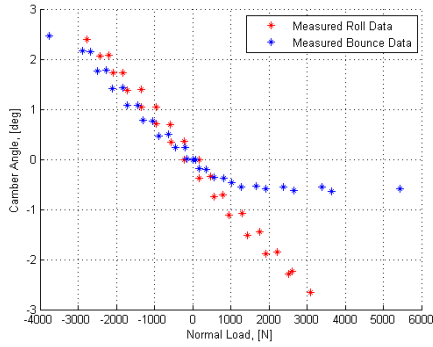


Figure 6.4: Front camber depending on normal load, measured in roll and bounce.

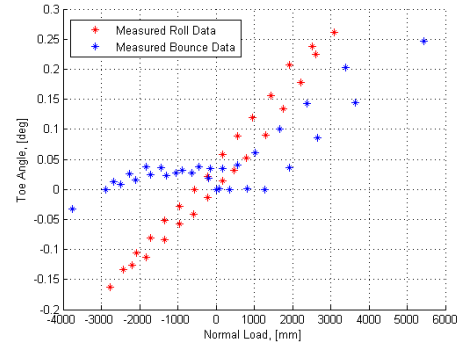


Figure 6.5: Front toe depending on normal load, measured in roll and bounce.

In order to solve this problem, one solution is to use both case 1 and 2 by dividing the anti-roll bar into two and splitting the stiffness so that a scale factor is effectively multiplied to the anti-roll bar load that the elastic component is loaded with, see equations 6.16, 6.17. By using roll based parameters one would achieve a compromise with a smaller deformation than the one measured in pure roll and a larger deformation than the one measured in bounce.

Case 1

$$F_{ze1} = z_1 k_{spring} + \Delta z k_{arb} \quad (6.12)$$

$$F_{ze2} = z_2 k_{spring} + \Delta z k_{arb} \quad (6.13)$$

Case 2

$$F_{ze1} = z_1 k_{spring} \quad (6.14)$$

$$F_{ze2} = z_2 k_{spring} \quad (6.15)$$

Combined with scale factor c , $c < 1$

$$F_{ze1} = z_1 k_{spring} + \Delta z k_{arb} c \quad (6.16)$$

$$F_{ze2} = z_2 k_{spring} + \Delta z k_{arb} c \quad (6.17)$$

A suggestion for a more advanced solution is to implement two \mathbf{K} matrices with parameters for bump and roll, using a variable scale factor based on vehicle state information. However, within this thesis there was no time to test this solution.

6.1.2 Hub Elasticity Parameter Determination

...like creating an egg from an omelet.

Johan Andreasson

In order to determine the parameters of the lumped elasticity investigations of data from a Kinematics and Compliance test, some of the parameters are straightforward as they are easily represented by a linear relation with force identified in the compliance test and parameters are suggested in [22]. These straightforward parameters include lateral force steer, K_{26} , lateral force camber, K_{24} , and aligning moment toe, K_{66} .

More difficult to determine are the compliances due to normal load, as measurements with a varying normal load also include body movement leading to geometric changes as well as elastic. In order to determine these parameters the geometric model must therefore be accepted as valid, however, as no measurements of purely geometric behaviour (i.e replacing all of the bushings with spherical bearings) were available during the work leading up to this report, this is very difficult. No geometrical models are presented in [12, 22] only geometric coordinates for all mounting points. These parameter determinations are therefore based on the assumption that these geometric coordinates are accurate and that a geometric model based on them therefor also is accurate.

Determining the elasticity parameters for normal load is done by comparing the measurement data from the kinematics and compliance test with the purely geometric model behaviour. Polynomial fit curves were then adapted to both measurement and simulation data in order to plot the difference between the curves within the measurement range. This was deemed to be as accurate as interpolating measurement points in order to obtain the numeric difference between geometric and measurement data. In determining the normal load dependent parameters, data from roll measurements were used as roll stiffness is higher than bounce stiffness and therefore puts a larger load on the elasticities. As mentioned in the previous section it is not possible to model both bounce, roll and their transitional states with a lumped elasticity. Determining parameters from the stiffest state gives the possibility to split the spring or roll load, in order to only partially load the elastic element for adjustment of behaviour for different purposes (see eq 6.16, 6.17). Applying this should be done with extreme care as it is very far from modelling the actual physical system.

The problem in modelling a lumped hub elasticity imposed by differentiating behaviour in roll and bounce is shown in figure 6.6, 6.7, simulated geometric behaviour plotted with roll and bounce measurements for both wheel travel and normal load.

In most cases the elastic relation is fairly linear, the geometric relations however, contain more or less nonlinear behaviour, especially for large suspension travels. Due to limited range measurement data and a desire to maintain the physical interpretation as far as possible, only linear elastic parameters were used in the compliance matrix. Polynomial approximations may yield closer results within the measurement range but results stray quickly outside of it.

As the issue with diverging characteristics in bounce and roll described above can not be described entirely using the lumped hub elasticity, and the nonlinear geometry causing some problems with a linear elasticity, a result close to but not exactly following the measured data is expected, see figures 6.8, 6.9.

The elastic parameters possible to determine and displaying a compliant behaviour from the kinematics and compliance measurement data were entered in the compliance matrix **K** and are marked in bold below.

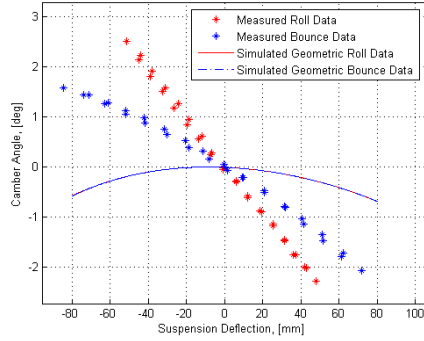


Figure 6.6: Rear camber depending on wheel travel for simulated geometric behaviour, the simulated camber is the same in roll and bounce plotted towards suspension travel.

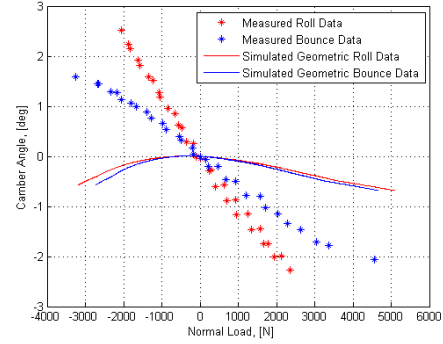


Figure 6.7: Rear camber measured and simulated geometric behaviour in bounce and roll, the camber differs slightly when plotted against normal load as the anti-roll bar applies more load in roll.

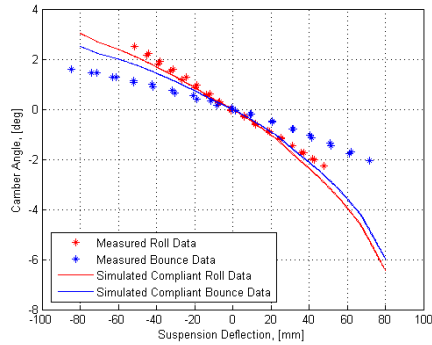


Figure 6.8: Rear camber measured and simulated compliant behaviour in bounce and roll vs Wheel travel

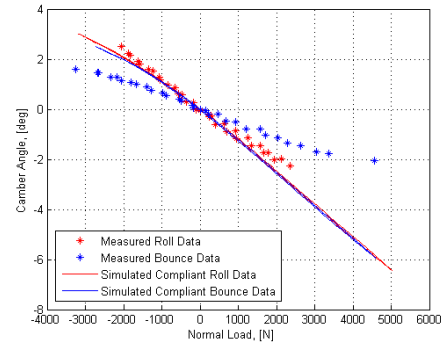


Figure 6.9: Rear camber measured and simulated compliant behaviour in bounce and roll vs Normal load

	f_x	f_y	f_z	m_x	m_y	m_z
δ_x	K_{11}	K_{12}	K_{13}	K_{14}	K_{15}	K_{16}
δ_y	K_{21}	K_{22}	K_{23}	K_{24}	K_{25}	K_{26}
δ_z	K_{31}	K_{32}	K_{33}	K_{34}	K_{35}	K_{36}
ϕ_x	K_{41}	K₄₂	K₄₃	K_{44}	K_{45}	K_{46}
ϕ_y	K_{51}	K_{52}	K_{53}	K_{54}	K_{55}	K_{56}
ϕ_z	K_{61}	K₆₂	K₆₃	K_{64}	K_{65}	K₆₆

The frequency response range for the model derived in this thesis is set to 7 Hz, selected arbitrarily as the highest frequency input in the driving tests is about 5 Hz.

In the kinematics and compliance measurements there is no information on the frequency of the force applications and therefore no analysis has been possible of the hysteresis effects in the suspension elasticities. The α and β parameters have simply been adjusted to the expected frequency response according to the filter specifications above for adequate response time with little overshoot.

6.1.3 Steering Compliance Modelling

In road vehicle steering systems elasticity exists both in the joints and in intentional elasticities used to reduce vibrations and shocks from surface imperfections reaching the driver, this gives the steering system a coupled elasticity between the front wheels different from the toe elasticity as there is a coupling between the two wheels. This elasticity is modelled as a torsional spring on the steering column with internal damping and viscous friction.

Parameter determination for the steering elasticity is based on measurement data for a lateral force applied at the right wheel contact patch, see Figure 6.10. The displacement, seen on the left wheel, will only be due to elasticities in the steering system, while the toe compliance will contribute at the right wheel. Neglecting the first few data points of the measurement, where the dynamic behaviour has not yet stabilised linear approximations show a non-zero steering angle for the unloaded case, due to free play in the steering. The steering elasticity stiffness is derived from the left wheel linear approximation for larger hand wheel steering angles, and having a very weak stiffness in the area composed of the free play. The front toe elasticity is given from the same experiment by the difference between the left and right wheel linear approximations.

6.2 Compliance Validation

Compliance effects dependent on lateral load or aligning moment are validated in suspension rigs with force or torque inputs at a point representing the tyre contact patch, see figure 6.11, 6.12 and Appendix C.3.2.

Verification of steering elasticity is done by repeating the experiment in a suspension simulation jig with the same single wheel force application. For lack of measurement data the compliant behaviour from aligning moment load could only be verified for single wheel toe and not for coupled steering.

Compliance effects dependent on normal load were validated together with geometric effects as accurate measurements can only be gathered for the combined geometric and elastic deflections, see C.3.3.

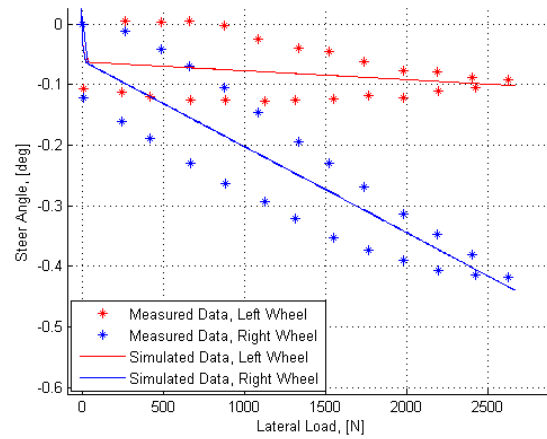


Figure 6.10: *Front Steer Angles vs Lateral Force on the Right Wheel*

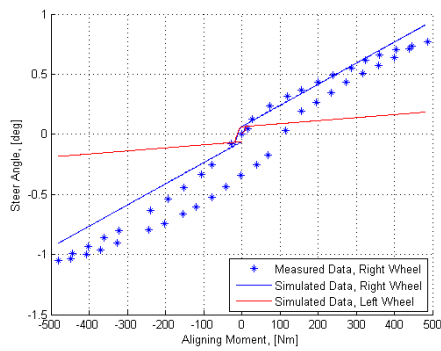


Figure 6.11: *Front Aligning Moment Toe Compliance*

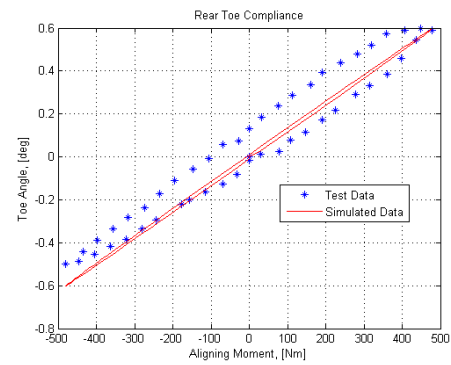


Figure 6.12: *Rear Aligning Moment Toe Compliance*

Chapter 7

Accomplishment

Within the development work and validation of a multibody road vehicle simulation model of a BMW 330i based on publicly available data, basic component based models have been created and combined with new components in order to achieve a full vehicle simulation model. Due to the limited measurement data some creative ideas have been tested and brought into play in order to use the measurement data available as effectively as possible and achieve credible simulation results.

7.1 Preliminaries

In order to develop this model based on measurements performed for the development of a Real-time simulation model for a driving simulator [12, 22], were studied thoroughly. Information regarding the methodology used in development of the NADS model as well as its predecessors and the environment they are developed for [9, 11] were also investigated.

Research work of the studied vehicle topology was also done as this was not entirely clear from the work description and articles describing parameter measurement.

A lot of effort was spent studying different tyre models in order to gain an understanding of different formulations used to model tyre behaviour, especially important here is the extensive work in [23, ?, 18].

Studying fundamental principles of multibody vehicle simulation in order to gain a greater understanding has also been important [10, 7].

Multibody modelling of vehicles in Dymola[3] using VDL[4] in the development work of Lund University's first and second Formula Student race cars as well as learning basic vehicle dynamics principles in this work has been very helpful.

7.2 Model Development Chronology

In the development of the model described in this thesis much of the work has been described in depth in previous chapters. However, as with vehicle design much of the work is iterative and a starting point must be established. Simplifications are made in order to be able to rapidly move on to the next step and reformulated for increased accuracy. A strong standpoint observed during this work has been to establish a solvable full vehicle model as quickly as possible together with solvable sub component experiments in

order to be able to test refined formulations quickly and compare them to the previous version on all levels.

7.2.1 Vehicle Parameter Identification and Modelling Sequence

Work started by gathering all known vehicle parameters from the articles and inserting them in a spreadsheet, allowing overview of what is known and what needs to be estimated. All vehicle parameters were converted to metric units and the FLU coordinate system. Geometry coordinates are presented in [22] and spring data and stiffness was gathered from measurement data files presented in [19].

A MATLAB script calculating the contact patch forces according to the formulation in [5] was created with the Bridgestone tyre parameters in [22]. This was done in order to verify that the formulation returns the correct forces over different load and slip combinations. The formulation was then translated to Modelica and inserted into a wheel model, which in turn was investigated in a tyre-rig experiment.

The suspension models were created with spherical joints based on the geometry data presented in [22].

Suspension rig experiments were used in order to compare the geometric suspension properties with measurement data from the kinematics and compliance tests in [19].

The suspension models were inserted in a general vehicle model with recalculated mass properties to account for sprung and unsprung masses. This model was investigated with several experiments in order to cross reference the measurements with tyre stiffness included.

The lumped hub elasticity was created and inserted to the suspension models, parameters for lateral load and aligning moments were determined. The normal load dependent parameters were calculated based on the difference between the geometric suspension model and the measurement data from the K&C report [19].

The chassis model was inserted into a generic vehicle model including drivetrain and driver models in order to run vehicle experiments with a maintained longitudinal velocity.

7.2.2 Iterative Approach

Within the sequence described above in 7.2.1 the creation of experiments to investigate each model level separately before combining the submodels into larger components allows many formulation errors to be found and fixed at an early stage.

For example stiffness figures presented in [22] were presented for wheel stiffness rather than spring stiffness, calculations of auxiliary stiffness for anti-roll bar parameters were also very unclear. Leading to several recalculations of these parameters as the motion ratio, especially in the rear suspension varies significantly over the suspension motion range. After recalculation of any parameter the experiments are repeated and results checked with measurement data. Results are presented in Appendix C.2.

The hub elasticity was initially modelled by a spring and damper system only dependent on lateral load and aligning moment affecting camber and toe. However, as the suspension bushings also are affected by normal load the modelled behaviour in bump and roll showed large differences when compared to the K&C measurements, this is shown in Appendix C.3.1, and the hub elasticity parameters had to be changed.

As the previously used formulation was not able to describe the elastic behaviour due to the way it is solved, a new formulation had to be developed, see section 6.1.1.

Despite using a compliance formulation in order to achieve accurate wheel angles, it is unclear whether or not the roll centre is affected by this. Depending on the definition the roll centre is either defined entirely by the instantaneous hub rotation point and the tyre contact patch or by the projected intersection axis of the suspension links. This lead to a series of simulations performed in order to determine the effects on roll centres of a lumped elasticity, results of these investigations can be found in 5.3.2 and 8.1.6.

The tyre model is another example of where an iterative approach was applied, first creating the contact patch forces in a MATLAB model for one tyre in order to verify that the model is formulated correctly. This model was then translated into a Modelica block and inserted into an existing wheel model. Then tyre vertical dynamics were modelled and inserted. This model was then generalized and extended models were created based on it in order to create separate front and rear tyre models. Tyre lateral and longitudinal dynamics were then implemented by first order differential equations on respective slips, see chapter 4.

Chapter 8

Results

In multibody vehicle dynamics simulation validating each subsystem by comparison with measured data in order to create a valid composite model is a sound method [11]. This chapter presents results for the assembled vehicle model while the validation of each subsystem is presented in its corresponding chapter.

Due to the complexity of the model and difficulties with measuring the behaviour accurately as well as repeatability of the tests, especially due to changing conditions and external disturbances, some deviations of the results can be tolerated depending on the severity of the manoeuvre.

8.1 Vehicle Simulation

The vehicle simulations are run with vehicle mass set including measurement system masses (see table 5.1), and including a generic drivetrain in order to maintain a constant velocity.

Some of the measurement data suffers from a lot of disturbance and/or poor filtering methods, and is therefore less appropriate for accurate validation. Both pitch rate and roll rate are heavily affected by noise but still provide useful transient information. Roll data in some of the slowly increasing steer driving tests is very poor with no other signals showing any event likely to cause this error.

8.1.1 Frame Resolves

The inertial sensing system mounted inside the vehicle rotates with the vehicle sprung mass, leading to measurement data sampled with this to require post processing to be presented in a non-rotated coordinate system. Lateral acceleration has been processed in the measurement data presented below, roll data is based in ultrasonic sensors combined with roll rate, pitch data is based on spring compression sensors. Further information about the measurement methods is presented in Appendix B and [12].

In the simulations the rotational vehicle motions are transformed in the order yaw, roll, pitch, giving different resolve frames for these angular motions. The yaw angle and yaw rate is resolved in the world frame, while the pitch and roll are measured relative to the world horizon. Roll rate is transformed before pitch rate meaning that the pitch rate is measured around the rotated Y-axis. This means that a fraction of the yaw rate is recorded as pitch rate which explains the constant off zero pitch rate value, while the

actual pitch stays constant relative the world horizon. The same effect can be seen in the measurement data as the pitch rate data is not post processed to compensate for roll, while actual pitch measurement is taken from the spring compression sensors showing that pitch is constant while cornering at a steady lateral acceleration, see section 8.1.3.

8.1.2 Increasing Steer

The increasing steer experiment is performed by slowly increasing the hand wheel input from an initial straight line driving, at a controlled constant longitudinal speed. The experiment is performed for six different cases (various speeds and turning directions), all presented in Appendix C.4.1. The experiment presented below is performed with a longitudinal speed of 22 m/s (80 km/h) and a hand wheel input reaching 250 degrees with a ramp of 10 deg/s, turning the vehicle to the right.

In Figure 8.1 the results of a driving experiment is presented for a model including the hub and steering elasticities, but also for a model with purely geometric suspensions.

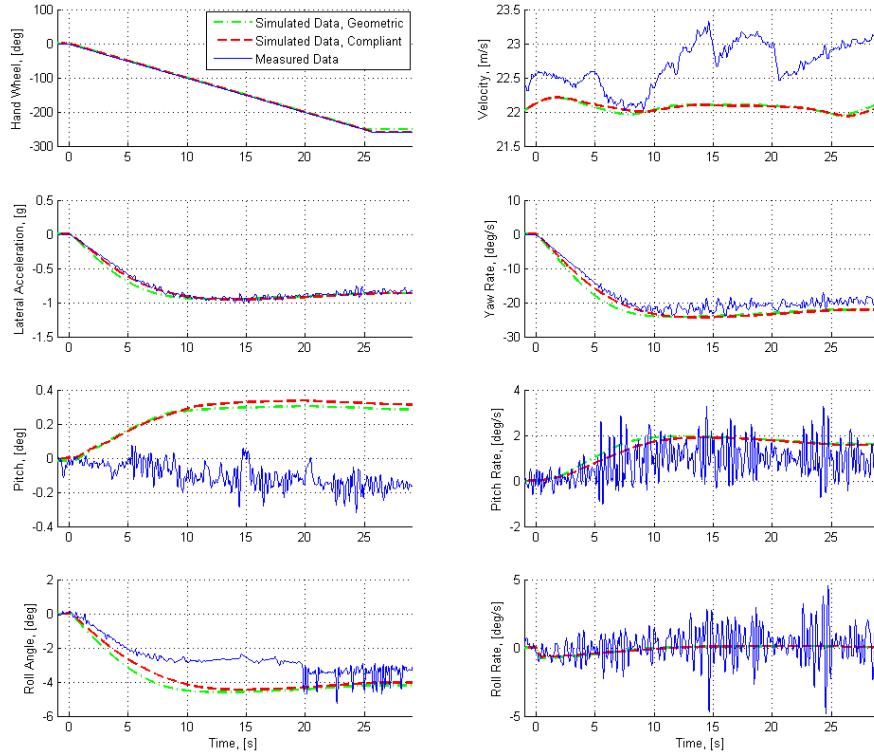


Figure 8.1: *Slowly increasing steer, 250 deg hand wheel*

In the experiment a near steady state handling of the vehicle up to limit lateral acceleration can be seen in Figure 8.2. The linear range cornering stiffness is only slightly on the high side with elasticities included. Lateral acceleration drop off is accurately captured. The vehicle model without the elastic components is also shown to illustrate

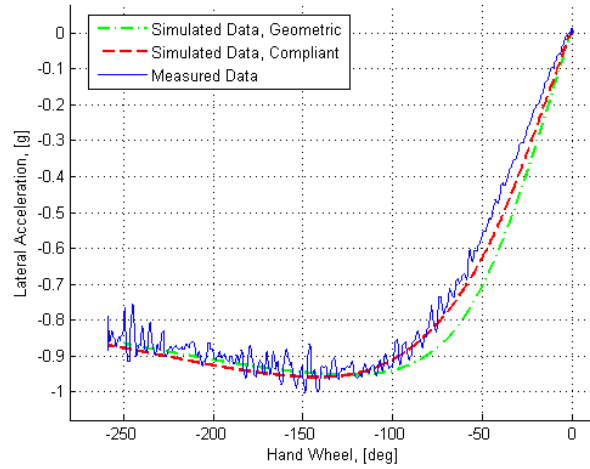


Figure 8.2: *Hand wheel steering angle as a function of lateral acceleration.*

the effect the bushings have on handling, where especially toe stiffness dramatically affects the cornering stiffness. The compliant model simulation displays a peak cornering force that is slightly too high, resulting in a higher acceleration throughout the drop off range while the drop off rate is accurate, see Figure 8.3.

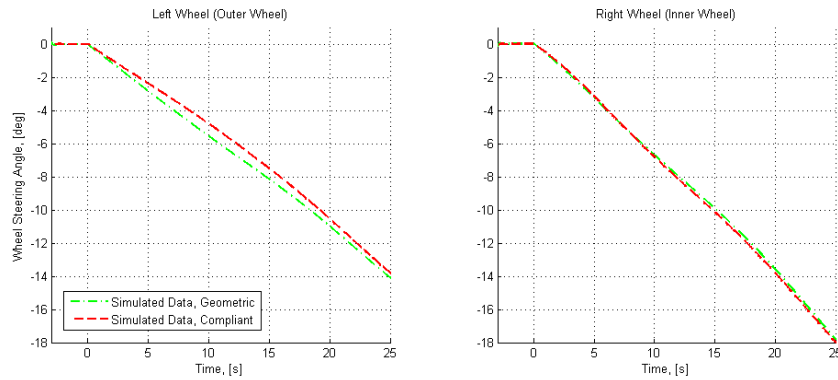


Figure 8.3: *Steer angles for left and right wheel with and without elasticity*

8.1.3 Step Steer

The step steer experiment is also performed for a constant speed, with a step steer input reaching a constant value. Since a true step input is impossible to perform, a ramp of 430 deg/s is used for all the tests.

Shown in Figure 8.4 are the simulated results together with measurement data (for four different runs of the current experiment), for a hand wheel input reaching 130 degrees (turning the vehicle to the right) at a longitudinal speed of 11 m/s. The remaining tests, with different speed and hand wheel inputs, are presented in Appendix 8.1.3.

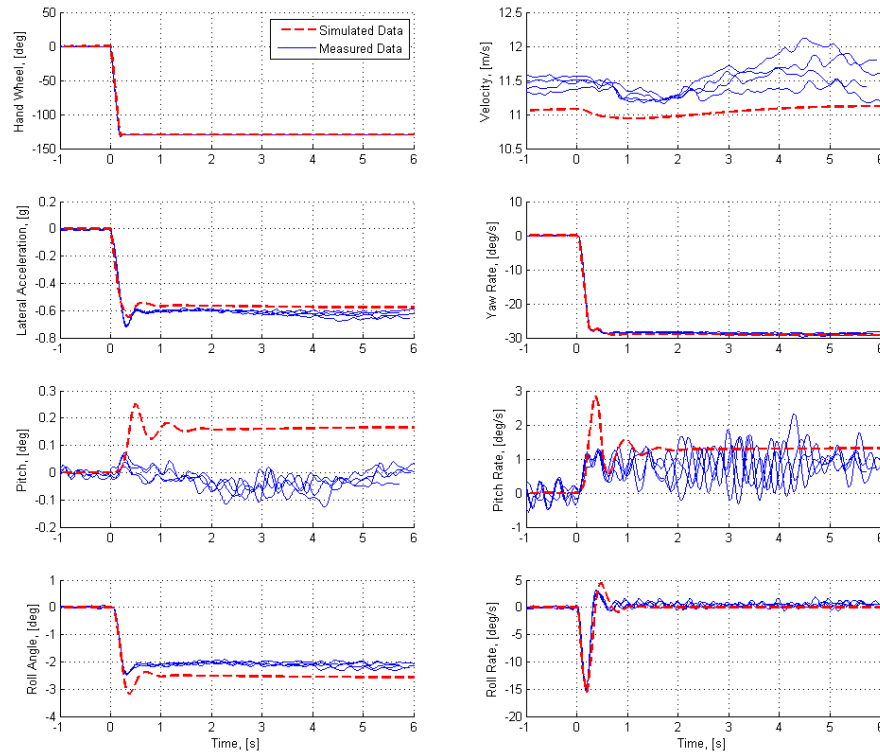


Figure 8.4: Step steer experiment, 130 degree hand wheel input turning the vehicle to the right.

Lateral Acceleration

The lateral acceleration seen in Figure C.71 is 5-10% lower in the simulation model than the measurement data, while in manoeuvres at other velocities and hand wheel inputs the simulation model gives lateral accelerations 5-10% above the measurement data. It is difficult to determine if this difference is due to acceleration measurement accuracy or incorrect load transfers as a result of roll centres discussed in 8.1.6.

Transients

In the transient phase, in the simulation result, a spike during the acceleration build up occurs (clearly seen in the lateral acceleration of Figure C.59 around 0.2 seconds), this behaviour is not seen in the measurement data. However, without any dynamics in the tyre model, the spike is even more prominent. This shows that the tyre model dynamics formulation is useful although not entirely accurate.

8.1.4 Yaw

In Figure 8.5 and Figure 8.6, as well as Appendix C.4.2, the simulated and measured yaw rate is compared with a yaw rate calculated from the lateral acceleration and longitudinal velocity from the measurement data. A difference between the calculated yaw rate and the yaw rate sensor measurement can be seen, where the calculated being higher in every test run. This does not state that the yaw rate presented in the measurement is wrong, but rather that there is an inaccuracy within these three measurement parameters (lateral acceleration, speed and yaw rate).

$$R\dot{\psi} = v_x \quad (8.1)$$

$$a_y = \frac{v_x^2}{R} = v_x \dot{\psi} \quad (8.2)$$

The yaw rate calculated from acceleration and velocity is resolved in the world frame, while the measured in the vehicle frame. However, the difference between the two resolves is rather small, as stated in Section 8.1.1, and can be neglected in this specific comparison.

This measurement error consistently gives a lower yaw rate depending on how large the roll angle is.

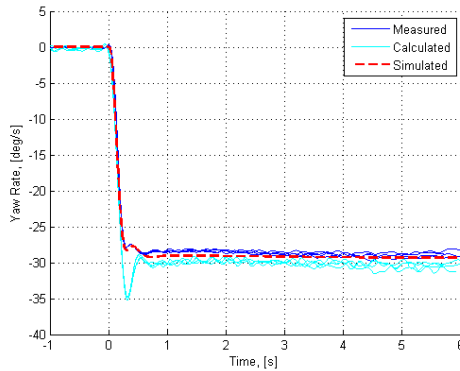


Figure 8.5: Yaw rate comparison with calculated yaw rate from measured lateral acceleration and speed, with 130 deg hand wheel input at 11 m/s

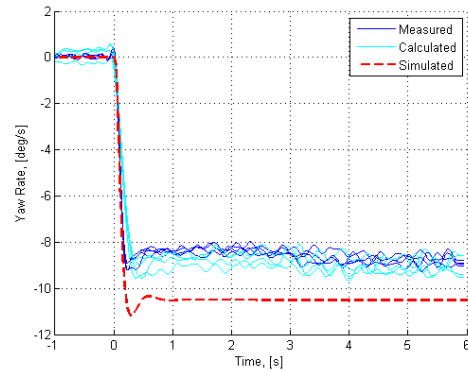


Figure 8.6: Yaw rate comparison with calculated yaw rate from measured lateral acceleration and speed, with 30 deg hand wheel input at 22 m/s

8.1.5 Pitch and Jacking

The pitch rate in the step steer experiment, see figure 8.4, shows a positive pitch rate for both the simulation and measurement results, where the pitch angle is more or less constant. This pitch rate is explained by the rolled vehicle body seeing part of the yaw rate as pitch rate. Same behaviour can be seen in the increasing steer experiment.

The simulation data shows a positive pitch angle for all experiments, while the measurement shows a near zero, but negative pitch angle. To verify that this difference is not due erroneous measurement, a pitch angle calculated from spring travel measurements is compared to both simulated and measured pitch angle, Figure 8.7. The calculated pitch follows the irregularities in the measured pitch, suggesting that this data is filtered and used in the measured pitch presented.

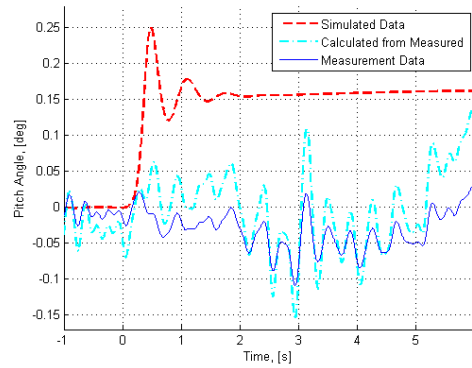


Figure 8.7: Simulated and measured pitch angle compared with pitch angle calculated from measured spring travel.

When turning the front wheels, the lateral force developed by the front tyres will contribute to a component acting in the longitudinal direction of the vehicle as a braking force, and thereby generating pitch by transferring load from the rear wheels to the front. Calculations for how much pitch that can be attributed to this is presented in Equation 8.3 – 8.6.

For the steady state achieved in the step steer experiment the front wheel steer angles are $\theta_1 = 8.5^\circ$ and $\theta_2 = 7.2^\circ$, and the lateral tyre forces $F_{y,1} = 3155$ N and $F_{y,2} = 1930$ N. This would contribute to a front downwards jacking of 2.2 mm and a rear upwards jacking of 1.8 mm, equivalent to a pitch angle of 0.08 degrees, which is about half of the total pitch experienced.

$$F_b = F_{y,1} \sin \theta_1 + F_{y,2} \sin \theta_2 \quad (8.3)$$

$$\Delta F_{z,f} + \Delta F_{z,r} = 0 \quad (8.4)$$

$$F_b \, cgh - \Delta F_{z,f} \frac{l}{2} + \Delta F_{z,r} \frac{l}{2} = 0 \quad (8.5)$$

$$\Delta z_f = \frac{\Delta F_{z,f}}{k_f}, \quad \Delta z_r = \frac{\Delta F_{z,r}}{k_r} \quad (8.6)$$

In Figure 8.8 the simulated model show a downward jacking of 6 mm for the front suspension, and an slight upward rear jacking of 1.5 mm. The measured data shows

near zero pitch and an upward jacking of the front (15 mm) as well as for the rear (10 mm). The difference between simulated and measured jacking is quite significant, especially considering the front jacking where simulated and measured data show completely different behaviour. This can be derived to instant centre location and/or lateral tyre forces, as these determine jacking. Instant centre locations is determined by the linkage modelling and the hub elasticity, and if these is not able to capture a correct behaviour, it might very well be seen in jacking behaviour. The lateral tyre forces are determined by slip angle and normal load, where the later being dependant on such a huge amount of different parameters, making it impossible to derive a likely source of error for the jacking from this.

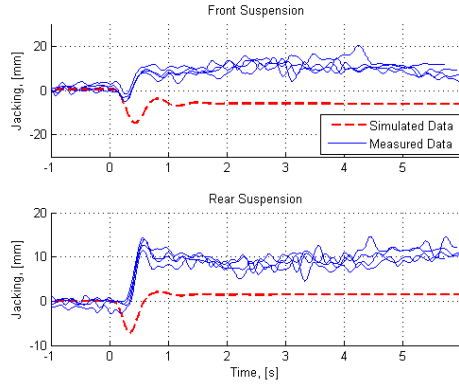


Figure 8.8: *Jacking of front and rear suspension, for the step steer experiment, calculated based on spring travel and wheel to spring motion ratio.*

Calculations for the front jacking, $z_{jacking,front}$, is derived by Equation 8.7 – 8.9. Indices 1 and 2 refers to the front left and right wheels, α is the angle between the ground level and the line constituted by the tyre contact patch and the instant centre, k_{front} is the vertical stiffness being the wheel rate for both wheels. Table 8.1 presents results from these calculations for the lateral tyre forces and instant centre locations at the steady state achieved in the step steer experiment in section 8.1.3, corresponding to both the geometric and the compliant suspension.

Looking at the calculated jacking, both the geometric and the compliant suspension gives similar results for the front suspension, a downward jacking not too far from the simulation results. The rear jacking differs a bit more between the two suspensions, and if taking the load transfer generated by the steered front wheels into the account, the compliant suspensions end up with a jacking very close to the simulated result, while the geometric suspension jacking is about 6 mm above the simulated result.

$$F_{jacking,1} = F_{y,1} \tan \alpha_1, \quad F_{jacking,2} = F_{y,2} \tan \alpha_2 \quad (8.7)$$

$$F_{jacking,front} = F_{jacking,1} + F_{jacking,2} \quad (8.8)$$

$$z_{jacking,front} = \frac{F_{jacking,front}}{k_{front}} \quad (8.9)$$

Table 8.1: *Calculated Jacking*

	Front Jacking, [mm]	Rear Jacking, [mm]
Geometric Suspension	-5.4	5.1
Compliant Suspension	-4.2	-0.1

8.1.6 Roll

Roll angle is determined by the lateral acceleration, sprung mass and its location, roll stiffness and roll centre height. The lateral acceleration differs by +/- 5–10 % between the simulations and the measurement data. Vehicle mass is the same as the measured with sprung component mass lumped at the wheels, centre of gravity location for the sprung mass is recalculated so that the combined vehicle centre of gravity is still found at the measured. Roll stiffness is validated both for suspension linkages individually in suspension rigs and coupled with tyre vertical stiffness in the full vehicle model. The roll angle measurement compared to the simulation data still differs significantly, 20-40 %.

The calculation below is for a simplified two-dimensional rear-view case, with front and rear suspensions combined at the centre of gravity.

Table 8.2: *Roll data*

$K_{roll,rear}$	776 Nm/deg
$K_{roll,front}$	1322 Nm/deg
$K_{roll,tot}$	2098 Nm/deg
m_{sprung}	1539 kg
a	0.6g

$$F = m a \quad (8.10)$$

$$\frac{F L_{cgh,Rc}}{K_{tot}} = \phi \quad (8.11)$$

$$\frac{\phi K_{tot}}{F} = L_{cgh,Rc} \quad (8.12)$$

Entering the simulated and measured roll values from Figure 8.4 shows that the roll moment lever arm (distance between centre of gravity and roll centre), $L_{cgh,Rc}$, is 466 mm for the measured values (2 degree roll) and 579 mm for the simulation model (2.5 degree roll), suggesting the model should have an averaged roll centre positioned 113 mm higher for the current state.

Figure 8.9 and Figure 8.10 show the roll centre movements along with the roll centre position at a roll angle of 2.5 degrees. Here is shown that the geometric front and rear roll centre together gives a chassis roll centre about 40 mm below ground, which differs by only 6 mm from the above calculated chassis roll centre (being 46 mm below ground). The compliant front and rear suspension gives a chassis roll centre of roughly 90 mm above ground, which is more comparable to the roll centre calculated from measurement data above, being 67 mm.

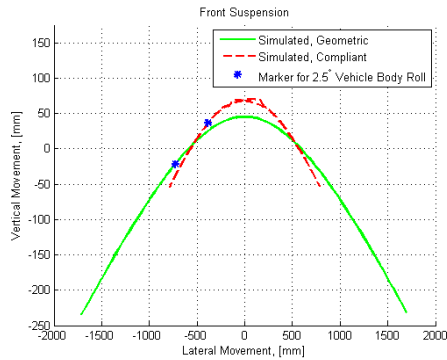


Figure 8.9: Front roll centre movement, with marker for 2.5 degree roll angle.

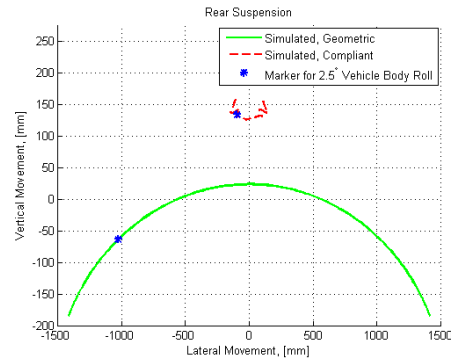


Figure 8.10: Rear roll centre movement, with marker for 2.5 degree roll angle.

Roll calculations above indicate that the simulated model, tends to have a roll behaviour close to that expected of the geometric suspension. The jacking calculations do not show a significant difference between geometric and compliant suspension, though, the compliant suspension calculations gives a result slightly closer to the simulations. This suggests that the hub compliance does not affect the roll centres, while it may have a very small effect on jacking. To investigate this theory an experiment similar to the step steer is performed, where the vehicle path radius is controlled in order to achieve the same lateral acceleration. The toe and steer elasticities will therefore not affect the result, allowing a legible comparison. In Figure 8.11 and Figure 8.12 roll angle and jacking for the two runs coincide for the full simulation time, verifying that the hub compliance have no effect on the instant centres and roll centres.

A reasonable result as the joints do not take torque loads and the suspension geometry remains unchanged with the hub elasticity, only the angle of the hub mounting surface changes. The suspension arms therefore still are axially loaded and the projected load distribution in the YZ plane remains unchanged.

Relocation of Instant Centres

To investigate what effects relocated instant centres for the wheels would have on the vehicle, the suspension geometry was changed to vertically move the instant centres, and thereby also the roll centre. The rear suspension is such a complex system, difficult to modify in a way only affecting the instant centres without severely altering other characteristics, and therefore only the front suspension was modified.

Simply moving the front suspension inner linkage joints vertically will result in vertically changed instant centres. This could also be achieved by moving either the upper strut joint or the outer linkage joints, however, strut joint movement would need such large movements that it would affect other properties and rearranging the outer linkage joints would noticeable affect the steering geometry even for very small changes.

In Figure 8.13 the front suspension roll centre movement for two suspensions having inner joints located 20 mm above respectively below the original geometry is compared to the prior used suspension geometry. It can be seen that moving the joints upwards also moves the roll centre upwards, although the lateral movements are decreased to

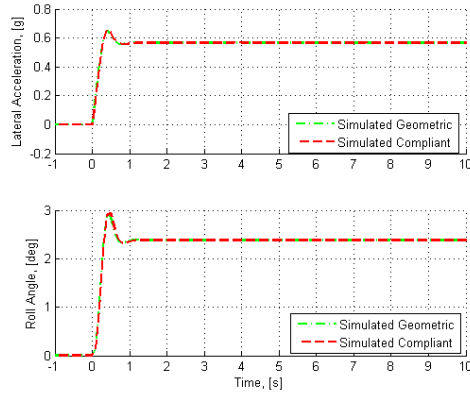


Figure 8.11: Constant turning-radius experiment comparing lateral acceleration and roll angle.

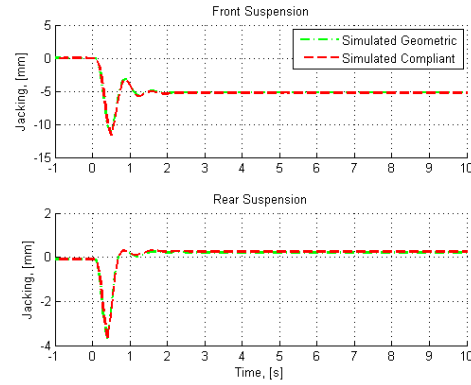


Figure 8.12: Constant turning-radius experiment comparing jacking.

approximately $1/4th$. Lowering the joints will for small roll angles also lowering the roll centre, but for an increasing roll angle the roll centre will behave different by laterally and vertically moving in the opposite direction from what the unmodified geometry originally did.

The modified suspension with the inner joints moved upward sees a front roll centre at 100 mm above the ground place at zero roll, for a roll angle of 2 degrees the roll centre moves down to 90 mm above the ground plane and 200 mm laterally. The linkage with the inner joints moved downward places the roll centre 30 mm below ground at zero roll, at 2 degrees roll the roll centre moves up to 70 mm above the ground plane and 1000 mm laterally.

Figure 8.14 presents the most general results for a step steer experiment using the modified suspension having its linkage joints positioned 20 mm upwards, and in Figure 8.15 the jacking effects is shown. The experiment is similar to the one presented in Figure 8.4, though it is performed as a constant radius experiment giving the same lateral accelerations for all runs, since modifying the suspension introduces small differences in the steering geometry.

The reduced roll angle and jacking for the raised roll centre suspension (linkage joints moved upwards) compared to the original suspension, agrees with the previous discussions for roll centre height. The lowered linkage joints suspension is also corresponding to this, result presented in Appendix C.4.3, with an increase in both roll and jacking effects, though, Figure 8.13 show that for a roll angle of two degrees the roll centre is actually higher than for the original suspension geometry.

Table 8.3: Calculated Jacking for Modified Suspension

	Front Jacking, [mm]
Raised Instant Centres	-2.9
Lowered Instant Centres	-10.2

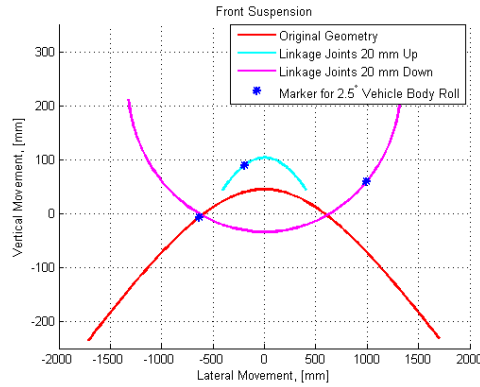


Figure 8.13: Front geometric suspension roll centre movement for original geometry and inner linkage joints moved upwards respectively downwards 20 mm.

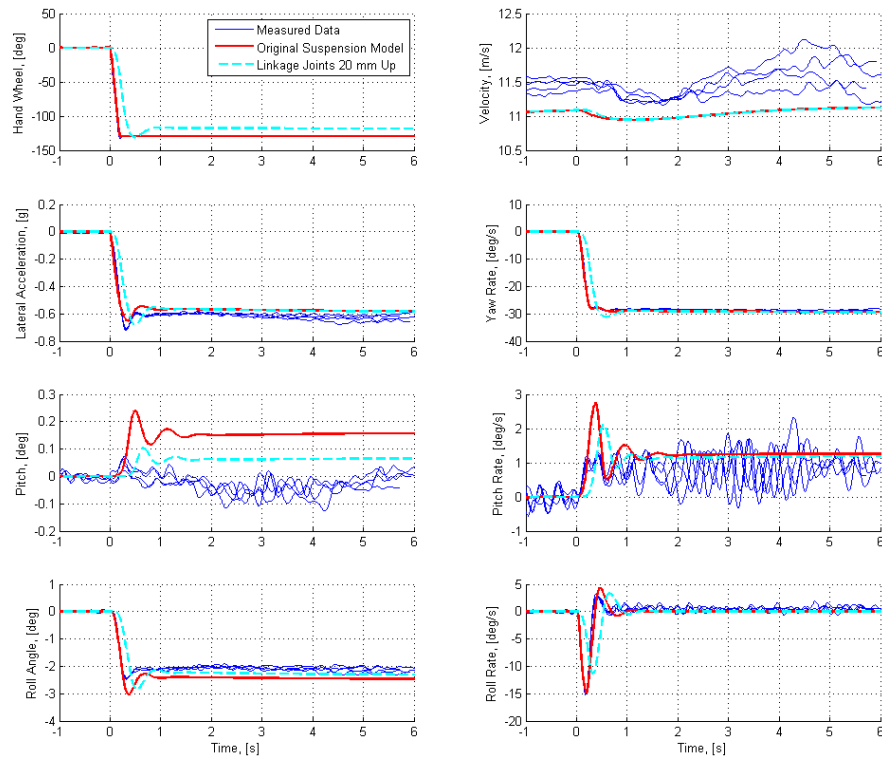


Figure 8.14: Step steer experiment comparing the vehicle model with modified suspension, where linkage joints been moved upwards, with original geometry suspension and measurement data.

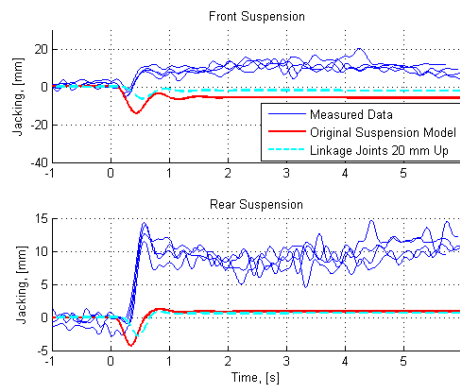


Figure 8.15: *Jacking for the step steer experiment comparing the vehicle model having a modified suspension, where linkage joints been moved upwards, with original geometry suspension and measurement data.*

Chapter 9

Conclusions

The model presented above with the modeling techniques used, proved to yield a fairly accurate model, however, there are still issues with the model formulation, these are presented and explained in chapter 8.

Thorough investigations have been made in order to determine how the lumped hub elasticity affects the model behaviour, as shown in 6.1.1 the formulation is limited by a parameter set to describe both compliance in roll and in bounce leading to compromises.

Results of the full vehicle simulations also have shown a consistently high roll angle of the simulation model when compared to measurements, this has been sourced to an erroneous formulation of the suspension geometry, specifically that of the roll centre. See section 8.1.6.

9.1 Restrictions and Limitations

The model development is limited by in data, the measurements gathered lack information on how they were performed and quasi-static measurements lead to poor information on dynamic behaviour of the elasticity.

Parameters for suspension geometry coordinates have been impossible to validate, measurements including elasticities have been available, these measurements are limited to wheel deflections, more detailed information on deformations as mentioned in [25] has not been available.

The tyre model used in [12] as presented in [5, 21] contain inconsistencies in the formulations between the two, plotting tyre model data using both formulations has allowed determination of the correct formulation. Information on how the formulations of the tyre models have been derived is also very vague, leading to determination of the correct formulation by following the mathematical derivation impossible. An analysis of the tyre model is performed in [14], however with the primary purpose of simplifying the model for computational performance it has been to little aid. The validation presented in [5, 12] should be sufficient.

The parameter data presented in [22] is gathered for a real time simulation environment, in the additional kinematics and compliance measurement report data was only gathered at the wheel and limited to lateral load and aligning moment, steering compliance measurement data is vague due to hysteresis effects, no information regarding the rise and fall times is presented in the report [19].

The roll data presented in the kinematics and compliance report shows that the vehicle roll motion has not been around the centre of the vehicle, this meaning that for parameter determination for elastic properties is based on mean values between left and right roll motions [19].

As the original data set was gathered for real time simulations, the elasticity measurements were only performed at the wheel as this modeling approach had been decided beforehand. Despite dismounting all the suspension links for mass and inertia determination, no individual elasticity measurements were performed. This is highly unfortunate as a comparison between a lumped hub elasticity and individual elasticity modeling would be very interesting since the lumped hub elasticity is limited especially for the five link rear suspension.

9.2 Final Discussion

Within this thesis a multibody simulation model is formulated and validated based on measurements presented in [22], the resulting model performs close to that presented in [20]. In the development of the simulation model several issues with a limited measurement data set have been encountered and solutions to them presented.

9.2.1 Elasticity Modelling

Elasticity modeling has been one of the main concerns in this thesis, in [22] the lumped elasticity formulation presented uses only lateral loads and aligning moment. In the multibody formulation used here this proved insufficient in describing the wheel motion throughout the suspension wheel travel, see C.3.1.

The formulation developed in order to circumvent issues with the a non-invertible stiffness matrix proved to work well. However, as the effects of a lumped hub elasticity have not been thoroughly investigated and no previous research in the area has been found. In this thesis it has been shown that the lumped elasticity formulation has no effect on instant centres, thus making the hub instant rotation method used in section 5.3.2 for roll centre calculations invalid for models with lumped hub elasticities.

Applying lumped elasticities is questionable for suspensions such as the rear suspension in the vehicle studied, with five separate links mounted with bushings on each end as the camber and toe behaviour of such five link suspensions is tuned by adjusting elasticities. As it is inadvisable to implement higher order polynomials to adapt elasticity response for short measurement spans, it is not always possible to achieve exact camber and toe behaviour. See results in section 6.2, C.3.3.

Another issue with a lumped elasticity formulation is that of the adjustment to anti-roll bar loads, as the camber and toe curves differentiate when the vehicle is in bounce or roll states for the same amount of wheel travel or load as seen in section 6.1.2, especially Figure 6.7 and Figure 6.9.

9.2.2 Kinematics

The kinematics modelling has been fairly straightforward, the resulting suspension kinematics are quite far from the measured suspension behaviour in many cases, see section C.3.1.

Results show that roll centres are not correctly modelled as stated in sections 8.1.6, 5.3.2. However as stated by Heydinger et al. "Adjusting the parameters of the model to

fit experimental results is just a curve-fitting effort that results in erroneous or invalid simulation software” [12].

Within this thesis these results have been based only on the resulting simulation data and the vehicle driving data provided, corrections to the suspension geometry points as suggested in [25] have not been made for anything but investigations of what effects a small change has.

9.2.3 Final Conclusion

9.3 Future Work

Future work stemming from this thesis could be divided into two sections. The first includes extensions to the model presented here, using it as a validated model of a typical road vehicle today for studies on the effects of regulated braking for stability control and regulated driving of separate wheels within a hybrid drive system. The second is deeper studies of the model formulation issues presented within this thesis. Further studies are suggested on the effects of lumped hub compliances, how the anti-roll bar load contribution and the parametrisation of the elasticity could be solved in a generalised way to accurately account for both cases, how the jacking effect is affected by the elasticity, if there is a possibility of including the changes in jacking with a lumped elasticity.

Chapter 10

Acknowledgements

Thanks to Per Lidström for his interest and support, Johan Andreasson for support and thoughts in his busy schedule, Magnus Gäfvert for help with everything computer related, Mathias Persson for discussing any thoughts and ideas on mechanics or numerics and everyone at Modelon for good company and making us coffee.

Thanks to Dr. Mohammed Kamel Salaani for writing inspiring articles, providing us with measurement data and answering our questions regarding their work.

Also thanks to Krister Olsson and everyone else involved with Formula Student at LTH and Martin Tunér for giving us our first introduction to vehicle dynamics.

Paula Persson deserves recognition for her patience in proof-reading and punctuation in endless sentences.

References

- [1] Massasonic m-5000/220 smart ultrasonic sensor, datasheet, 2005. [http://www.massa.com/datasheets/M-5000-220 20datasheet 2011-12-05.pdf](http://www.massa.com/datasheets/M-5000-220%20datasheet%202011-12-05.pdf).
- [2] An eigenvector approach to roll centre analysis. *SAE Technical paper 2007-01-0859*, 2007.
- [3] D. AB. Dynamic modeling laboratory. www.dynasim.se.
- [4] M. AB. Vehicle dynamics library - modeling and simulation of road vehicle dynamics. www.modelon.se.
- [5] R. W. Allen, T. J. Rosenthal, and J. P. Chrstos. A vehicle dynamics tire model for both pavement and off-road conditions. *SAE International*, 1997.
- [6] M. Association. Modelica - a unified object-oriented language for physical systems modeling language, 2007. <http://www.modelica.org/documents/ModelicaSpec30.pdf>.
- [7] M. Blundell and D. Harty. *The Multibody Systems Approach to Vehicle Dynamics*. 2000.
- [8] S. Furic. Hybrid acausal modeling using modelica. *LMS Slide*, 2007. [http://www.afsec-cnrs.org/wp-content/uploads/2007/07/Modelica Presentation.pdf](http://www.afsec-cnrs.org/wp-content/uploads/2007/07/Modelica%20Presentation.pdf).
- [9] W. R. Garrott, P. A. Grygier, J. P. Chrstos, G. J. Heydinger, K. Salaani, J. G. Howe, and D. A. Guenther. Methodology for validating the national advanced driving simulator's vehicle dynamics. *SAE International*, 1997.
- [10] M. Gäfvert, J. Svendenius, and J. Andreasson. Implementation and application of a semi empirical tire-model in multi-body simulation of vehicle handling. *AVEC 06*, 2006.
- [11] G. J. Heydinger, M. K. Salaani, and D. A. Guenther. Validation results from using nadsdyna vehicle dynamics simulation. *SAE International*, 1997.
- [12] G. J. Heydinger, C. Schwarz, M. K. Salaani, and P. A. Grygier. Model validation of the 2006 bmw 330i for the national advanced driving simulator. *SAE International*, 2007.
- [13] S. S. S. Inc. Continental tire model, bridgestone 225/40, bridgestone 255/35 r18.

- [14] Q. Liu, D. Solis, and W. Pan. Analysis of the sti tire model. *SAE International*, 2002.
- [15] H. E. Martin Otter. Modelica language, libraries, tools, workshop and eu-project realsim, 2000. <http://www.modelica.org/documents/ModelicaOverview14.pdf>.
- [16] W. F. Milliken and D. L. Milliken. *Race Car Vehicle Dynamics*. Society of Automotive Engineers, 1995.
- [17] W. C. Mitchell. Force-based roll centers and an enhanced kinematic roll center. *SAE International*, 2006.
- [18] H. B. Pacejka. *Tyre and Vehicle Dynamics*. Elsevier Butterworth-Heinemann, 2002.
- [19] S. E. A. Report. Vehicle inertia measurement facility, suspension kinematics and compliances, shock absorber, suspension component geometric and inertia, and tire test measurement results, 2006. Tests performed for the University of Iowa of 2006 BMW 330i.
- [20] M. K. Salaani. Analytical tire forces and moments model with validated data. *SAE International*, 2007.
- [21] M. K. Salaani and G. J. Heydinger. Powertrain and brake modeling of the 1994 ford taurus for the national advanced driving simulator. *SAE International*, pages 11–13, 1998.
- [22] M. K. Salaani, C. Schwarz, G. J. Heydinger, and P. A. Grygier. Parameter determination and vehicle dynamics modeling for the national advanced driving simulator of the 2006 bmw 330i. *SAE International*, 2007.
- [23] J. Svendenius. *Tire Modeling and Friction Estimation*. PhD thesis, Lund University, 2007.
- [24] J. Svendenius and B. Wittenmark. Brush tire models with increased flexibility. *Lund University, dept. of Automatic Control*, 2003.
- [25] P. van der Jagt. *The Road to Virtual Vehicle Prototyping; new CAE-models for accelerated vehicle dynamics development*. Technische Universiteit Eindhoven, 2000.
- [26] E. Wennerström, S. Nordmark, and B. Thorvald. Fordonsdynamik. *Royal Institute of Technology, dept. of Vehicle Dynamics*, 2006.

Appendix A

Basic Vehicle Dynamics Terminology

The change of momentum of a body is proportional to the impulse impressed on the body, and happens along the straight line on which that impulse is impressed.

Sir Isaac Newton (1642 - 1727)

In order to understand vehicle dynamic behaviour it is important to describe the forces acting on the vehicle and how it responds to them.

The forces acting on the vehicle are mainly developed in the contact patch between tyre and ground, some aerodynamic forces such as drag are also present and more thoroughly described below. The forces developed in the tyre-ground contact patch are mainly dependent on the normal load and coefficient of friction in the contact interface.

A.1 Coordinate Systems

In order to describe these motions one must have a clear definition of the motions and to what they are relative. Depending on what is studied a number of coordinate systems describing relative motions are used, a system following the sprung mass motions in longitudinal (x), lateral (y) and vertical (z) as well as rotations, roll (about x), pitch (about y) and yaw (about z).

Different directions of the axes are defined in Society of Automotive Engineers (SAE) j670e and International Organization for Standardisation (ISO) 8855. In the SAE definition x is positive forward, y positive to the right and z positive down. In the ISO definition x is positive forward, y positive to the left and z positive upwards. As the simulation software used in this thesis by default uses the ISO definition, also referred to as Frontward Leftward Upward (FLU), this will be used throughout the thesis. Subsystems and components are also described as far as it is possible with the FLU definition.

A.2 Motions and Angles

Since the forces in the tyre-ground contact patch are mainly dependent on the normal load it is important to understand how this normal load varies on each wheel. To

describe the variation in the normal loads the vehicle is viewed as a rigid body with a mass resting on springs connected to the wheels. The rigid body is commonly referred to as sprung mass and the mass of the wheels and their subsystems referred to as un-sprung mass.

A.2.1 Body

In a simplified case, a force developed by an applied torque at a wheel acts on the contact patch in the vehicle side view. The resultant moment about the centre of gravity (CG) compresses one spring and extends the other, this effectively changes the normal load distribution between the wheels and in a steady state case results in a rotational displacement of the rigid body. This rotation about the y-axis is referred to as pitch angle. The same principle can be applied to the front view, where a force acting in the contact patch in the lateral direction results in a rotation about the x-axis called roll angle.

When a steer angle is applied to the front wheels, the resulting rotation around the z-axis is referred to as yaw angle.

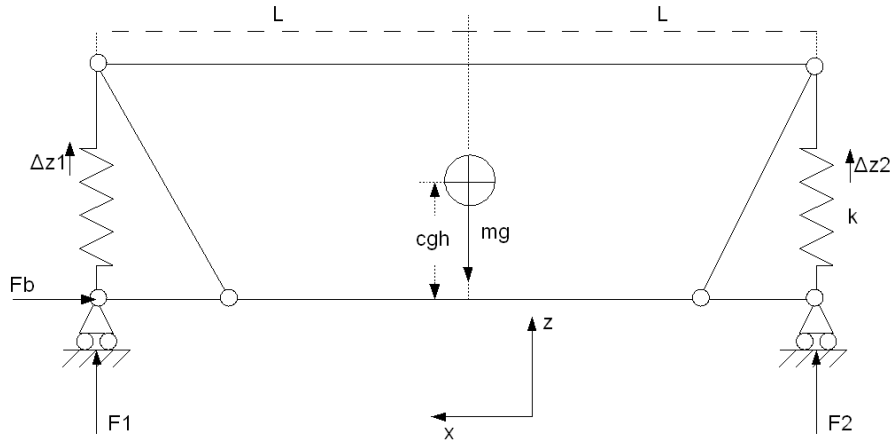


Figure A.1: *Simplified vehicle body in side view*

$$0 = F_1 + F_2 - mg \quad (\text{A.1})$$

$$0 = F_b CGH + F_2 l - F_1 l \quad (\text{A.2})$$

$$\Delta z_1 = \frac{F_1}{k} \quad (\text{A.3})$$

$$\Delta z_2 = \frac{F_2}{k} \quad (\text{A.4})$$

$$F_2 = \frac{mgl - F_b CGH}{2l} \quad (\text{A.5})$$

$$F_1 = mg - \left(\frac{mgl - F_b CGH}{2l} \right) \quad (\text{A.6})$$

$$F_1 = \frac{mgl + F_b CGH}{2l}$$

A.2.2 Wheel

In order to accurately determine the forces developed at the contact patch the force, position and rotations of the wheel are required. To describe the behaviour of the wheel one must define these motions and angles, referring to the FLU coordinate system translational motion along the z-axis is referred to as wheel travel or bounce for positive and rebound for negative translation.

Depending on design of the suspension, translation does occur during wheel travel in x and y directions, these motions are generally small but movement in y drags the tyre across the surface thus generating contact forces, this motion is referred to as scrubbing

Camber Angle

The angle which describes the angular offset for the wheel around the x-axis is known as the camber angle γ , this is positive for inclinations where the top of the wheel is pointing outwards from the car. The camber angle is often used to compensate for the tyre wall deflection during high lateral accelerations to keep the tyre contact patch flat against the ground.

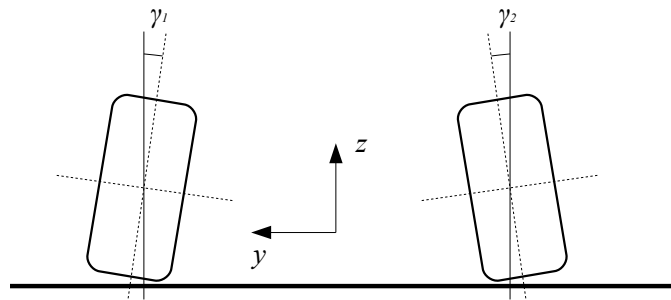


Figure A.2: Camber angle

Toe Angles

The offset angle around the z-axis is called toe angle, most often described with the terms *toe in*, front end of the wheel pointing in towards the centre line of the car, and *toe out*, front end pointing outwards, these are also referred to as positive respective negative toe. Generally toe in configurations increase vehicle stability in a straight line while toe out gives a quicker turn in response.

Steering Angle

Steer angle and toe angle describe the same rotation, steer angle defines the wheel rotation achieved by steering wheel inputs and is coupled between the left and right steerable wheels. Steer angles are positive for positive rotations about the z-axis.

Due to the track of the vehicle, the inside and outside wheel do not follow the same radius turn, this is sometimes compensated within the steering system geometry in order to make the inside wheel rotate more than the outside for a given steering angle input, this is referred to as ackermann steering, with the inside wheel rotating more than the outside positive ackermann steering exists, both wheels turning equally is referred to

as parallel steer and inside wheel turning less than the outside is negative ackermann steering.

Steering Axis (Kingpin & Caster)

The steering axis is described by the caster angle and the kingpin inclination angle, where caster angle is defined by the steering axis inclination seen in side view, caster is positive with the top mount rearward of the lower mount. Kingpin inclination is the steering axis incline seen in front view, positive for a top inward incline.

Both the caster angle and the kingpin inclination have a large influence on camber change when steering. If considering the left front wheel, a positive caster angle will contribute to a negative camber change for negative steer angles (right hand turn), while a positive kingpin inclination will contribute to a positive and vice versa yields for negative caster and kingpin angles.

The caster angle affects the straight line stability of the vehicle by introducing a self-centring effect, it also influences the required steering torque and diagonal load transfer as the vehicle is lifted onto the tyre sidewall with steering angle.

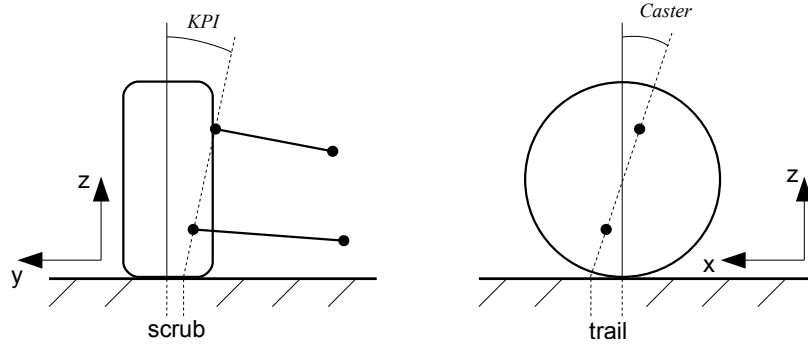


Figure A.3: Rear and side view of a wheel, showing KPI and caster angle

Scrub Radius

Scrub radius is the projected distance between the wheel centre axis and the steering axis on the XY plane in the ground plane, see figure A.3. This forms a lever arm for the tyre contact patch forces, creating a moment about the steering axis, which heavily affect the required steering torque especially for slow speed corners.

Trail

Trail is the projected distance between the wheel centre axis and the steering axis on the XZ plane in the ground plane, see figure A.3, pictured here is the mechanical trail component. In reality the effective tyre contact patch moves with varying slip affecting the trail, the tyre component is referred to as pneumatic trail.

A.3 Springs and Dampers

Road vehicles commonly use coil springs combined with a torsion beam coupled between the left and right side to provide additional stiffness in roll. The main purpose is to allow a vertical motion of the wheel relative to the vehicle body, thus letting the wheel follow the irregularities of the road surface with the body proceeding in its previous path without disturbance, while limiting wheel travel to reasonable amounts. From a handling perspective this translates into maintaining the wheel normal load to avoid sudden loss of contact forces, the configuration also allows sprung mass motion which is aimed at preventing sudden and large load transfers between the wheels. Large load transfers generally reduce the available contact forces as tyres do not have a linear relation between normal load and lateral/longitudinal force. The dampers are applied to reduce oscillations and limit the rate of spring compression.

Quite often different characteristics are desired for wheel bounce and body roll cases, a soft spring is used for comfort reasons when driving on rough surface roads, but this spring gives a low roll stiffness leading to large roll angles at lateral accelerations which leads to unfavourable wheel angles as well as discomfort for passengers. To cope with this problem a spring, often a torsion bar connecting a wheel pair so that it is subject to rotation when the left and right wheels travel relative to each other, this spring is called an anti roll bar or sway bar. For a vehicle driving through a corner the anti-roll bar transfers load from the inner wheel onto the outer, resulting in less roll angle.

As the anti-roll bar couples the left and right wheels, it also results in an increased stiffness for single wheel bump, when for example driving over a road irregularity with a single wheel.

A.4 Instant Centre

In any independent suspension, one linkage can be simplified to rotating about one point in space at a given position, this is determined by extending the axes through each suspension joint to find their intersection, see Figure A.4, the position of this intersection will change over suspension travel thus the term instant. The distance and position of the instant centre can be used to describe the rate of rotation of the wheel in camber and toe as well as calculation of anti geometries and roll centres as described in A.7 below, in order to simplify the description of these effects the three dimensional instant centre can be described by two two-dimensional projections, one in side view and one in front view. [16]

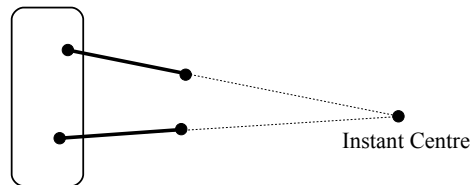


Figure A.4: *Instant centre definition, wheel seen in front-view.*

A.5 Roll Centre

With the instant centres for both the left and right suspension in front view determined a line between the tyre contact patch and respective instant centre can be determined to describe the arm the contact patch pivots about, the intersection of these pivot arms for the left and right wheel is the effective instant point about which the chassis rotates at that instant, see Figure A.5. This is useful for analysis of chassis motions when subject to lateral loads, care must be used though as the instant centres change with suspension deflection effectively changing the roll centre as well. [16, 17]

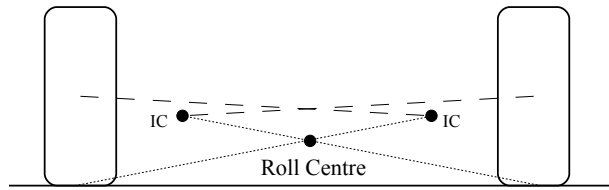


Figure A.5: *Roll centre definition, wheel pair seen in front-view.*

A.6 Jacking

As the linkage can be seen as a rigid bar pivoting about the instant centre a vertical and lateral force applied at the contact patch will effectively apply a force acting along the instant centre axis. The vertical component of this force, reacted through the suspension linkage not the springs, is commonly referred to as jacking, see Figure A.6. [16]

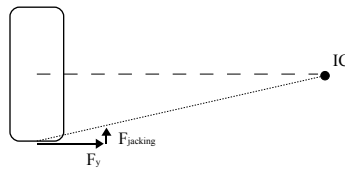


Figure A.6: *Jacking definition, wheel seen in front-view.*

A.7 Anti Geometries

Side view instant centres (see A.4) can be placed so that the suspension arms create a connection between sprung and unsprung mass for the longitudinal load transfer. This will affect what proportion of the load transfer is carried by the spring and how much is carried by the suspension linkage, without changing the load transfer seen by the

wheel, affecting body pitch. This is commonly referred to as anti geometries, anti-dive, anti-squat and anti-lift. [16]

This is used in order to cater for different characteristics in different driving situations, soft springs are used for rough surface comfort, while heavy braking manoeuvres would tilt the vehicle forward with a large amount of pitch angle, causing discomfort.

Another solution to this is using a progressive spring or a nonlinear wheel-to-spring motion ratio, giving a desired wheel constant for more moderate driving, while for heavy braking an increased spring constant acting on the wheel results in less wheel travel.

A.8 Understeer - Neutral Steer - Oversteer

In order to understand the concept of understeer and oversteer let us first define a simplified neutral steer vehicle, a vehicle with the CG at its center and equal tyres at all corners with no load transfers present, when this vehicle is steered into a steady state corner the rotation of the vehicle gives a rear slip angle equal to that of the front, the reactive centrifugal force acting at the CG is countered by the equal forces on front and rear tyres acting at equal distances from the CG.

Consider the same vehicle with the CG moved forward to 1/3 of the wheelbase rearward of the front axle, resulting in the front wheels carrying twice the load of the rear. Tyres are adjusted so that the cornering slopes are identical for front and rear with the new load distribution, when this vehicle is presented with the same radius corner as in the previous example the front axle takes 2/3 of the cornering force and the rear 1/3, as the cornering stiffness of the tyres is identical in the front and rear the front slip angle must be twice that of the rear. Meaning that to maintain the same radius corner the understeer car requires a larger steering angle than the neutral steer car.

In the same way a simple example of an oversteer vehicle can be created by placing the CG 2/3 rearward of the front axle, adjusting the tyres so that the cornering slopes are identical will lead to a smaller steering angle required at the front wheels in order to maintain the same radius turn. [16]

A.9 Aerodynamic Effects

The most commonly studied aerodynamic effect is drag, i.e. the force acting upon the vehicle as it passes through the air at speed. This is however mainly of interest for studies of fuel economy and engine performance.

$$F_D = \frac{1}{2} \rho u^2 C_D A$$

In road vehicle dynamics handling studies the most interesting aerodynamic effects result in variations of the normal load, referred to as lift or downforce, depending on if normal load decreases or increases.

In stability studies the effects of large sidewinds can be investigated, especially for larger vehicles such as vans and SUVs.

These effects are relatively small for the driving situations studied in this thesis and are therefore neglected.

A.10 Tyres

All road vehicles today are equipped with tyre shod wheels, nearly all of the forces acting on a vehicle are transmitted through the tyres. All driver controls, steering, braking and accelerating affect parts of the vehicle to generate forces in the tyre-ground contact patch. The road surface in turn affects the vehicle through the same contact patch, for example bumps or roughness in the surface.

The purpose of the tyre is not only to generate forces, but also minimize the rolling resistance and isolate the vehicle from high frequency road disturbances.

In vehicle dynamics, tyres generate most of the forces acting on the vehicle, therefore a good estimation and understanding of these forces and how they are generated is vital to an accurate result.

A.10.1 Slip

The tyre forces developed in the tyre to road contact patch is generally considered to be generated by slip. This slip describes the differences in wheel velocity and road relative velocity and is often divided into two different types commonly referred to as lateral and longitudinal slip, or slip angle (α) and slip ratio (S). Both lateral and longitudinal slip is built up by deflection of the tyre sidewall and carcass and due to sliding of the tyre against the road surface.

Lateral Slip

The slip angle is the angle between the direction of which the tyre is pointing and the direction of which the tyre is heading. This is often described by dividing the tyre velocity (V) into two components, longitudinal and lateral velocity (v_x and v_y), resolved in the wheel coordinate system.

$$\alpha = \arctan \frac{v_y}{v_x} \quad (\text{A.7})$$

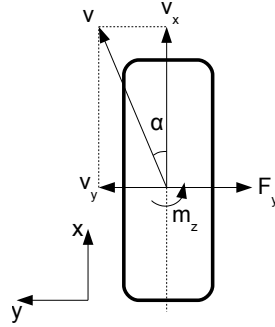


Figure A.7: Slip angle definition, tyre seen from above

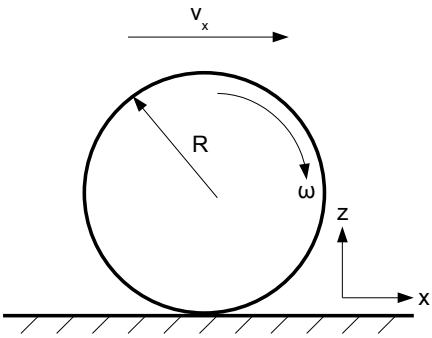
Longitudinal Slip

There are several different definitions for the slip ratio, all describing the difference between the velocity of the tyre carcass and the velocity of the road.

A common definition, and also the one used in the implemented tyre model, is the one described among others by Sakai in [24]. It is the difference between the wheel

hub longitudinal velocity relative to the ground and the wheel rotational velocity multiplied with the effective rolling radius, normalized with the wheel hub velocity. For this definition a slip ratio of $S = 1$ represents full braking slip, braking with locked wheels.

The effective rolling radius is determined by the distance the wheel will travel for a full revolution, this radius lies somewhere between the radius of the unloaded and loaded wheel.

$$S = \frac{v_x - R_e \omega}{v_x} \quad (\text{A.8})$$


The diagram illustrates a wheel in side view. A horizontal arrow above the wheel is labeled v_x , representing the hub longitudinal velocity. The wheel is a circle with radius R indicated by a line from the center to the top. A curved arrow on the right side of the wheel is labeled ω , representing the rotational velocity. The wheel is in contact with a horizontal ground surface, which is indicated by a line with diagonal hatching below it. A coordinate system is shown at the bottom right, with a vertical arrow labeled z pointing upwards and a horizontal arrow labeled x pointing to the right.

Figure A.8: Longitudinal slip definition, tyre seen in side view

Appendix B

Vehicle Measurements

This chapter is mainly a summary of the measurement procedures presented in [12, 19] as there are uncertainties regarding the procedures in these reports and a clarified summary is essential for repeatability of the results presented in this thesis.

B.1 Vehicle Inertia Measurement

The vehicle center of gravity height is measured in five separate tests, one to find the nominal zero angle of the platform and vehicle, two tests with the vehicle tilted forward and two with the vehicle tilted rearward. The results are then averaged.

The moment of inertia tests are repeated three times and the results are then averaged. [19]

B.2 Kinematics and Compliance

The suspension and steering were tested in nine different tests, in the bounce and roll tests tubular steel cross members were rigidly attached to the chassis, these were moved up and down in phase for the bounce test and out of phase for the roll test. In these tests the wheels were placed on floating wheel pads taking only vertical load so that no lateral, longitudinal forces or aligning moments would exist at the wheels. In all tests except the steering ratio test, the steering wheel was locked and all brakes applied.

In the lateral compliance tests a pneumatic cylinder was used to generate forces at the right side wheels. In the steering compliance test a custom device was used to apply an aligning moment on the right side wheels. [19]

B.3 Driving Manoeuvres

The vehicle field testing as performed for the University of Ohio by VRTC, this is a short summary of the information listed in [12] with some additional information from the measurement data and correspondence with Dr. Salaani.

The ultrasonic sensors were mounted near the CG along the length of the vehicle at track width, used in conjunction with the roll rate data from the inertial sensing system to determine roll angle.

B.3.1 Vehicle Motion Measurement

The rotational transitions about the vehicle coordinate axes is measured using a mutli-axis inertial sensing system mounted close to the vehicles centre of gravity. This device measures the rates of roll, yaw and pitch, and the corresponding angles is given by integration over the rates. An issue with this is that for a steady state corner, such as the step steer manoeuvre described in 8.1, if the sensor is slightly off zero, the tiny error is integrated for each increment and the result will drift from the steady state value.

Roll Measurement

To get a more accurate result for the roll angle an additional measurement method was used for this. Two ultrasonic sensors mounted on each side of the vehicle near the longitudinal center of gravity were used, and the output of these sensors were combined to find the roll angle. The ultrasonic sensors used can be found in [1]

Vehicle Speed

The longitudinal speed was measured with a non-contact speed sensor mounted near the lateral centre of at the rear of the vehicle. This was used for the maintenance of the constant speed.

Appendix C

Data plots

Here all simulation data plots of value are presented together with measurement data, divided in different sections.

C.1 Tyre Data

C.1.1 Front Tyres

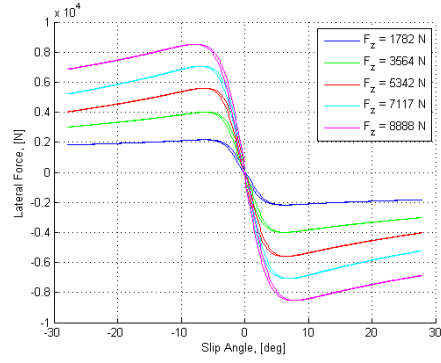


Figure C.1: Front tyre lateral force vs slip angle

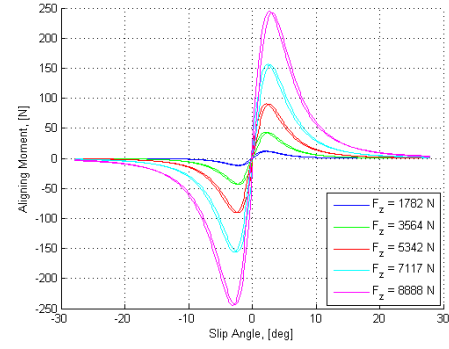


Figure C.2: Front tyre aligning moment vs slip angle

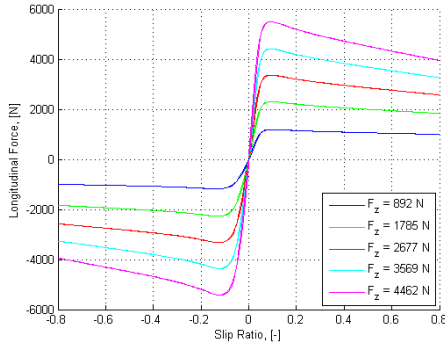


Figure C.3: Front tyre longitudinal force vs slip ratio

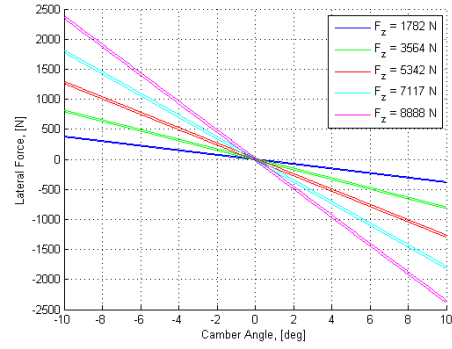


Figure C.4: Front tyre lateral force vs camber angle

C.1.2 Rear Tyres

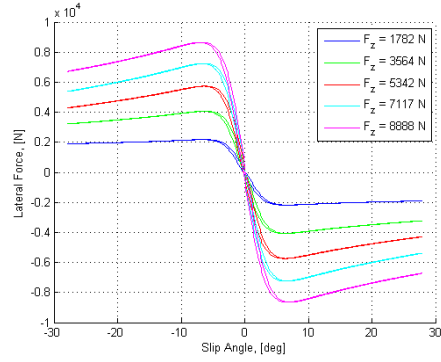


Figure C.5: Rear tyre lateral force vs slip angle

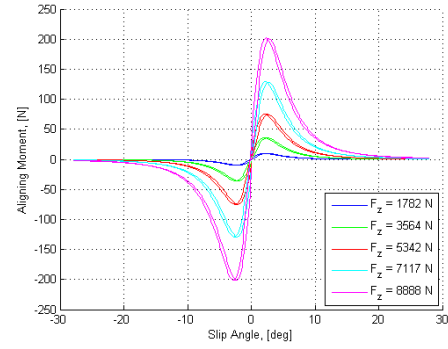


Figure C.6: Rear tyre aligning moment vs slip angle

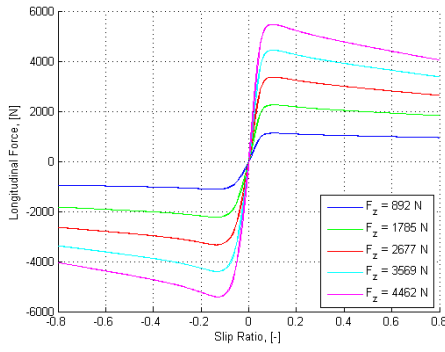


Figure C.7: Rear tyre longitudinal force vs slip ratio

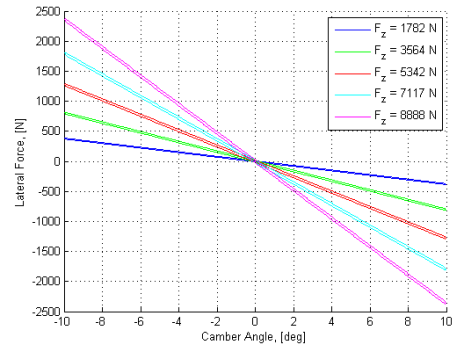


Figure C.8: Rear tyre lateral force vs camber angle

C.2 Spring and Damper Characteristics

Simulated bounce and roll stiffness, damping characteristics, plotted with measurement data.

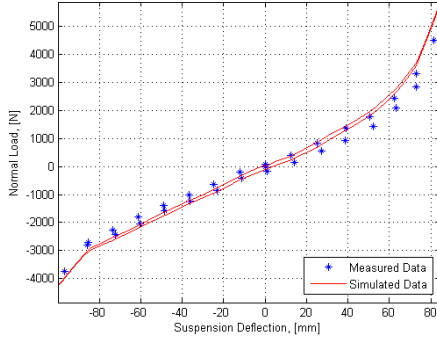


Figure C.9: *Front spring force*

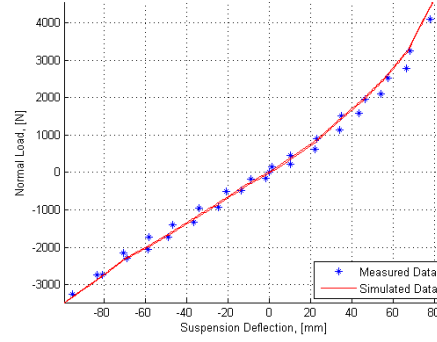


Figure C.10: *Rear spring force*

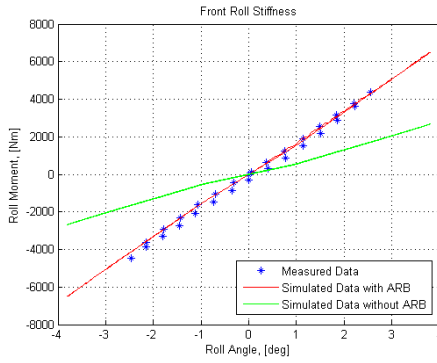


Figure C.11: *Front roll stiffness simulated with and without anti-roll bar, less tyre stiffness*

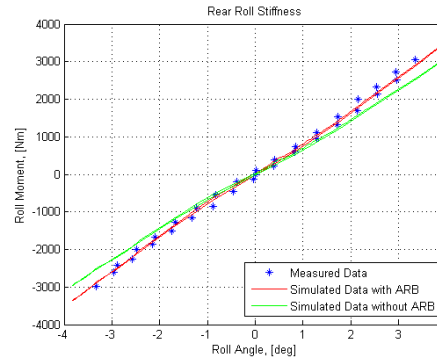


Figure C.12: *Rear roll stiffness simulated with and without anti-roll bar, less tyre stiffness*

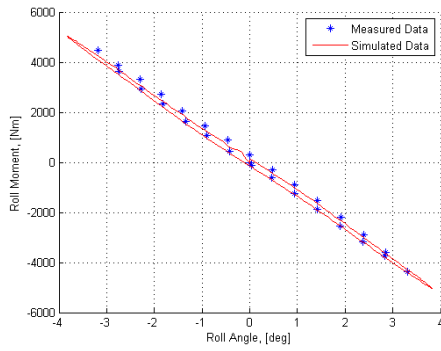


Figure C.13: Front roll stiffness simulated with anti-roll bar and tyre stiffness

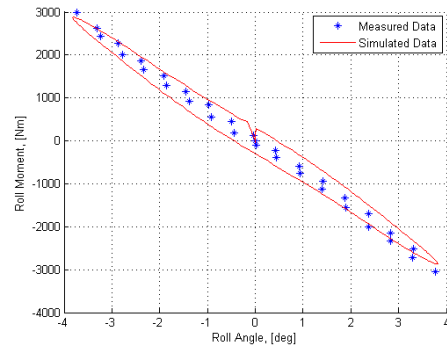


Figure C.14: Rear roll stiffness simulated with anti-roll bar and tyre stiffness

C.3 Suspension Characteristics

C.3.1 Geometric

Simulated suspension behaviour with purely geometric geometry, plotted with measurement data.

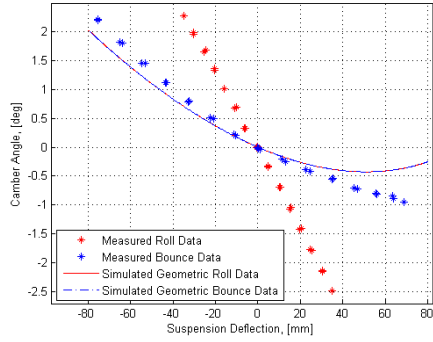


Figure C.15: Front left wheel camber angle vs. wheel travel, for the geometric suspension.

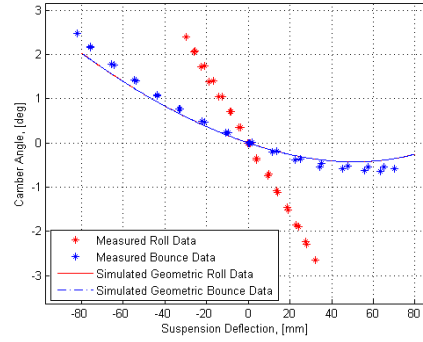


Figure C.16: Front right wheel camber angle vs. wheel travel, for the geometric suspension.

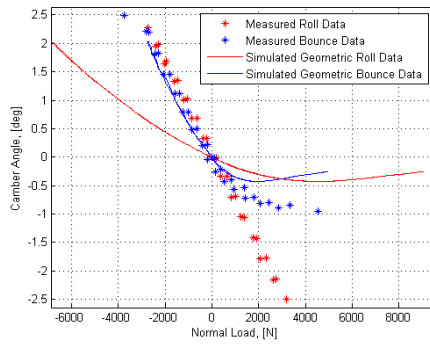


Figure C.17: Front left wheel camber angle vs. normal load, for the geometric suspension.

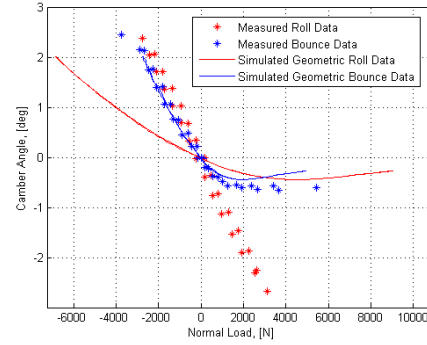


Figure C.18: Front right wheel camber angle vs. normal load, for the geometric suspension.

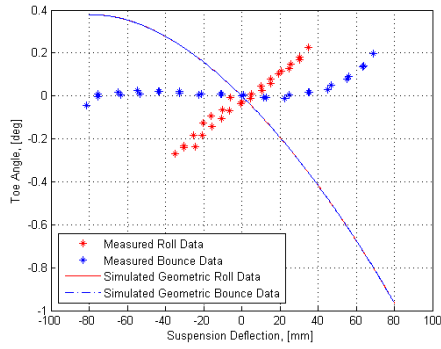


Figure C.19: Front left wheel toe angle vs. wheel travel, for the geometric suspension.

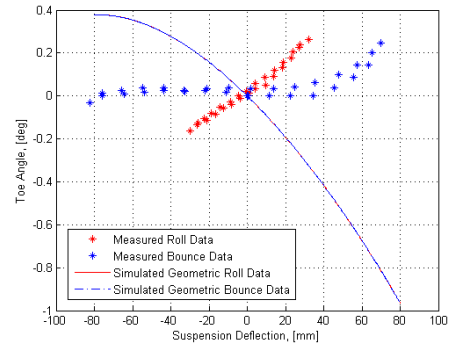


Figure C.20: Front right wheel toe angle vs. wheel travel, for the geometric suspension.

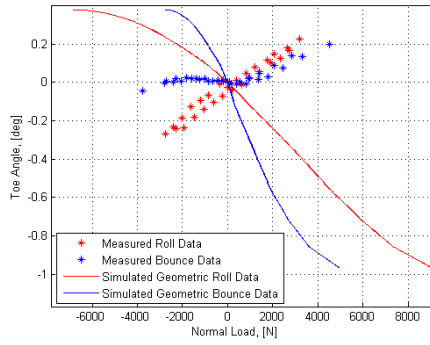


Figure C.21: Front left wheel toe angle vs. normal load, for the geometric suspension.

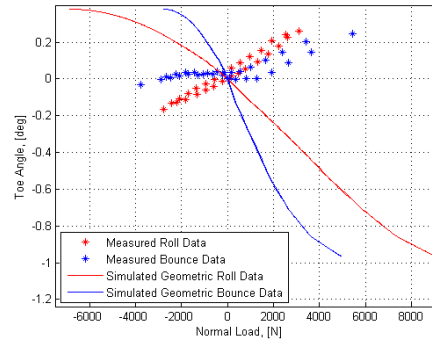


Figure C.22: Front right wheel toe angle vs. normal load, for the geometric suspension.

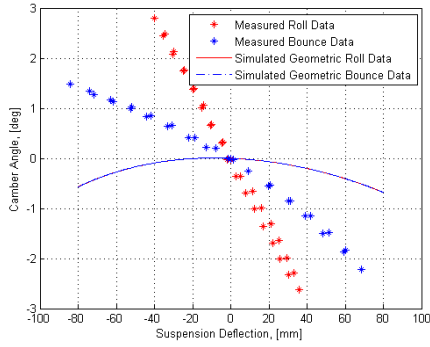


Figure C.23: Rear left wheel camber angle vs. wheel travel, for the geometric suspension.

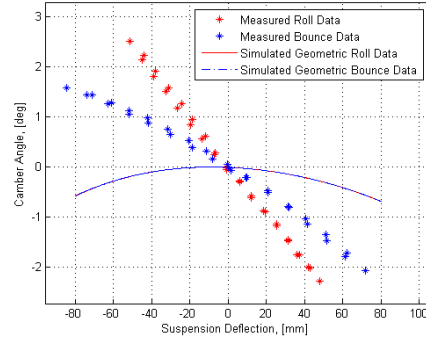


Figure C.24: Rear right wheel camber angle vs. wheel travel, for the geometric suspension.

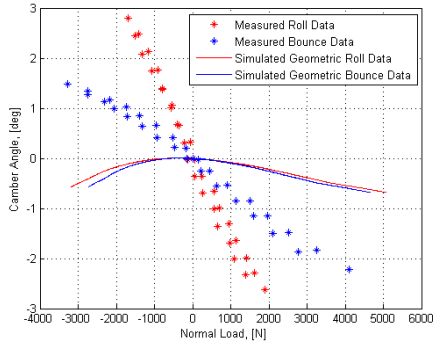


Figure C.25: Rear left wheel camber angle vs. normal load, for the geometric suspension.

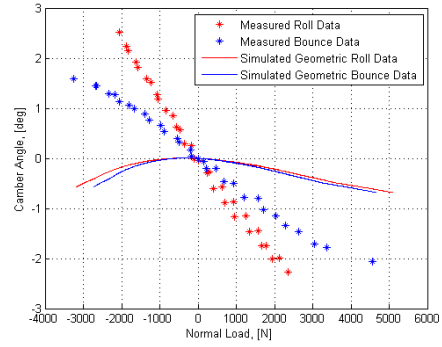


Figure C.26: Rear right wheel camber angle vs. normal load, for the geometric suspension.

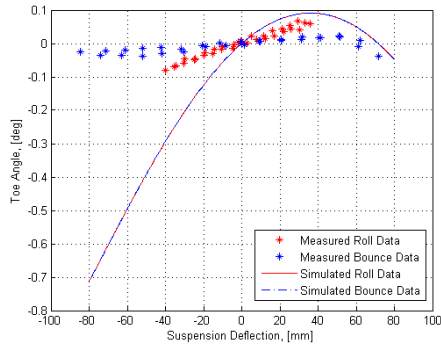


Figure C.27: Rear left wheel toe angle vs. wheel travel, for the geometric suspension.

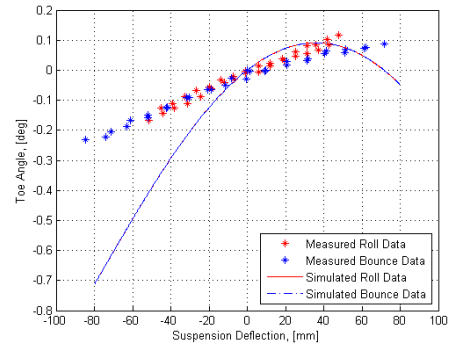


Figure C.28: Rear right wheel toe angle vs. wheel travel, for the geometric suspension.

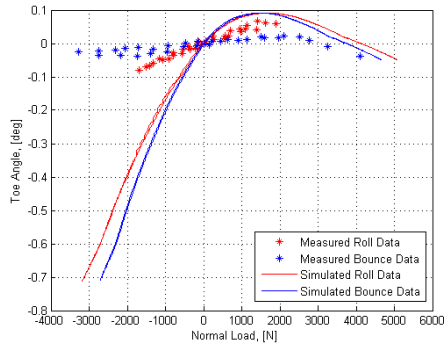


Figure C.29: Rear left wheel toe angle vs. normal load, for the geometric suspension.

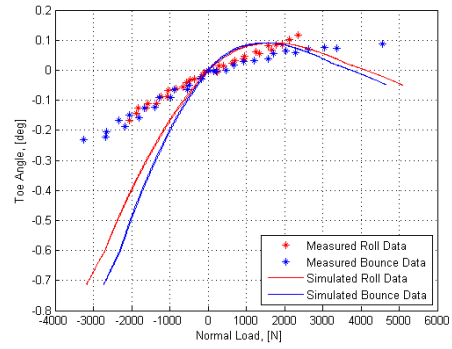


Figure C.30: Rear right wheel toe angle vs. normal load, for the geometric suspension.

C.3.2 Compliance

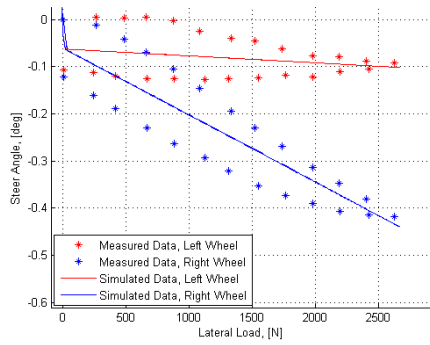


Figure C.31: Front lateral force steer compliance

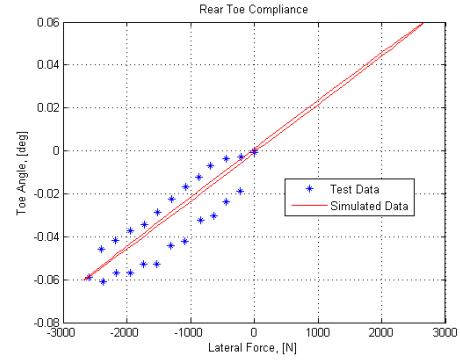


Figure C.32: Rear lateral force toe compliance

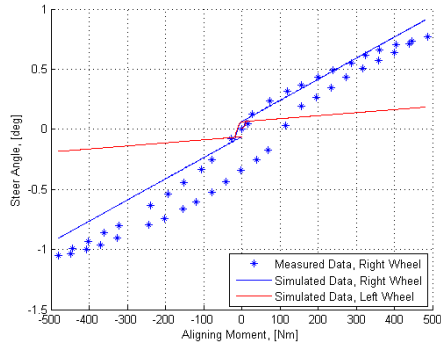


Figure C.33: Front aligning moment toe compliance

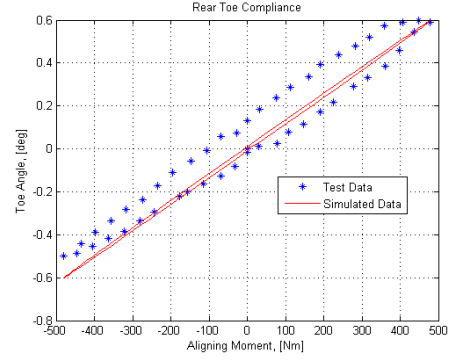


Figure C.34: Rear aligning moment toe compliance

C.3.3 Combined Compliant and Geometric Suspension Behaviour

Simulated suspension behaviour with hub elasticity, plotted with measurement data.

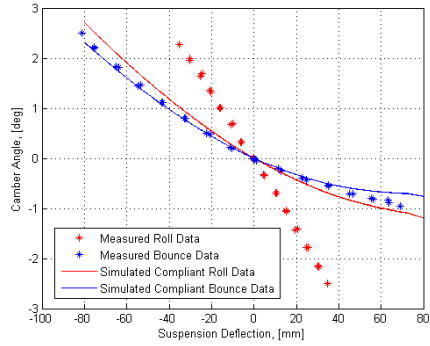


Figure C.35: Front left wheel camber angle vs. wheel travel, for the compliant suspension.

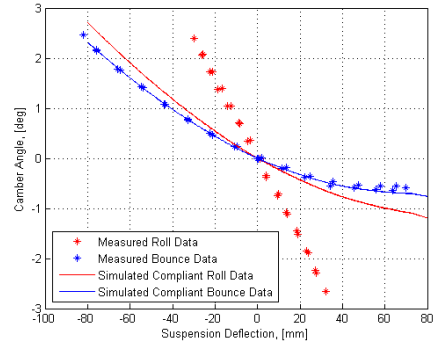


Figure C.36: Front right wheel camber angle vs. wheel travel, for the compliant suspension.

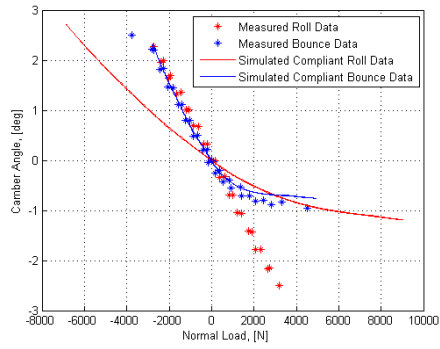


Figure C.37: Front left wheel camber angle vs. normal load, for the compliant suspension.

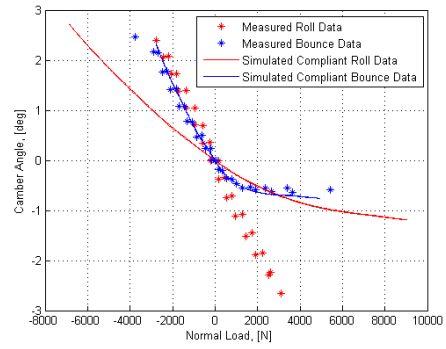


Figure C.38: Front right wheel camber angle vs. normal load, for the compliant suspension.

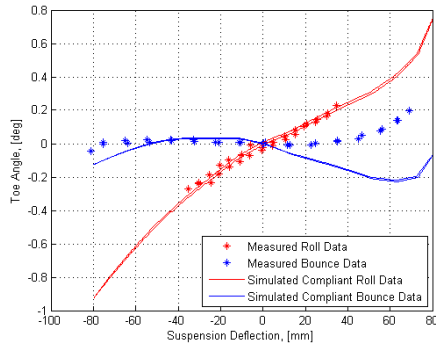


Figure C.39: Front left wheel toe angle vs. wheel travel, for the compliant suspension.

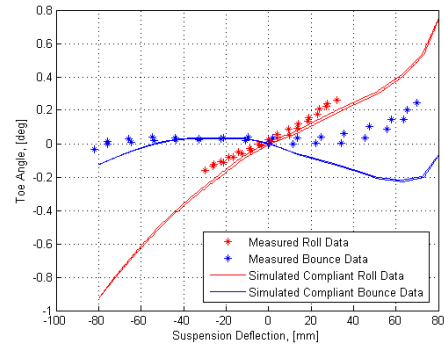


Figure C.40: Front right wheel toe angle vs. wheel travel, for the compliant suspension.

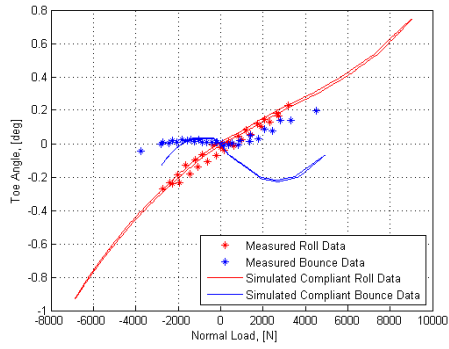


Figure C.41: Front left wheel toe angle vs. normal load, for the compliant suspension.

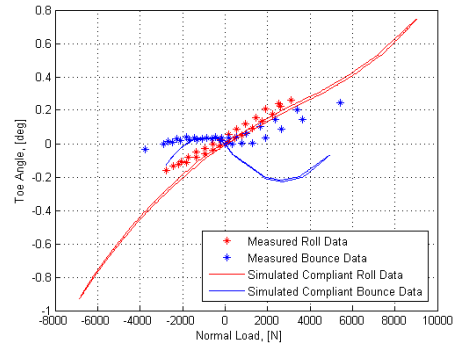


Figure C.42: Front right wheel toe angle vs. normal load, for the compliant suspension.

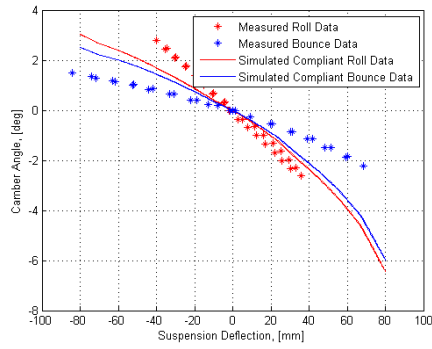


Figure C.43: Rear left wheel camber angle vs. wheel travel, for the compliant suspension.

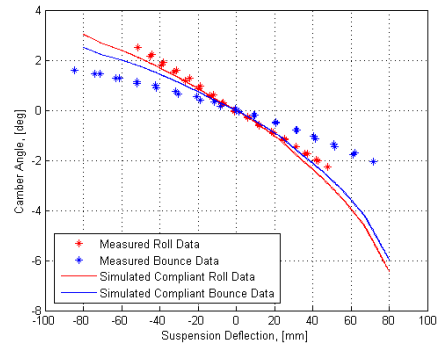


Figure C.44: Rear right wheel camber angle vs. wheel travel, for the compliant suspension.

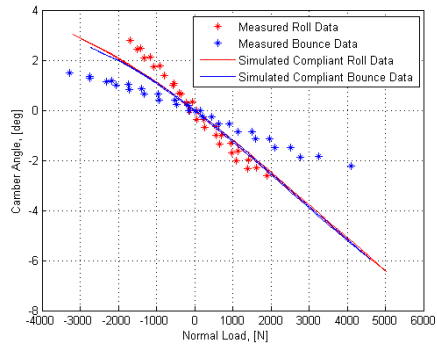


Figure C.45: Rear left wheel camber angle vs. normal load, for the compliant suspension.

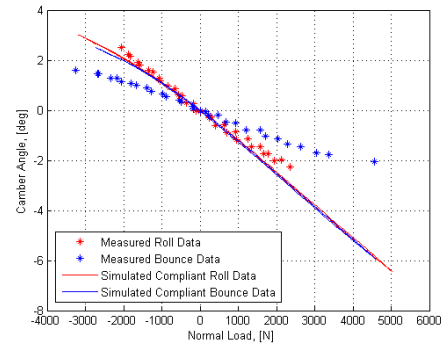


Figure C.46: Rear right wheel camber angle vs. normal load, for the compliant suspension.

C.4 Vehicle Behaviour

Here full vehicle experiments are presented.

C.4.1 Increasing Steer

Simulation model is compared with measurement data for an increasing steer experiment. A slowly increasing hand wheel input is turning the vehicle at a constant longitudinal speed. Six different runs are done, varying speed and turning direction.

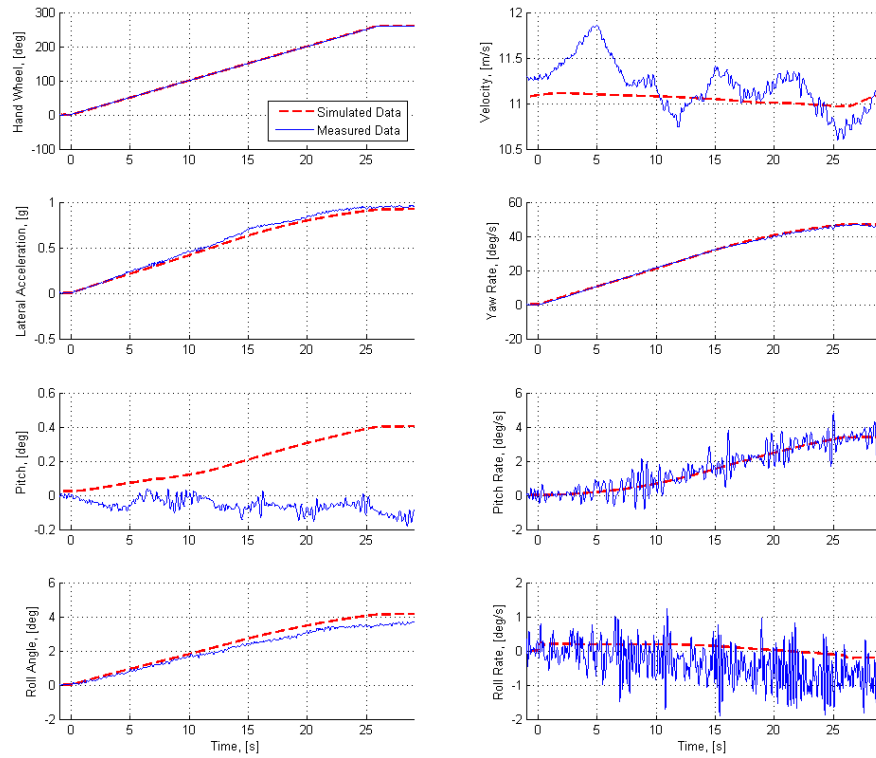


Figure C.47: Increasing steer experiment, left turn, 11 m/s.

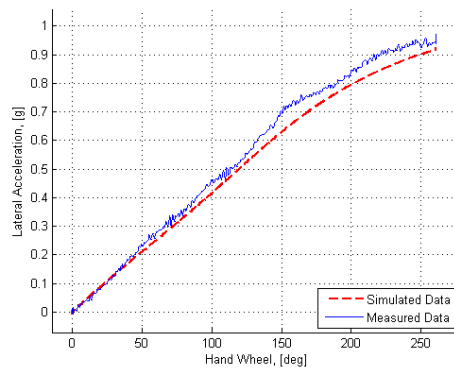


Figure C.48: Hand wheel vs. lateral acceleration; increasing steer, left turn, 11 m/s.

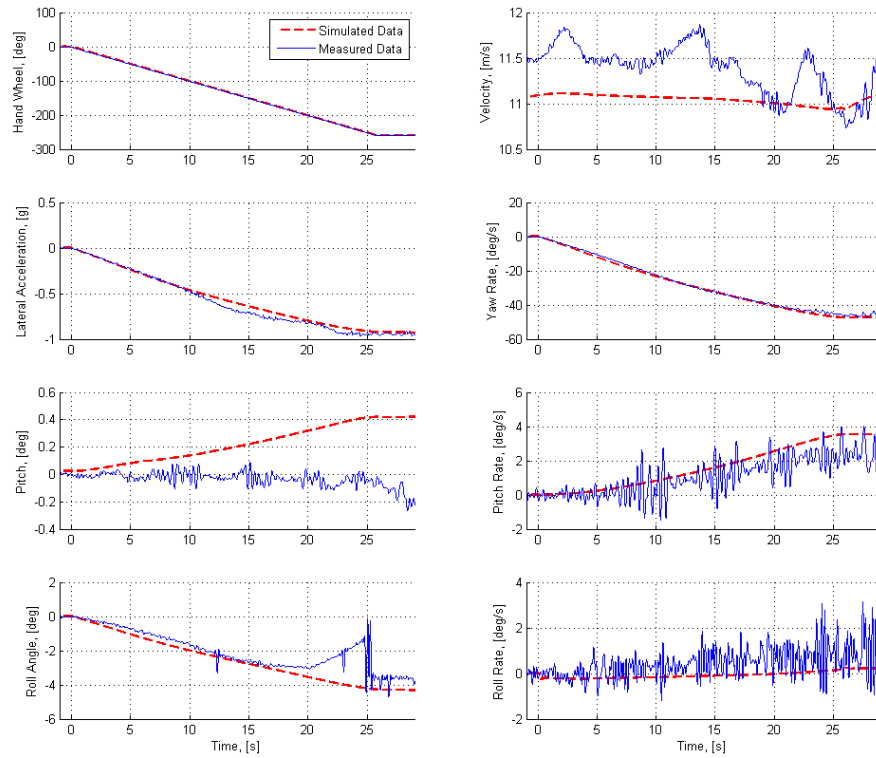


Figure C.49: Increasing steer experiment, right turn, 11 m/s.

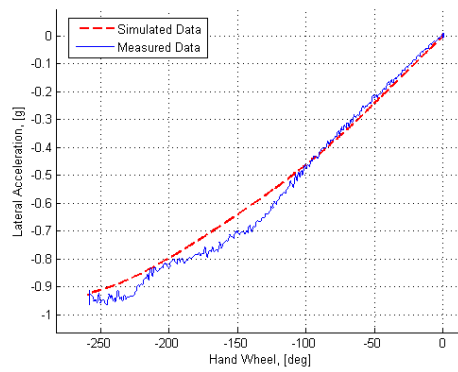


Figure C.50: Hand wheel vs. lateral acceleration; increasing steer, right turn, 11 m/s.

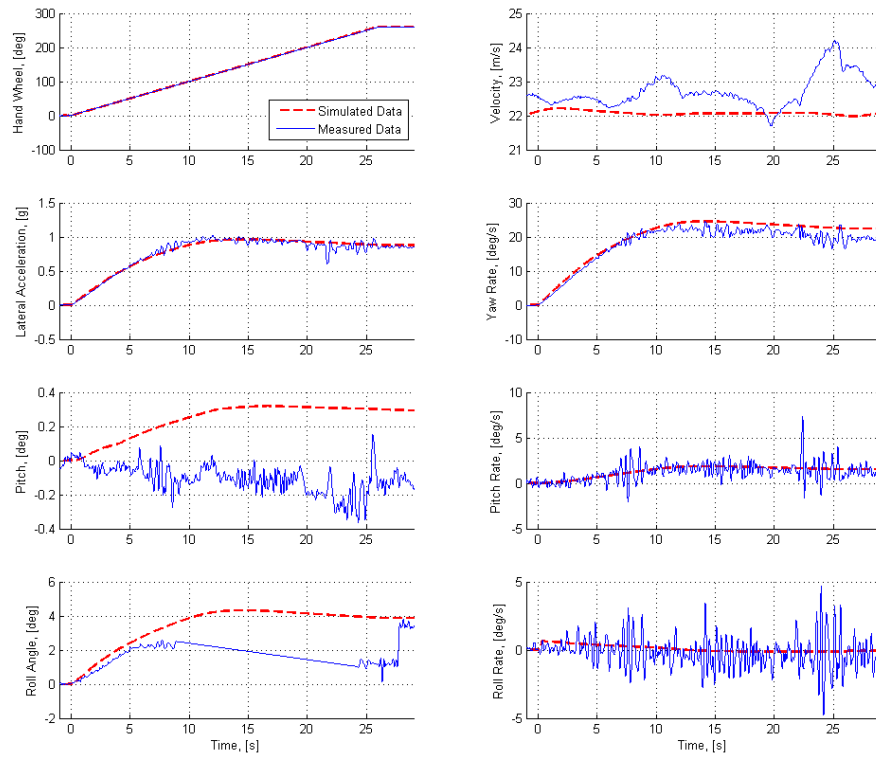


Figure C.51: Increasing steer experiment, left turn, 22 m/s.

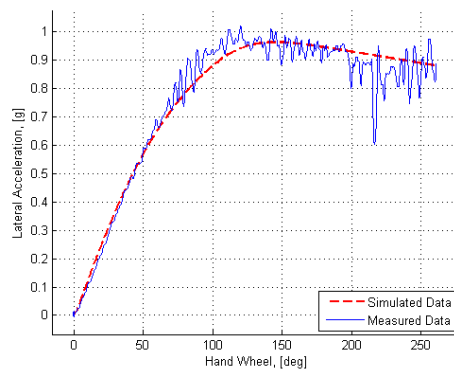


Figure C.52: Hand wheel vs. lateral acceleration; increasing steer, left turn, 22 m/s.

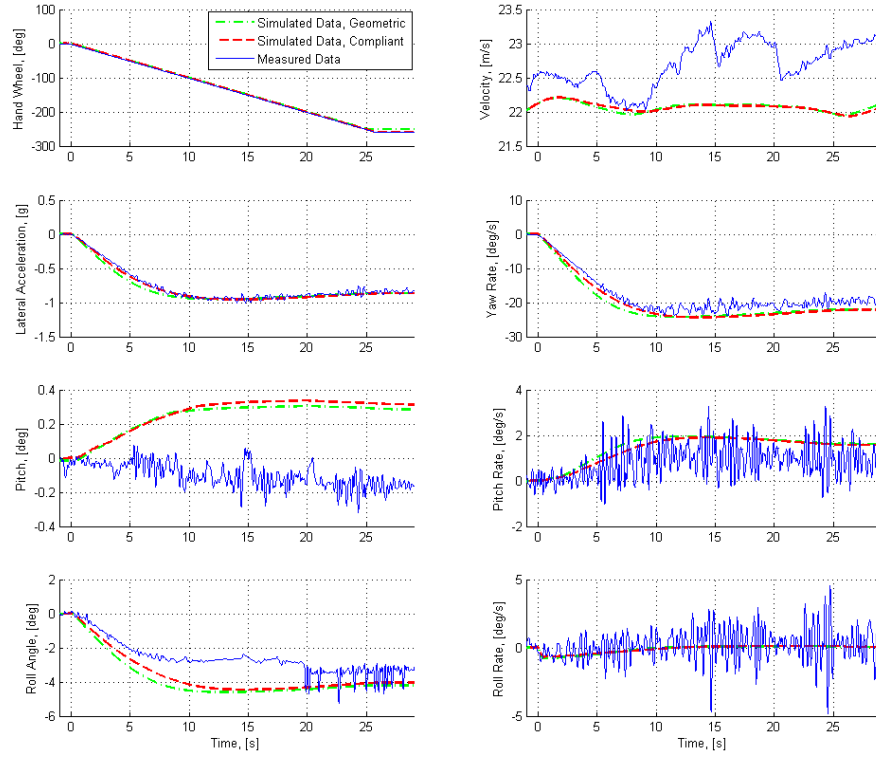


Figure C.53: *Increasing steer experiment, right turn, 22 m/s.*

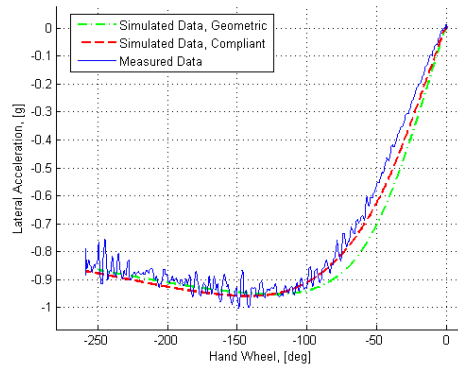


Figure C.54: *Hand wheel vs. lateral acceleration; increasing steer, right turn, 22 m/s.*

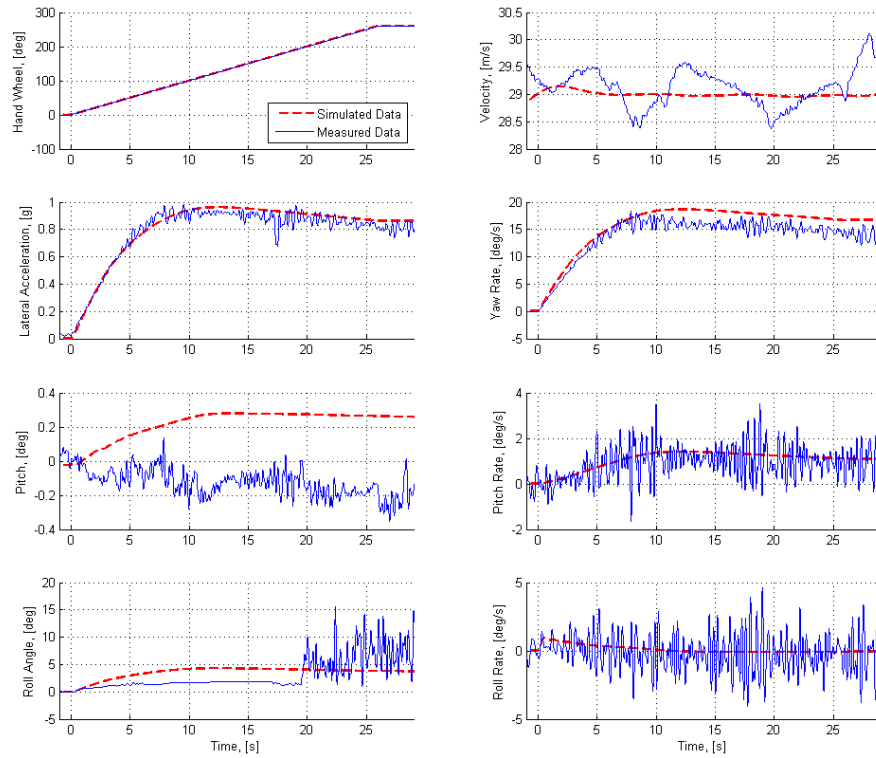


Figure C.55: Increasing steer experiment, left turn, 29 m/s.

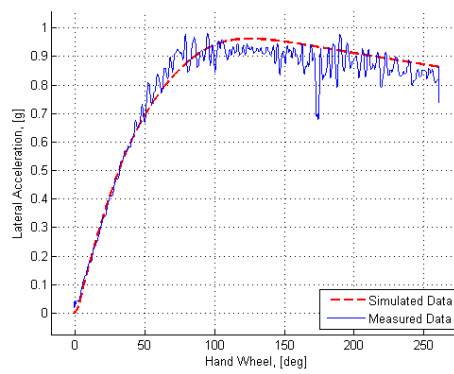


Figure C.56: Hand wheel vs. lateral acceleration; increasing steer, left turn, 29 m/s.

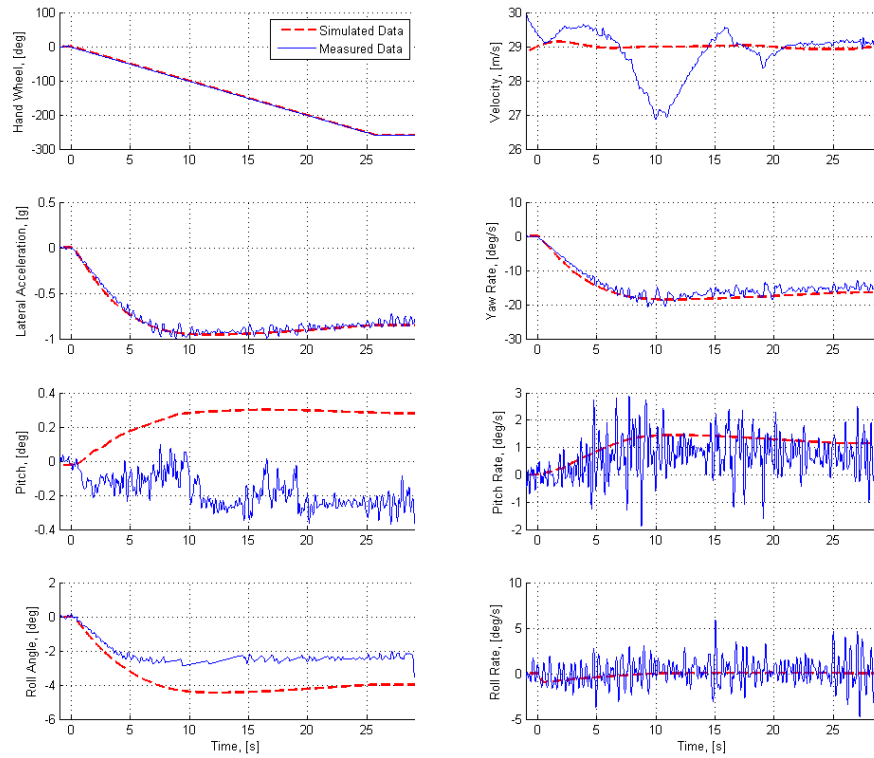


Figure C.57: Increasing steer experiment, right turn, 29 m/s.

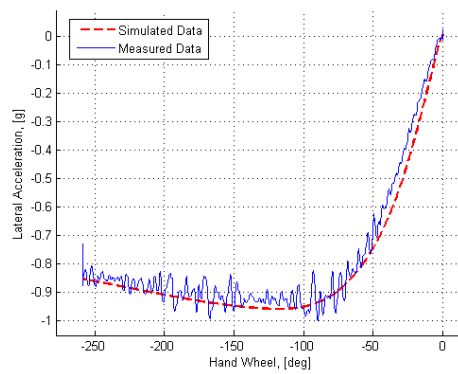


Figure C.58: Hand wheel vs. lateral acceleration; increasing steer, left turn, 29 m/s.

C.4.2 Step Steer

Simulation model is compared with measurement data for a step steer experiment. The hand wheel is turned with a step input at a constant vehicle speed. Six different experiments are done, varying speed, amplitude of steer input and turning direction.

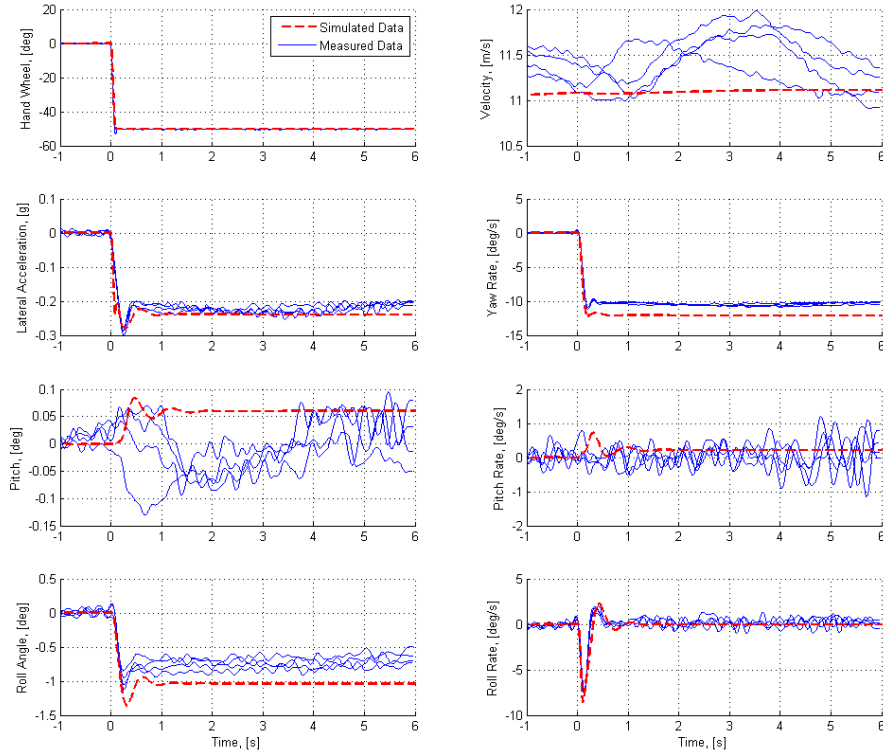


Figure C.59: Step steer experiment, right turn, 50° hand wheel input, 11 m/s.

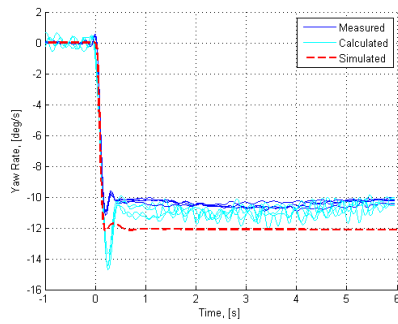


Figure C.60: Yaw rate comparison; step steer experiment, right turn, 50° hand wheel input, 11 m/s.

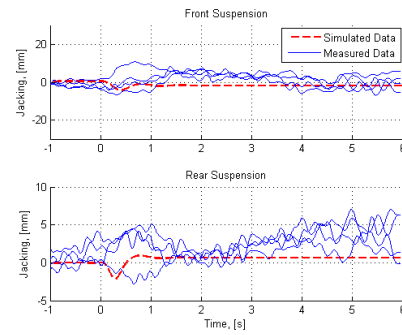


Figure C.61: Jacking; step steer experiment, right turn, 50° hand wheel input, 11 m/s.

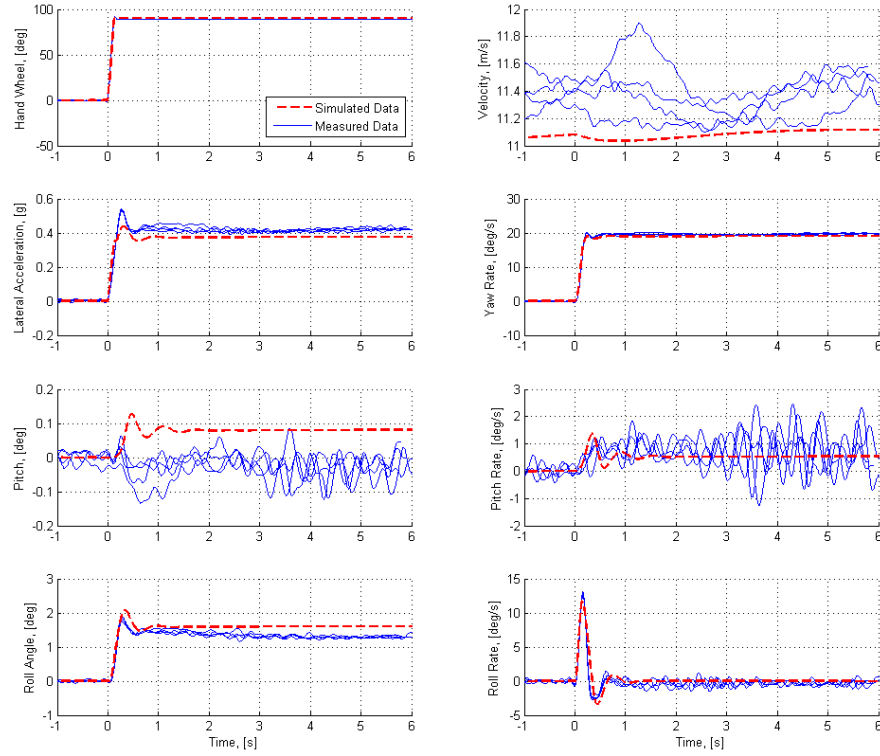


Figure C.62: Step steer experiment, left turn, 90° hand wheel input, 11 m/s.

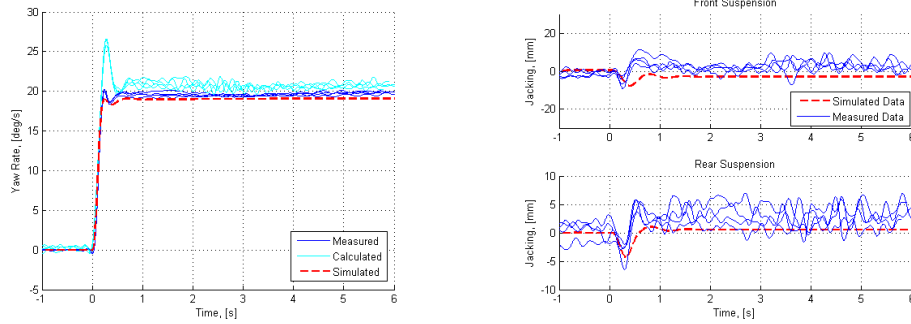


Figure C.63: Yaw rate comparison; step steer experiment, left turn, 90° hand wheel input, 11 m/s.

Figure C.64: Jacking; step steer experiment, left turn, 90° hand wheel input, 11 m/s.

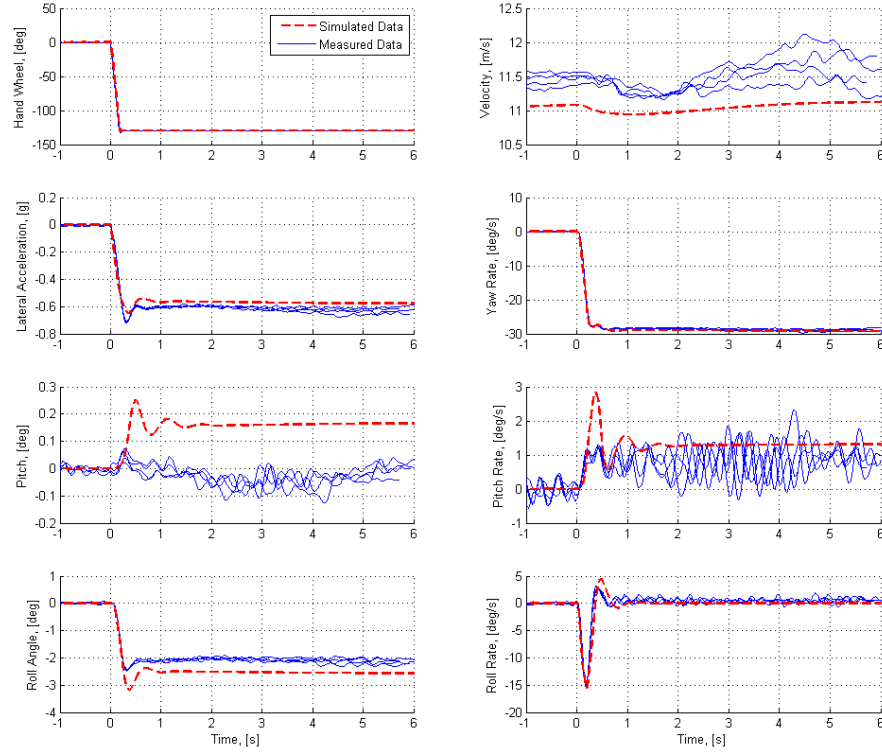


Figure C.65: Step steer experiment, right turn, 130° hand wheel input, 11 m/s.

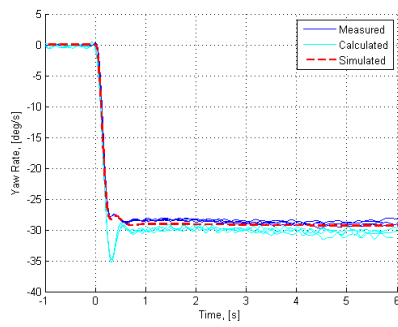


Figure C.66: Yaw rate comparison; step steer experiment, right turn, 130° hand wheel input, 11 m/s.

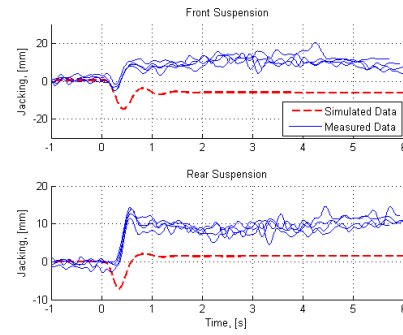


Figure C.67: Jacking; step steer experiment, right turn, 130° hand wheel input, 11 m/s.

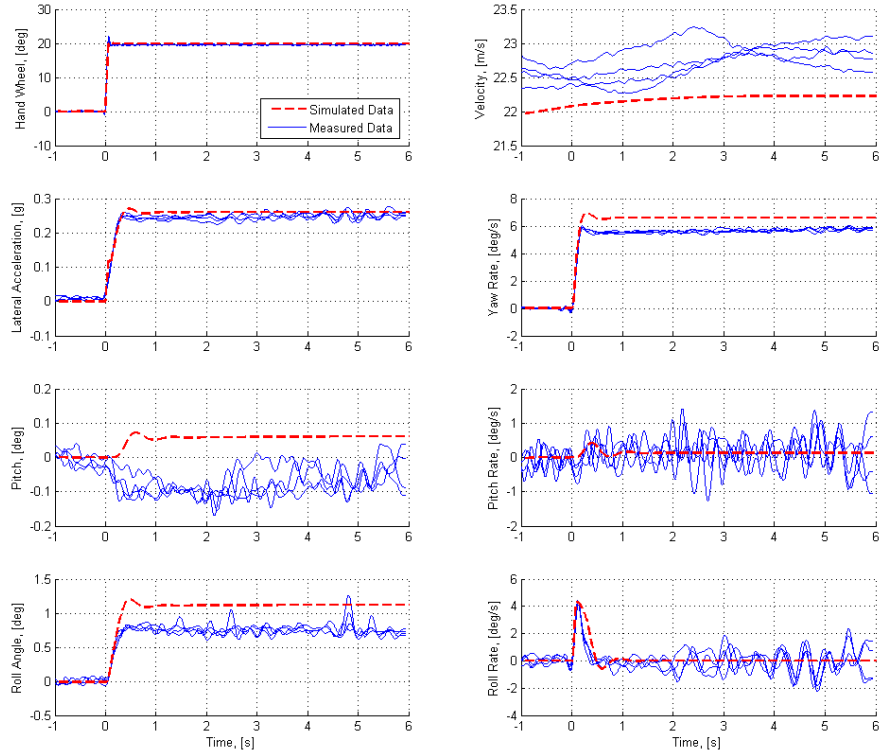


Figure C.68: Step steer experiment, left turn, 20° hand wheel input, 22 m/s.

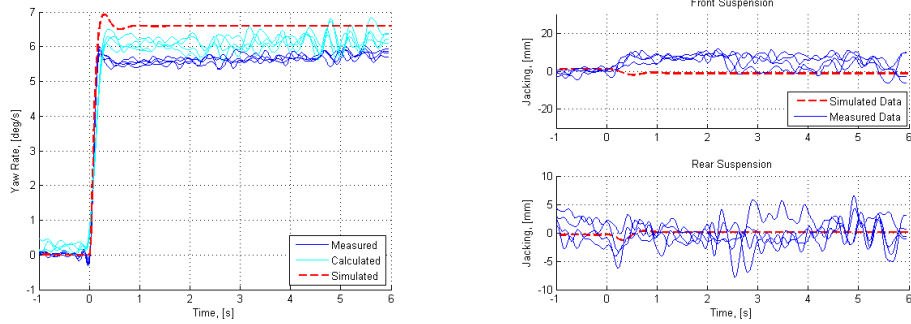


Figure C.69: Yaw rate comparison; step steer experiment, left turn, 20° hand wheel input, 22 m/s.

Figure C.70: Jacking; step steer experiment, left turn, 20° hand wheel input, 22 m/s.

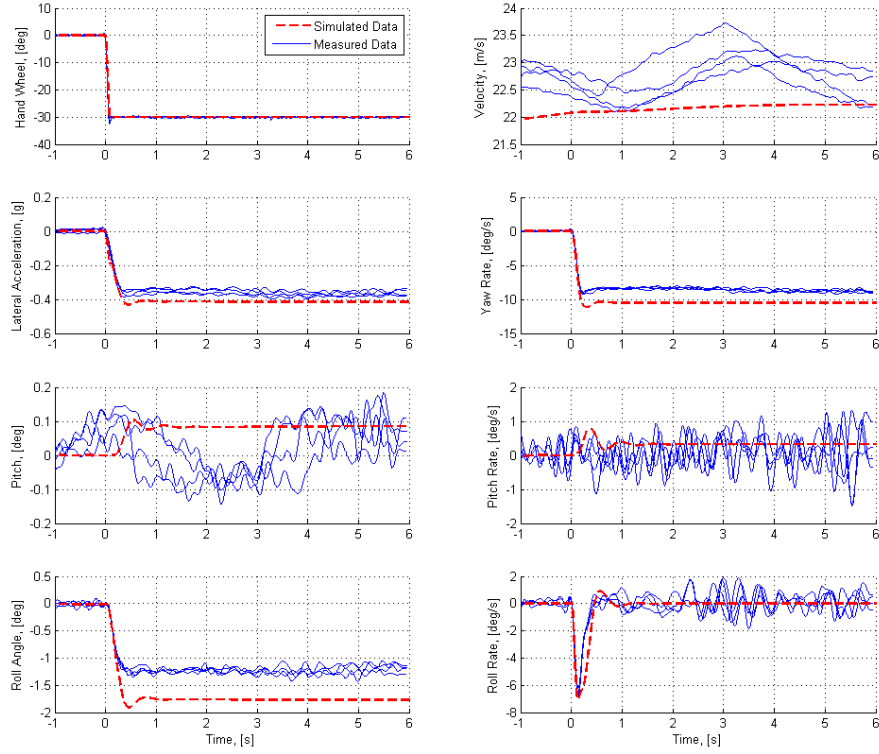


Figure C.71: Step steer experiment, right turn, 30° hand wheel input, 22 m/s.

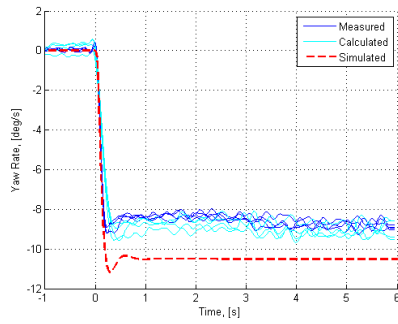


Figure C.72: Yaw rate comparison; step steer experiment, right turn, 30° hand wheel input, 22 m/s.

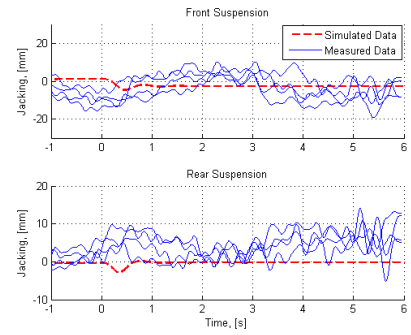


Figure C.73: Jacking; step steer experiment, right turn, 30° hand wheel input, 22 m/s.

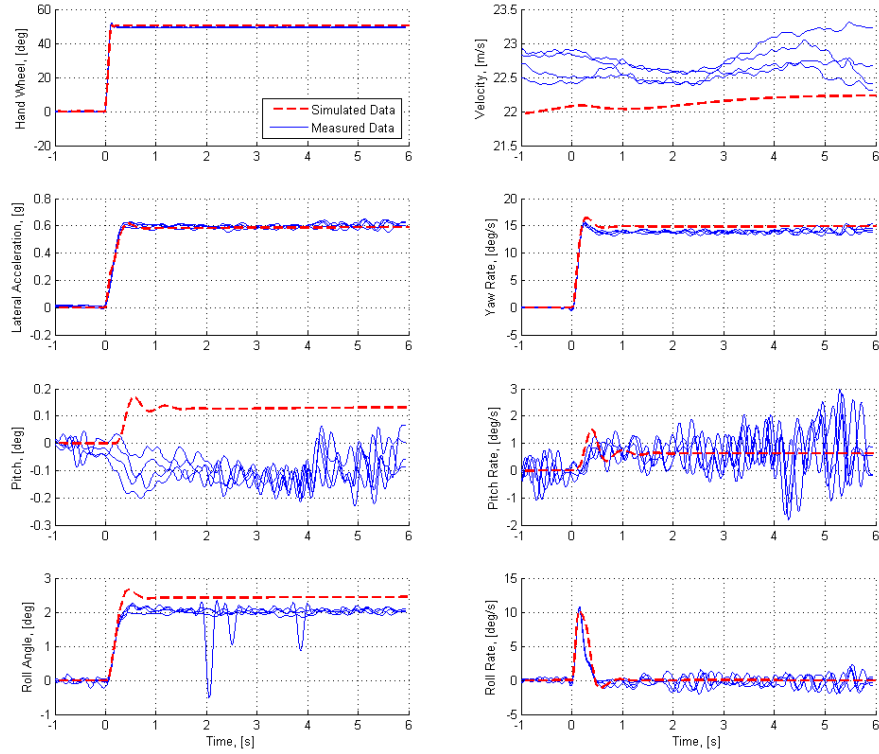


Figure C.74: Step steer experiment, left turn, 50° hand wheel input, 22 m/s.

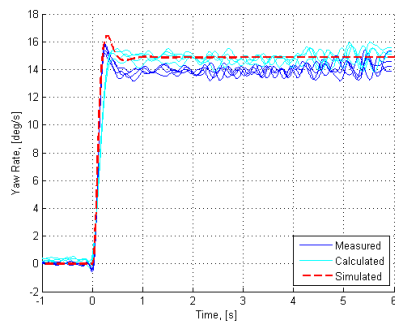


Figure C.75: Yaw rate comparison; step steer experiment, left turn, 50° hand wheel input, 22 m/s.

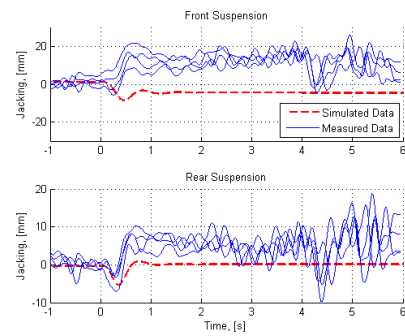


Figure C.76: Jacking; step steer experiment, left turn, 50° hand wheel input, 22 m/s.

C.4.3 Modified Front Suspension Geometry - Step Steer

A model using a modified front suspension, inner linkage joints moved vertically, is compared to the unmodified model and measurement data for a step steer experiment.

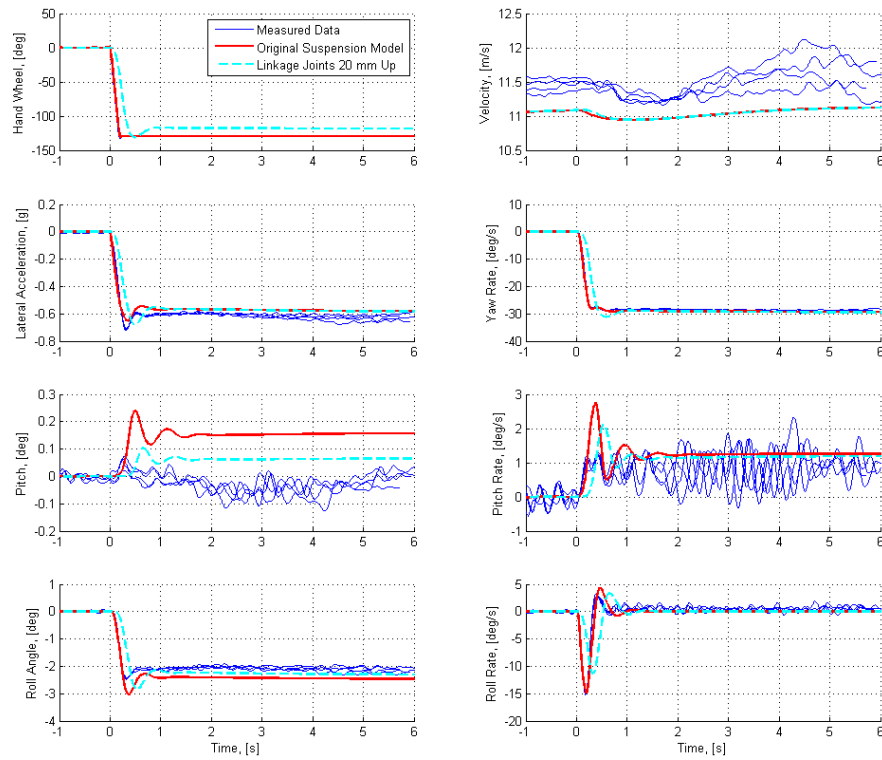


Figure C.77: Front suspension linkage joints moved up 20 mm. Step steer experiment, right turn, 130° hand wheel input, 11 m/s.

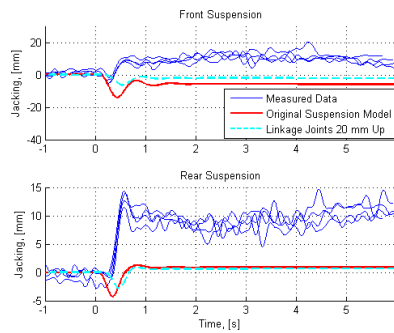


Figure C.78: Jacking in step steer experiment, linkage joints moved upwards.

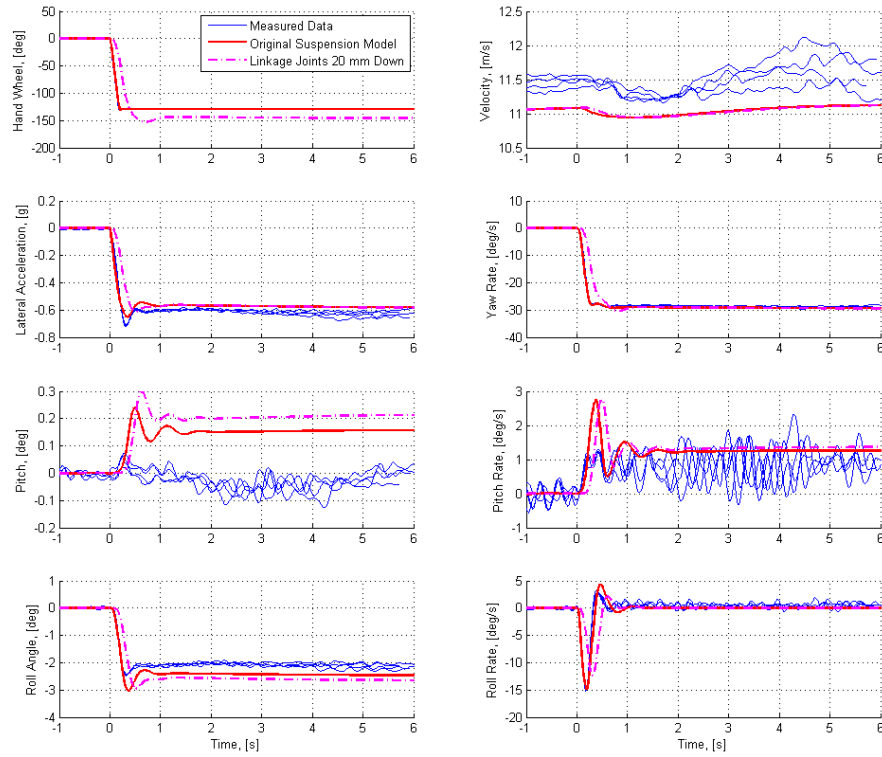


Figure C.79: Front suspension linkage joints moved down 20 mm. Step steer experiment, right turn, 130° hand wheel input, 11 m/s.

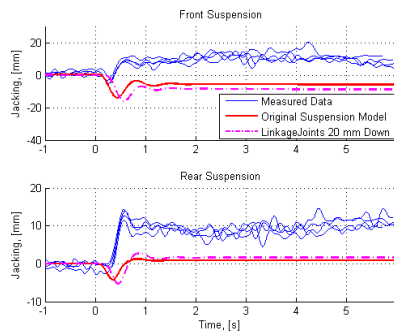


Figure C.80: Jacking in step steer experiment, linkage joints moved downwards.

Appendix D

Tabular Data

Appendix E

Source Code

E.1 Hub Elasticity

```
model elasticity6dof "Elastic component"
  import SI = Modelica.SIunits; import Modelica.Mechanics.MultiBody.Frames.*;
  Modelica.Mechanics.MultiBody.Interfaces.Frame_a frame_a
  "Coordinate system fixed to the component with one cut-force and cut-torque"
  annotation (Placement(transformation(extent= -116,-16,-84,16, rotation=0)));
  Modelica.Mechanics.MultiBody.Interfaces.Frame_b frame_b
  "Coordinate system fixed to the component with one cut-force and cut-torque"
  annotation (Placement(transformation(extent=84, -16,116,16, rotation=0)));
  Real r_rel[3]; //( stateSelect=stateSelect) "Vector from frame_a to frame_b resolved
in world frame, SI.Distance";
  Real r_rel_a[3];
  Real phi[3](start=0,0,0); //(, stateSelect=stateSelect) "SI.Angle";
  Orientation R_ab;
  Real f[3]; Real t[3];
  Real F[6];
  Real delta[6](start=0,0,0,0,0,0, stateSelect=StateSelect.always);
  Real ddelta[6](start=0,0,0,0,0,0, stateSelect=StateSelect.always);
  Real dddelta[6](start=0,0,0,0,0,0);
  parameter Real w=5;
  parameter Real alpha=1/(1.27*w)^ 2;
  parameter Real beta=2*0.87/(1.27*w);
  parameter Real k_left[6,6]=zeros(6,6)
  "compliance matrix for a left side wheel";
  parameter Boolean left_linkage=false;
  parameter Real f_pre[3]=0,0,0
  "pretension vector (forces), resolved in a, on left wheel";
  protected
  parameter Real k[6,6]=kappa.*k_left;
  parameter Real left=if left_linkage then 1 else -1;
  parameter Real kappa[6,6]=[ 1, left, 1, left, 1, left;
left, 1, left, 1, left, 1;
1, left, 1, left, 1, left;
```

```

left, 1, left, 1, left, 1;
1, left, 1, left, 1, left;
left, 1, left, 1, left, 1];
    outer Modelica.Mechanics.MultiBody.World world;
    equation
f=resolveRelative(frame_b.f,frame_b.R,frame_a.R)-f_pre.*{1,left,1};
t=resolveRelative(frame_b.t,frame_b.R,frame_a.R);
F=cat(1,f,t) "force and torque components resolved in frame a";
delta=cat(1,r_rel_a,phi)
"displacement and rotations resolved in frame a";
r_rel_a=resolve2(frame_a.R,r_rel);
ddelta=der(delta) "velocities resolved in frame a";
dddelta=der(ddelta) "accelerations resolved in frame a";
delta=-(alpha*dddelta+beta*ddelta-k*F) "the motion equation";
R_ab=axesRotations(1,2,3,phi,der(phi));
Connections.branch(frame_a.R, frame_b.R);
frame_b.R=absoluteRotation(frame_a.R,R_ab);
/* Force and torque balance */
zeros(3) = frame_a.f + resolveRelative(frame_b.f,frame_b.R,frame_a.R);
zeros(3) = frame_a.t + resolveRelative(frame_b.t,frame_b.R,frame_a.R) +
cross(r_rel, resolveRelative(frame_b.f,frame_b.R,frame_a.R));
end bessell6dof;

```